Doped polymer optical fibers for high performance fluorescent fiber applications

DISSERTATION
submitted for the degree of Doctor of Philosophy by

Itxaso Parola Domingo

Supervisors:
María Asunción Illarramendi Leturia
Joseba Zubia Zaballa

UNIVERSITY OF THE BASQUE COUNTRY
EUSKAL HERRIKO UNIBERTSITATEA
2018

"Creativity takes courage." – Henri Matisse

Agradecimientos

Durante estos años son muchas las personas que han contribuido de una forma u otra en este trabajo, y a quienes quiero expresar mi más profundo agradecimiento.

En primer lugar, a mis directores de tesis, María Asunción Illarramanedi y Joseba Zubia, por brindarme la oportunidad de unirme al Grupo de Fotónica Aplicada (APG) hace ya más de cuatro años, y por su confianza, su disposición y su inestimable ayuda durante la realización de este trabajo. Sin su orientación y apoyo esta tesis no habría sido posible. Especialmente gracias a Asun, a quien le debo gran parte de mi conocimiento en el mundo de las fibras de plástico dopadas, por su dedicación y motivación, y por ayudarme siempre a mejorar. Eskerrik asko bihotz-bihotzetik.

La realización de este proyecto tampoco habría sido posible sin la financiación recibida por el Departamento de Educación, Política Lingüística y Cultura del Gobierno Vasco/Eusko Jaurlaritza mediante su programa de ayudas predoctorales de formación de personal investigador no doctor.

Gracias también a todos mis compañeros del grupo de investigación APG, Igor, Jon, Oskar, Eneko, Joel, Begoña, Ibon, Amaia, Mikel, Iker, Iñaki, Gotzon, Gaizka, Josu, Rubén, Felipe y ángel. Especialmente a Igor, por ayudarme con las medidas en la primera etapa de esta tesis, a

Eneko, por estirar parte de las fibras utilizadas en este trabajo, a Jon, por enseñarme los fundamentos de la óptica allá por el último año de carrera y despertar mi interés en este ámbito, y por responder desinteresadamente a todas mis preguntas, y a Oskar y Joel, por estar siempre dispuestos a ayudarme y a transmitirme sus conocimientos. Quisiera extender este agradecimiento a Fede y a Nekane, por sus imprescindibles colaboraciones y aportaciones.

Agradezco a todo el personal del Departamento de Física Aplicada I, por la agradable acogida que me brindaron desde el primer momento y por el buen ambiente de trabajo del que he podido disfrutar. Por supuesto, gracias a todos mis compañeros de despacho y de comidas, Iñaki, Hao, Naiara, Jon, Aritz, Peio, Jorge y Vitalii. Echaré de menos nuestras tertulias del mediodía y nuestras estadísticas sobre las mandarinas. Gracias a Macarena y Arrate, por todos los buenos momentos que hemos pasado juntas, por vuestro apoyo y ayuda. Porque, más allá de ser las mejores compañeras de despacho, me llevo una gran amistad.

Muchas gracias al Profesor Hans-Hermann Johannes, por recibirme con los brazos abiertos en dos ocasiones el grupo Applied Organic Materials de la Universidad Técnica de Braunschweig, por darme la oportunidad de desarrollar gran parte del trabajo de esta tesis, por su amabilidad y por hacerme sentir como una más de su grupo. Es imprescindible agradecer también a todos mis compañeros de POF group, Jana, Daniel, Robert, Florian y Rickie, su agradable acogida y sus inmejorables aportaciones. Especialmente gracias a Daniel y a Jana. A Daniel, por ayudarme en mis primeros días en Alemania, por transmitirme tantísimos conocimientos de química, por enseñarme el mejor restaurante vietnamita de la ciudad y por su gran amistad. A Jana, por haber compartido conmigo tantos momentos durante mis estancias, por haberme dejado invadir un mes el salón de su casa, y por estar siempre dispuesta a ayudar, me llevo una

amiga para toda la vida. No se me puede olvidar mencionar a Kristoffer, al que también le invadí su salón, con él las risas están aseguradas. Gracias a todo el resto de integrantes del LEO, Justyna, Kathleen, Lea, Felix, Laurie, Tasja, Ouacef, Marko, Stefan. Vielen Dank!

Extiendo este agradecimiento a todas las personas con las que he compartido momentos a lo largo de esta tesis. En particular, quisiera agradecer a los expertos evaluadores que han contribuido en el desarrollo de esta tesis y a los miembros del tribunal.

Agradezco de todo corazón a mis padres, por su constante apoyo y cariño, porque sin ellos no habría sido capaz de llegar hasta aquí. Gracias a mi hermana Eider, y a Yago, por su ayuda y compañía, y por sus geniales ilustraciones. Por supuesto, gracias a todo el resto de mi familia, a mi Aitite y mi Amama, mis tíos y primos, y a mis amigos. Tampoco puedo olvidarme de dar las gracias a mi familia granaína.

Por último, gracias Alex, por ayudarme a ver la vida desde un prisma de positividad, por enseñarme a apreciar hasta las más pequeñas de las cosas. Gracias por acompañarme en esta etapa de la vida, por tu apoyo, tu ayuda y tu sonrisa. Ahora, la aventura continua. ¡Gracias!

Resumen

La sociedad actual ha experimentado los mayores y más destacados avances tecnológicos desde la Revolución Industrial a finales del siglo XIX. El desarrollo en ámbitos como el transporte, las comunicaciones, la medicina o la producción de energía, entre otros, se ha convertido en el pilar principal del progreso global actual. En este contexto, esta tesis engloba el uso de fibras ópticas de plástico (FOP) dopadas en dos áreas en pleno desarrollo y muy demandadas por la sociedad moderna: comunicaciones ópticas y producción de energía sostenible.

El despliegue global de las comunicaciones basadas en fibra óptica ha sido, desde sus inicios, dominado por las fibras ópticas de vidrio. Sin embargo, el uso de FOPs ha aumentado considerablemente en los últimos años debido a los diversos beneficios que éstas presentan. Son ligeras, finas y flexibles, y exhiben buena tolerancia frente a torsiones y desalineaciones, lo que las convierte en fáciles de manejar desde el punto de vista del usuario. Además, fabricar enlaces FOP es más fácil y barato que para su equivalente de vidrio, ya que los dispositivos FOP (conectores, terminaciones, etc.) son más sencillos y menos costosos. Este hecho conlleva una reducción en el coste de instalación y de mantenimiento de los enlaces de FOP. Por otra parte, la posibilidad de dopar FOPs con una amplia variedad de materiales funcionales ha abierto un abanico de nuevas aplicaciones en los campos de los láseres, amplificadores,

iluminadores y sensores en la región visible. Las fuentes de luz basadas en fibra óptica son útiles en múltiples aplicaciones. Como ejemplo, los láseres basados en FOP son especialmente atractivos como fuentes de luz en aplicaciones de redes de área local (LAN, por sus siglas en inglés) ya que pueden ser fácilmente acoplados a sistemas FOP, igual de sencillo que dos FOPs se conectan entre sí. Además, debido a una serie de factores atenuantes, la potencia de la señal transmitida a través de una FOP disminuye considerablemente con la distancia, y por consiguiente, la señal necesita ser restaurada. En este sentido, amplificadores de fibra óptica que aumenten la potencia de la señal de manera sencilla y eficiente son altamente necesarios. La amplificación de la señal también es de gran importancia en sistemas de comunicación de banda ancha en los que se emplea la tecnología de multiplexación por división de longitud de onda (WDM, por sus siglas en inglés). Haciendo uso del amplio espectro de ganancia de los amplificadores FOP se consigue amplificar los canales de un sistema WDM con aproximadamente la misma ganancia. Las FOP dopadas se han convertido en un medio de ganancia eficiente para dar cabida a la gran demanda en estos campos. En este contexto, esta tesis aborda el estudio de la emisión espontánea amplificada y las propiedades de ganancia óptica de diversas FOP dopadas con rodamina 6G con el objetivo de demostrar su potencial como fuentes de luz y amplificadores de fibra.

El segundo tema clave de este trabajo aborda la necesidad de encontrar nuevas fuentes de energía renovables para, por un lado, tratar de dar una solución eficiente a la creciente demanda de energía de hoy en día, y, por otro lado, tratar de resolver la amenaza del calentamiento global. La tecnología fotovoltaica se prevé como una prometedora candidata para hacer frente a estos desafíos, ya que presenta la mayor perspectiva de crecimiento entre las fuentes de energía renovables. Convertir la luz solar en electricidad por medio de células fotovoltaicas ha sido

objeto de innumerables investigaciones a lo largo de más de 60 años. Sin embargo, la producción de energía solar todavía no puede competir económicamente con la energía producida a partir de fuentes fósiles. Mediante el uso de concentradores solares luminiscentes (LSC, por sus siglas en inglés), es posible disminuir el coste del sistema de captación de energía solar al concentrar la luz en un área más pequeña de células fotovoltaicas sin necesidad de utilizar ningún tipo de mecanismo de alineación o de rastreo. Tradicionalmente, los LSC se diseñaron con una configuración plana, lo que implicó una limitación importante a la hora de acoplar la luz desde sus bordes tanto a células fotovoltaicas como a fibras ópticas pasivas. Sin embargo, varios estudios demostraron que este inconveniente se podía resolver fácilmente mediante el uso de LSCs con geometría cilíndrica. Además, con esta nueva configuración se llegan a obtener mayores capacidades de concentración que con los LSCs planos. En este contexto, las FOP dopadas han obtenido gran relevancia ya que son baratas, faciles de conectorizar y demuestran alto rendimiento al concentrar energía solar. En este sentido, la segunda parte de esta tesis analiza las propiedades ópticas de varias FOP dopadas con el principal objetivo de estudiar su posible uso como concentradores solares luminiscentes.

Laburpena

XIX. mendearen amaierako Industria-Iraultzatik gaur egunera arte aurrerapen teknologiko handiak eta nabarmenak jasan ditu gizarteak. Besteak beste, garraiobideak, komunikabideak, medikuntza eta energia ekoizpena gaur egungo garapenaren ardatz bilakatu dira. Testuinguru honetan, tesi honek plastikozko zuntz optiko (PZO) dopatuen erabilerak biltzen ditu garapen osoan dauden bi arlotan: komunikazio optikoak eta energia iturri berriztagarriak.

PZO bidezko komunikazioak, hasiera–hasieratik, beirazko zuntz optikoen bitartez gauzatzen ziren. Hala ere, azken urteetan, PZO–en erabilera nabarmen handitu da hauek aurkezten dituzten onura desberdinak direla eta. Pisu arinekoak, finak eta malguak dira, eta tortsio eta ezlerrokatzeen aurrean tolerantzia altua erakusten dute. Ezaugarri hauek, erabilera erraza ahalbidetzen dute erabiltzailearen ikuspuntutik. Gainera, PZO–zko loturak fabrikatzea errazagoa eta merkeagoa da haien beirazko baliokideekin konparatuta, hain zuzen ere PZO loturentzako dispositiboak (konektoreak, bukaerak, eta abar.) sinpleagoak eta kostu gutxiagokoak direlako. Honek, PZO–zko loturen instalazio eta mantentze kostuak asko murrizten ditu. Bestalde, PZO–ak material funtzional ezberdin askorekin dopatzeko aukera dela eta, haien erabilerak eskualde ikuskorrean lan egiten duten alor ezberdin askoetara zabaldu du, hala nola, PZO–zko laserretara, anplifikagailuetara eta sentsoreetara. Zuntz

optikoan oinarritutako argi–iturriek aplikazio anizkunetan erabilgarriak direla frogatu dute. Adibide bezala, PZO–etan oinarritutako laserrak bereziki erakargarriak dira area lokaleko sareetan (LAN, ingelesazko bere siglengatik) argi iturri bezala erabiltzeko, oso erraz konektatu ahal direlako PZO loturetara (bi PZO elkarren artean lotzen diren bezain erraz). Gainera, atenuazio iturri desberdinak direla eta, PZO batean zehar transmititzen den seinalearen potentzia nabarmen gutxitzen da distantziarekin, eta beraz, seinalea berreskuratu beharra dago. Zentzu honetan, seinalearen potentzia era erraz eta eraginkor batean berreskuratzen duten PZO–zko anplifikagailuak beharrezkoak dira. Seinalearen anplifikazioak garrantzi handia du ere banda zabaleko uhin–luzera banatuzko multiplexazio–teknologia (WDM, ingelesezko bere siglengatik) erabiltzen duten komunikazio sistemetan. PZO anplifikagailuaren irabazi espektral zabala erabiliz, WDM sistemako kanal guztiak gutxi gorabehera irabazi berdinarekin anplifikatzea lortzen da. Beharrizan guzti hauei lekua emateko, PZO dopatuak irabazi ingurune eraginkorrak bilakatu dira. Testuinguru honetan, tesi honek errodamina 6G–z dopaturiko PZO–en berezko igorpen anplifikatuaren eta irabazi optikoaren ezaugarriak aztertzen ditu, haien potentziala argi–iturri eta zuntzezko anplifikadore bezala frogatzeko helburuarekin.

Tesi honek bigarren gai garrantzitsu bezala energia–iturri berriztagarri berriak aurkitzeko beharrak jorratzen ditu. Batetik, premiazkoa da energia iturri berriztagarri berriak lortzea gaur eguneko energia eskari gorakorrari konponbide eraginkorra emateko, eta, bestalde, berotze globalaren mehatxuari irtenbide bat emateko ezinbestekoak dira ere. Erronka hauei aurre egiteko teknologia fotovoltaikoa etorkizun handiko teknologia bezala planteatzen da, energia–iturri berriztagarrien artean hazkunde aukerarik handiena aurkezten duelako. Eguzki–argia zelula fotovoltaikoen bidez elektrizitatea bihurtzea aspaldi hasi zen aztertzen. Hala ere, eguzki–energiak oraindik ezin du iturri fosilen bitartez pro-

duzitutako energiarekin ekonomikoki lehiatu. Eguzki–kontzentratzaile lumineszenteko erabileraren (LSC, ingelesazko bere siglengatik) bitartez, posiblea da eguzki–energia eskuratzeko sistemaren kostua gutxitzea, hain zuzen ere eguzki–argia zelula fotovoltaikoko azalera txikiago batean kontzentratzea ahalbidetzen dutelako inolako lerrokatze eta eguzki–bilaketa mekanismoen beharrik gabe. Tradizioz, LSC–ak konfigurazio lauarekin diseinatu ziren. Dispositibo hauek, galera handiak erakusten dituzte haien ertzetako argia zelula fotovoltaikoetara edota zuntz optikoetara atxikitzerako orduan. Hainbat ikerketak eragozpen hau geometria zilindrikoko LSCs–ak erabiliz errazki ebatz zitekeela frogatu zuten. Gainera, konfigurazio berri honekin kontzentrazio ahalmen handiagoak lortzen dira LSCs lauekin konparatuz. Testuinguru honetan, dopatutako PZO–ek garrantzi handia irabazi dute eguzki–argia era merkean eta errendimendu altuarekin kontzentratzeko sistemak bezala. Zentzu honetan, tesi honen bigarren atalak, hainbat PZO dopatuen ezaugarri optikoak aztertzen ditu, LSC bezala erabiltzeko aukera posibleak ikertzeko.

Contents

List of Figures **xxi**

List of Tables **xxvii**

List of Acronyms **xxviii**

1 Introduction **1**
1.1 Motivation 1
1.2 Thesis outline 3

2 Polymer Optical Fibers: Overview **7**
2.1 Introduction 7
2.2 POF Parameters 9
2.3 Host materials 13
2.4 Loss mechanisms in POFs 18

3 Fundamentals of dye-doped POFs **21**
3.1 Energy level model 22
3.2 Light absorption 24
3.2.1 Linear absorption 24
3.2.2 Two-photon absorption 25
3.3 Light emission 26
3.3.1 Spontaneous emission 27
3.3.2 Stimulated emission 28
3.3.3 Amplified spontaneous emission 29
3.4 Rate equations 32
3.4.1 Analytic expressions in steady state 37

3.5 Photodegradation 38

4 ASE features and gain phenomena in doped POFs 41
4.1 General background 42
4.2 Experimental methods 47
4.3 Result 1: ASE and gain in R6G doped GI PMMA POFs . 53
4.3.1 Samples 54
4.3.2 ASE features Vs pump energy 57
4.3.3 ASE features Vs z_e and study of the net gain . . . 61
4.3.4 Polarization effects on ASE and on the net gain . . 69
4.4 Result 2: Cladded and uncladded R6G doped thermoset SI POFs 74
4.4.1 Samples 74
4.4.2 ASE features Vs pump energy 76
4.4.3 Study of the net gain 79
4.4.4 Polarization effects on ASE and on the net gain . . 82
4.4.5 Two-photon emission 85
4.5 Conclusions 86

5 Solar energy concentration using doped POFs 93
5.1 General background 94
5.2 Luminescent solar concentrators 98
5.2.1 Past, present and future 98
5.2.2 LSC operation 100
5.2.3 Loss mechanisms in LSCs 101
5.2.4 LSC materials 104
5.2.4.1 Host materials 104
5.2.4.2 Dopant materials 105
5.3 Fluorescent fiber solar concentrators 109
5.4 Experimental methods: efficiency calculations 111
5.5 Result 1: POFs doped with organic materials as FFSC . . 114
5.5.1 Samples 114
5.5.2 Optical losses 116
5.5.3 Side illumination coupling efficiency 118
5.5.4 FFSC efficiency 120
5.5.5 Conclusions 121

5.6 Result 2: POFs doped with lumogen dyes as FFSCs . . . 122
5.6.1 Samples . . . 122
5.6.2 Optical losses . . . 125
5.6.3 Side illumination coupling efficiency . . . 127
5.6.4 Analysis under solar simulator . . . 128
5.6.5 Conclusions . . . 132
5.7 Result 3: High performance FFSCs employing double-doped POFs . . . 132
5.7.1 Samples and characterization methods . . . 133
5.7.2 Fiber fabrication . . . 136
5.7.3 Hybrid absorption and emission bands . . . 138
5.7.4 Output power and FFSC efficiency . . . 139
5.7.5 Performance under simulated weather scenarios . . 142
5.7.6 Power-saturation fiber length . . . 145
5.7.7 Photostability . . . 148
5.7.8 Conclusions . . . 152
5.8 Result 4: Diameter dependence on double-doped POFs for FFSCs . . . 153
5.8.1 Samples and characterization methods . . . 154
5.8.2 Output power and FFSC efficiency . . . 155
5.8.3 Performance under simulated weather scenarios . . 160
5.8.4 Power-saturation fiber length . . . 163
5.8.5 Conclusions . . . 166

6 Conclusions and open lines **169**
6.1 Conclusions . . . 169
6.2 Open lines . . . 174

Bibliography **177**

Thesis outreach **201**

List of Figures

2.1 Structure of a POF 10
2.2 Refractive index profiles of SI, MSI and GI POFs 11
2.3 Cross sections of 37 cores and 217 cores multicore POFs . 12
2.4 Cross sections of a microstructured preform, the intermediate cane, and the final mPOF 12
2.5 Attenuation of a PMMA SI POF 15
2.6 Polymer structure differences between thermoplastic and thermoset polymers 18
2.7 Classification of the intrinsic and extrinsic loss mechanisms in POFs 19

3.1 Schematic of the Jablonski diagram 22
3.2 Schematic of the linear absorption mechanism 25
3.3 Schematic of the two-photon absorption 26
3.4 Schematic of the spontaneous emission 27
3.5 Fluorescence lifetime 28
3.6 Schematic of the stimulated emission 29
3.7 Signatures of the ASE 31
3.8 Two methods for the calculation of the ASE threshold energy 32
3.9 Set-up for the theoretical model under longitudinal excitation 33
3.10 Set-up for the theoretical model under transversal excitation 36
3.11 Power evolution in fluorescence and gain regimes 39
3.12 Photodegradation of two POF samples 40

4.1 Illustration of the experimental set-up for the study of the ASE features as function of the pump energy 49
4.2 Polarization reference system 50
4.3 Experimental set-up for gain analysis: VSL method 51
4.4 Experimental set-up for the analysis as function of the non exited fiber length 52
4.5 Experimental set-up for two-photon fluorescence measurements 53
4.6 Refractive index and dye distribution of R6G doped GI POFs 55
4.7 Microscope images of the R6G doped GI PMMA POFs . 55
4.8 Absorption and emission curves of R6G doped PMMA POFs 56
4.9 Evolution of the emission spectra of F12 and F16 for different pump energies 57
4.10 Progression of the spectral full width at half maximum for both F12 and F16 samples as functions of the pump energy 58
4.11 Evolution of the output intensities of F12 and F16 samples as functions of the pump energy 59
4.12 Progression of the average emission wavelength as a function of the pump energy for F12 and F16 fibers 60
4.13 Evolution of the emission spectrum of F16 sample for different illuminated lengths 61
4.14 Evolution of the FWHM, the output intensity and the λ_{avg} of F12 sample as a function of z_e 63
4.15 Evolution of the FWHM, the λ_{avg} and output intensity of F16 sample as a function of z_e 64
4.16 Theoretical and experimental evolution of the FWHM for the F16 sample and three pump irradiances 65
4.17 Example of the calculation of the optical gain for the F16 GI PMMA POF 66
4.18 Spectral net gains for F12 and F16 fibers 66
4.19 Attenuation coefficients of F16 sample. 67

4.20 Theoretical calculation of the evolution of the local gain at different positions z on the fiber for three different $z_{e,max}$ 68

4.21 Evolution of the FWHM of the emitted spectra and of the output intensity of the F12 sample for horizontal and vertical polarizations 70

4.22 Illustration of the radiation patterns for a dipole parallel to the fiber symmetry axis and for a dipole perpendicular to the fiber symmetry axis 70

4.23 Average emission wavelength as a function of the pump energy for horizontal and vertical polarizations. 71

4.24 Evolution of the FWHM curve of F12 for two different polarizations and three pump irradiances. 72

4.25 Example of gain calculation for horizontal and vertical polarizations for F12 sample 73

4.26 Microscope images of the R6G thermoset SI POFs 75

4.27 Absorption and emission curves of the cladded R6G thermoset POFs 76

4.28 Evolution of the emission spectra of the cladded thermoset sample for different pump energies 77

4.29 Evolution of the FWHM and the λ_{avg} of the emission as functions of the pump energy for the uncladded and cladded thermoset POFs 77

4.30 Example of the calculation of the optical gain for the uncladded thermoset POF 80

4.31 Spectral gains for the uncladded and cladded thermoset fibers 80

4.32 Spectral gains for PMMA and thermoset samples 81

4.33 Evolution of the FWHM and the λ_{avg} as functions of the pump energy for the uncladded and cladded samples and horizontal and vertical polarization 83

4.34 Comparison of the optical gain curves of the uncladded and cladded samples for horizontal and vertical polarizations 84

4.35 OPA and TPA emission spectra of the cladded thermoset POF 86

4.36 Representative illustration of the distance traveled by the rays in OPA and TPA configuration 87
4.37 FWHM and λ_{avg} of the emitted spectra as functions of the light propagation length for OPA and TPA and uncladded and cladded samples 88

5.1 Global primary energy consumption by source in 2017 . . 95
5.2 Solar radiation spectra 95
5.3 Examples of geometric solar concentrators 97
5.4 Schematic diagram of a basic square planar LSC showing its operating principle 100
5.5 Schematic illustration of the loss mechanism processes involved in LSCs 102
5.6 Absorption and emission bands of the Lumogen F orange 240 dye 107
5.7 Absorption and emission of $Eu(TTFA)_3Phen$ 109
5.8 Schematic diagram of a fluorescent fiber solar concentrator 111
5.9 Illustration of the side illumination coupling efficiency calculation 112
5.10 Illustration of the fluorescent fiber solar concentration efficiency calculation 113
5.11 Absorption and emission spectra of the LR01 and PF3T samples 116
5.12 Evolution of λ_{avg} as function of z_{ne} LR01-04 and conjugated polymers 117
5.13 Evolution of the output intensity with z_{ne} at three different wavelengths for LR02 sample 117
5.14 Attenuation coefficients of LR and conjugated polymer samples measured by the SIT 118
5.15 Power absorbed sideways as a function of the pump power for η_{SIC} calculation 119
5.16 Chemical structures of lumogen violet, yellow, orange, and red 123

5.17 Photograph of lumogen violet, yellow, red, and orange doped POFs 124
5.18 Absorption and emission bands of the lumogen doped POFs 125
5.19 Evolution of the output intensity and of the λ_{avg} as a function of the propagation distance for the four lumogen doped POFs 126
5.20 Optical attenuation coefficients for the four lumogen doped POFs 126
5.21 Power absorbed sideways by the lumogen doped POFs as a function of the pump power for η_{SIC} calculation 128
5.22 Output power as a function of z_e for the lumogen doped POFs 129
5.23 Evolution of the output power and the fiber surface temperature along 10 h lamp exposure 131
5.24 Chemical structures of Eu(TTFA)$_3$Phen, Lumogen Orange, Perylene, Coumarin-1, and Coumarin-6 134
5.25 Outdoor photograph of the emission of one of the samples being excited by sunlight. 135
5.26 Two photographs of some fibers in the set-up under solar simulator excitation 136
5.27 Photographs of the preforms and two fibers under UV excitation 138
5.28 Emission of the AM 1.5G radiation and the solar-simulator, and absorption and emission bands of the five double-doped combinations 140
5.29 Photograph of the reflective layer placed bellow one of the samples 142
5.30 Evolution of the η_{FFSC} for three of the samples as a function of the pump power 145
5.31 Photograph of a sample rolled into several loops under the solar simulator excitation 146
5.32 Evolution of the output power as a function of the illuminated fiber length. 147

5.33 Example of the evolution of the normalized output power as a function of the measurement time after 160 h of exposure 148

5.34 Evolution of the normalized output power during the excitation/recovery tests as a function of the measurement time. 151

5.35 Photographs of the preforms before and after polymerization. 155

5.36 Output power, output irradiance and η_{FFSC} for the three double-doped samples as function of the fiber core diameter. 156

5.37 Representative model of the distance traveled by light in fibers with different radius. 157

5.38 Experimental and theoretical output power, output irradiance and η_{FFSC} of Eu/L sample fiber as function of the fiber core diameter 160

5.39 Evolution of the η_{FFSC} of the three double-doped combinations for different weather scenarios as function of the fiber core diameter 163

5.40 3D plot of the variation of the η_{FFSC} with two variables: excitation irradiance and fiber core diameter 164

5.41 Evolution of the output power as a function of the illuminated fiber length for three fiber diameters. 165

6.1 Photographs of 7 fiber arrays mounted on semicircular reflective rails 176

List of Tables

4.1 Summary of the characteristics of the R6G doped PMMA GI POFs 55
4.2 ASE characteristics of F12 and F16 60
4.3 ASE characteristics of F12 for two pump polarizations . . 71
4.4 Summary of the characteristics of the R6G doped thermoset SI POFs 75
4.5 ASE characteristics of the uncladded and cladded thermoset POFs 78
4.6 PMMA Vs thermoset fiber characteristics 81
4.7 ASE characteristics of the uncladded and cladded thermoset POFs for horizontal and vertical polarizations . . . 84
4.8 Average FWHM and λ_{avg} slopes for OPA and TPA 87
4.9 Summary of the results from Chapter 4 91

5.1 Summary of the desired dopant properties for LSC operation 106
5.2 Summary of the main characteristics of the POFs doped with lumogen red and conjugated polymers 115
5.3 Values of the side illumination coupling efficiencies of POFs doped with lumogen red and conjugated polymers 120
5.4 Values of the fluorescent fiber solar concentration efficiencies of POFs doped with lumogen red and conjugated polymers 121
5.5 Summary of POF samples doped with lumogen dyes . . . 124

5.6 Average loss coefficients and saturation lengths for the lumogen doped samples 130
5.7 Information about the dopants employed in each of the double-doped fibers and of the polymer parameters 137
5.8 Output power, output intensity, η_{FFSC}), and relative power improvements for 6 cm illuminated fiber length, with and without mirror 143
5.9 Relative η_{FFSC} improvements for each of the simulated weather scenarios 145
5.10 Saturation fiber length, output saturation power and irradiance for each sample under test 147
5.11 Exposure time in hours until reaching 65% (PD65%) and 50% (PD50%) of the initial emission, and degradation saturation level 149
5.12 Partial recovery percentages after darkness resting. Recovery-1 and recovery-2 151
5.13 Time in hours (h) until reaching 15% of of the initial emission for each of the radiation periods 152
5.14 Summary of the five fiber diameters 154
5.15 Output power, η_{FFSC} and irradiance values without and with reflective layer 161
5.16 Saturation fiber length, saturation output power, and saturation irradiance for five different fiber diameters 164

List of Acronyms

APG	Applied Photonics Group
ASE	Amplified Spontaneous Emission
BIPV	Building Integrated Photovoltaics
CSIC	Consejo Superior de Investigaciones Cientficas
FBG	Fiber Bragg Grating
FFSC	Fluorescent Fiber Solar Concentrator
FOP	Fibra Óptica de Plástico
FWHM	Full Width at Half Maximum
GI	Graded-Index
GSC	Geometric Solar Concentrator
IC	Internal Conversion
ISC	Intersystem Crossing
LAN	Local Area Network
LSC	Luminescent Solar Concentrator
MMA	Methyl methacrylate
mPOF	Microstructured Polymer Optical Fiber
MSI	Multi-Step-Index
NA	Numerical Aperture
NZEB	Net Zero Energy Buildings
OD	Optical Density
OPA	One-Photon Absorption

PC	Polycarbonate
PF	Perfluorinated
PMMA	Poly(methyl-methacrylate)
POF	Polymer Optical Fiber
PS	Polystyrene
PV	Photovoltaic
PZO	Polimerozko Zuntz Optikoa
QD	Quantum Dots
R6G	Rhodamine 6G
SI	Step-Index
SIT	Side-Illumination Technique
TPA	Two-Photon Absorption
TUB	Technical University Braunschweig
VR	Vibrational Relaxation
VSL	Variable Stripe Length
WDM	Wavelength-Division Multiplexing

Chapter 1

Introduction

1.1 Motivation

Today's society has experienced the greatest and most outstanding technological advances since the Industrial Revolution at the end of the 19th century. The development of transport, communications, medicine or energy production, among others, has settled the pace of the current global progress. In this context, this thesis addresses the use of doped polymer optical fibers (POF) in two areas in full development and highly demanded by the modern society: optical communications and sustainable energy production.

The global spread of optical fiber-based communications has traditionally been governed by silica optical fibers. However, the use of POFs has greatly increased in recent times due to the several benefits they present. They are light-weight, thin and flexible, and they show great

tolerance to bending and misalignment, what makes them easy handling from the consumer point of view. Besides, they are easier and cheaper to fabricate, terminate, polish and connect than their glass counterparts, what reduces the cost off installation and maintenance. Moreover, the potential of doping POFs with a wide variety of functional materials opened a versatile range of new applications in the fields of lasers, amplifiers, illuminators, switches and sensors in the visible region. Fiber light sources have proven to be useful as all-purpose standalone applications. As an example, POFs lasers are especially attractive as light sources in local area networks (LAN) applications since they can be straightforward coupled to a POF system, in the same simple way as passive POF connect to each other. Besides, the signal transmitted over a POF considerably decreases with distance due to a number of attenuating factors, and consequently it needs to be restored. In this respect, fiber optic amplifiers that increases the signal power are highly demanded. Signal amplification is also of great importance in high bandwidth telecommunication systems where wavelength division multiplexing (WDM) technology is used. Taking advantage of the spectrally broad-gain of POF amplifiers, they can be used to amplify all the channels in a WDM system with approximately the same gain. In the search for efficient gain medium to meet the requirements on this field, the dye doped POFs came to the forefront. In this context, this thesis addresses the issues of amplified spontaneous emission and gain properties of various rhodamine-6G doped POFs.

Regarding the second key issue approached in this work, it is common knowledge that the search for alternative sustainable energy sources has become of great urgency to try to give a solution to the threat of global warming. Moreover, the energy obtained from burning fossil fuels is considered non-renewable, and at some point it will become too costly

to harvest, what threatens the possibility of accommodating the nowadays huge energy demand. Photovoltaic (PV) technology appears to be a promising candidate to face these challenges, as it has the largest growths prospects among renewable energy sources. The objective of converting sun-light into electricity by means of PV-cells has been deeply studied. However, the solar energy production still can not economically compete with fossil energy sources. Luminescent solar cocentrators (LSC), are seen as a potential strategy to decrease costs by concentrating the sun-light into a smaller area of PV-cells without needing any kind of sun-trucking and alignment mechanisms. Traditionally, LSCs had planar configuration, what involved a major limitation in coupling the output light at the edges. However, several studies demonstrated that a cylindrical geometry could solve this drawback, and even show a greater concentration capacity than planar LSCs. In this context, polymer optical fibers have gained huge attention as cost-effective and high performance sustainable energy acquisition devices. In this regard, the second part of this thesis analyzes the properties of several doped POFs with the main objective of their possible use as luminescent solar concentrators.

1.2 Thesis outline

According to the previously depicted objectives, the work in this thesis has been structured as follows:

Chapter 2— A general overview of polymer optical fibers is presented in this chapter. It covers a historical introduction of the use of POFs since their first applications to today's uses, together with a presentation of the basic parameters and typical host materials employed in this type of fibers. Finally, it introduces the basic loss mechanisms

present in POFs. The main objective of this chapter is to put the reader into perspective on basic concepts of passive POFs to address the following chapters regarding doped POFs.

Chapter 3— The fundamentals to understand the optical processes behind a dye-doped POF are described in this chapter. It starts with the description of the light-matter interactions in organic materials by means of the Jablonski diagram, comprising phenomena such as linear absorption, two-photon absorption, and emission. Different types of emission are presented, such as spontaneous emission, stimulated emission and amplified spontaneous emission (ASE), which is the base of the light amplification in doped POFs. To sum up, it presents a theoretical model to describe light generation and amplification by the so-called rate equations, together with three steady state analytic equations that will be used all along the results of this thesis.

Chapter 4— This chapter begins with an overview of the state-of-the-art of doped POFs in the field of ASE fiber lasers an fiber amplifiers. Afterwards, the experimental methods employed along the results sections are described. Finally, the experimental results concerning ASE and gain in rhodamine-6G doped POFs are presented. The first study corresponds to two gradded-index poly(methyl-methacrylate) (PMMA) fibers of different dopant concentrations, whereas the second one is based on two step-index thermoset fibers of same concentration, one with cladding and the other only core. Within the analysis carried out, the dependence of the ASE performance with the pump energy, the excited fiber length, and the pump polarization are found. Two-photon absorption phenomenon is also reported for the SI thermoset POFs. Comparisons between fibers are presented and discussed.

Chapter 5— This chapter provides a global perspective of the worldwide energy consumption followed by the state-of-the-art in luminescent solar concentrators. It describes their operation fundamentals, together with the typical host and dopant materials employed and the common loss sources. An overview of the new concept of fluorescent fiber solar concentrators (FFSC) is also presented. The experimental works are reported into 4 sections. The first two results comprise various experiments to determine the possible application of several doped POFs as FFSC, such as the the optical losses, the side illumination coupling efficiency and the fluorescent fiber solar concentrator efficiency. Following, the design, fabrication and characterization under AM 1.5G standard excitation of several novel double-doped POFs is presented. Finally, the diameter dependence of some of the double-doped fibers is experimentally and theoretically discussed.

Chapter 6— Lastly, the overall conclusions and the open lines are presented in this chapter.

Chapter 2

Polymer Optical Fibers: Overview

Prologue— *This chapter offers a general overview of polymer optical fibers. It comprises a historical introduction of the use of POFs since their very first steps to nowadays applications, together with a presentation of the basic parameters and typical host materials employed in this type of fibers. Finally, it also introduces the basic loss mechanisms present in POFs. The main objective of this chapter is to put the reader into perspective on the basic concepts of passive POFs to address the next chapter where the fundamentals of dye doped POFs are presented.*

2.1 Introduction

The inventions of the telegraph first, and then of the telephone in the mid-19th century, marked a turning point in the way people communicated, starting the era of the electrical telecommunications. Subsequent

inventions, led to the transmission of not only sound, but also figures and images, what significantly increased the amount of transmitted information. The historical trend in telecommunication systems was to shift to use progressively higher carrier frequencies, which offered an increase in the bandwidth and in the information capacity. Soon, the optical portion of the electromagnetic spectrum became attractive as the optical frequencies are several orders of magnitude higher than those employed in electrical communication systems. Hence, the use of optical carrier frequencies provided far larger transmission capacities in comparison to the electrical systems. However, it was not until the invention of the first laser in the 1960s that significant advance in optical communications was made. At this time, the well-known polymer POFs were first introduced, at the same time as the invention of their glass counterparts. Optical fibers offered groundbreaking advantages such as very high bandwidth, immunity to electromagnetic interference, electrical insulation and lightweight [1]. The first POFs employing PMMA as host material had quite high attenuation (in the order of 1000 dB/km at 670 nm), what limited their use to illuminating and sensing applications rather than data transmission. Since the dramatic growth of the transmitted data with the widespread of the internet in the 90's, optical fibers gained great relevance, as electrical wiring could not bear the ever-increasing needs of bandwidth and high transmission speeds. Silica-based single mode fibers dominated the field of long-distance and high-speed optical networks. However, due to their very small diameters ($\sim$ 10 μm), extreme accuracy in their connections and terminations is required, what makes the costs of private intranets in homes, offices and buildings, too high. Successive improvements in the materials of POFs, downgraded the limits of attenuation to around 20 dB/km at 650 nm in a step-index deuterated PMMA fiber [2], and to around 10 dB/km at 1.0 μm in a perfluorinated graded-index POF (CYTOP® material) [3]. The theoretical limit of at-

tenuation of the later is estimated to be 0.7 dB/km at 1.0 μm, and it is expected to lower further by impoving the fabrications methods [4]. Thanks to these improvements, in addition to their advantages for consumer use (high tolerance to bending and misalignment, high mechanical strength and easy handling), POFs became attractive again. They have been gradually installed in short-haul communication links, such as LANs in homes, buildings and vehicles, and also as interconnects in computers, reaching bit rates of more than 40 Gb/s over 100 m fiber employing perfluorinated gradded-index POFs [5].

Moreover, the posibility of doping POFs has widely extended their potential to applications in the field of fiber amplifiers, lasers [6], illuminators [7, 8] and a variety of sensing use [9, 10]. In the last few years, due to the improvements carried out in the materials and in the fabrication process, their use has also been expanded to the field of photovoltaic technology, acting as high performance solar energy concentrators [11].

2.2 POF Parameters

The cross-section of a POF is typically circular and generally divided into two layers (core and cladding), with the possibility of adding a protective cover called *jacket* in case of POFs used for optical communications (see Figure 2.1). Light is trapped and guided along the core by total internal reflection enabled by $n_{co} > n_{cl}$ condition, being n_{co} and n_{cl} the refractive indexes of the core and the cladding respectively.

Traditionally, POFs are divided into two main groups depending on the core refractive-index profile, namely step-index (SI) and graded-index (GI). In SI fibers, the refractive index is uniform all along the core. They can be single mode or multimode, and they are used mostly for short op-

tical communications, as they have high intermodal dispersion. As a possible alternative, multi-step-index (MSI) fibers were proposed. Their core is formed by several layers, approaching the total refractive index to a parabolic profile. They are multimode fibers that combine the simplicity in fabrication of the SI POFs but with higher bandwidth potential [12]. Nowadays, thanks to advanced modulation techniques, the high intermodal dispersion of the SI POFs can be overcame [13]. In GI POFs, the refractive index decreases gradually with the distance r to the symmetry axis. This profile enables a compensation in the difference in distance covered by the fastest and slowest modes, so the intermodal dispersion is reduced in some orders of magnitude. GI POFs are always multimode and can be used in short and medium communications. Figure 2.2 shows the refractive index profiles in SI, MSI and GI POFs.

During the past years new types of POFs have been proposed, such as multicore POFs and microstuctured POFs (mPOF). Multicore POFs are produced by stacking together a certain number of small size cores embedded in a cladding material, until forming the desired cross-section (about 1 mm typically), as it is shown in Figure 2.3. These fibers combine the advantages of having large diameters, such as easy light-coupling and straightforward manipulation by user, and the benefits of having small cores, what involves smaller sensitivity to bending losses. Multicore POFs can be used in applications such as data transmission in fiber-to-

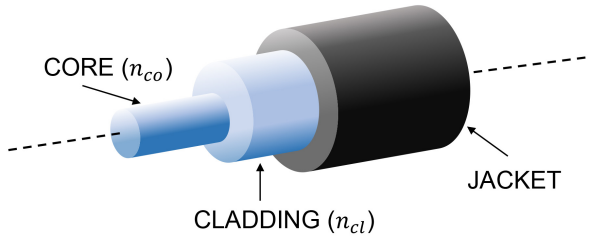

Figure 2.1: Structure of a POF.

the-home links and short-reach optical interconnections [14, 15].

On the other hand, mPOFs are a quite recent development in the field of POFs, first reported in 2001 [16]. Since then, there has been an active interest in searching applications for which they could show competitive advantages over other technologies [17]. The light is guided through microscopic air-channels that run longitudinally along the fiber axis, hence, the attenuation induced by the absorption of polymeric materials is not present in these fibers. They show the advantages of large fiber diameters and the transmission properties of single-mode fibers. Moreover, their use offers a new range of possible applications. For instance, the capillarity property of the holes can be used in the sensor field to analyze chemicals, gases or other substances, as it allows a close interaction between the optical field and the substance to be sensed [18]. Fiber Bragg gratings (FBG) have been written in mPOF, even if at the first stage some difficulties were found that strongly increased the inscription time. However, fast FBG writing in mPOF has recently been reported [19, 20, 21]. Figure 2.4 illustrates the cross sections of a microstructured preform, the intermediate cane (employed as an intermediate step in mPOF fabrication) and the final mPOF.

The contrast between the refractive indexes of the core and cladding

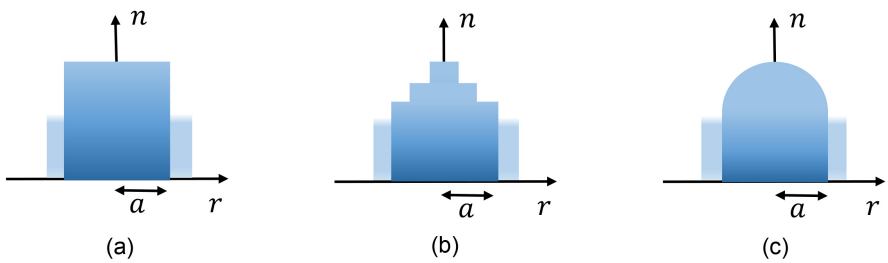

Figure 2.2: Refractive index profiles in a step-index POF (a), a multi-step-index POF (b), a and gradded-index POF (c).

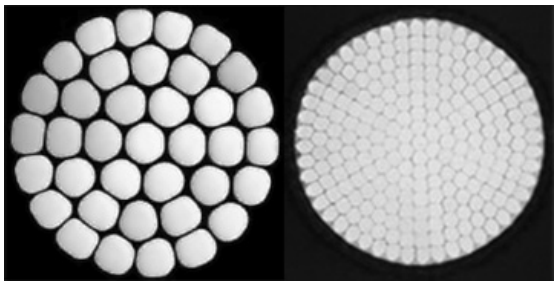

Figure 2.3: Cross sections of 37 cores and 217 cores multicore POFs (Figures from Asahi Kasei).

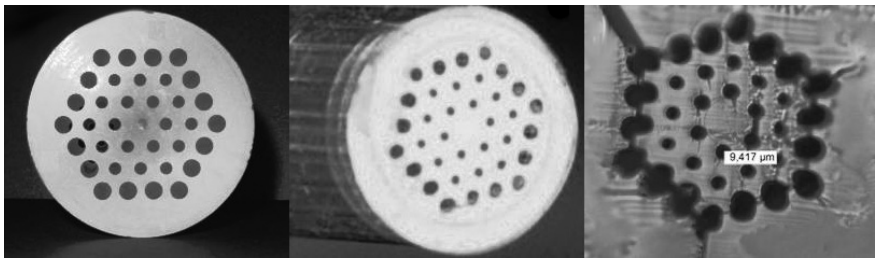

Figure 2.4: Cross sections of a microstructured preform (left), the intermediate cane (center), and the final mPOF (right).

has considerable impact on the optical properties of the fiber. The most direct impact lies on the light collection capacity of the POFs, largely determined by the numerical aperture (NA):

$$NA = \sqrt{n_{co}^2 - n_{cl}^2} \tag{2.1}$$

Therefore, POFs with high contrast between core and cladding, show relatively high NAs, what improves the coupling efficiency of lightwaves into POFs and reduces bending losses. However, big values of NAs also creates difficulties in the fabrication of single-mode fibers. Single-mode fibers have comparatively small cores and they require wave model of light for their analysis. Multimode fiber though, have cores large enough to be studied with a geometric ray-tracing model. The number of modes

N that an optical fiber supports is related to the V parameter (*normalized frequency*) given by:

$$V = \frac{2\pi r}{\lambda} NA \tag{2.2}$$

$$N = \frac{V^2}{2} \tag{2.3}$$

where r is the core radius and λ is the light propagation wavelength through the fiber. If V is greater than 2.405, it can be demonstrated that the behaviour of a SI POF is multimode [22]. For a typical POF link it can be obtained that the approximate number of modes is $N \approx 10^4 - 10^6$. The main advantage of single-mode POF is the absence of modal dispersion, what provides higher bandwidths [23]. However, with comparatively small cores, they lack the main advantages of the conventional POFs (easiness to handle and low-cost connectors), and they exhibit a much larger attenuation than their glass counterparts ($\sim$ 200 dB/km at 652 nm). For these reasons, the single-mode POF research has not been very active. However, recent advances in the fabrication of single-mode POFs with a minimal attenuation levels have expanded the potential of these POFs to, for example, the field of sensors [24, 25, 26, 27], and they have become potential candidates for making in-line devices compatible with single-mode silica fibers. Moreover, single-mode fibers will be needed for telecommunication applications [23].

2.3 Host materials

One of the most important features the materials employed in optical fibers should meet is a high transparency in their operational region. Besides, their mechanical resistance, thermal stability and robustness

against external factors such as humidity, radiation, or acidity, should be considered for each of the targeted applications. PMMA has dominated the field of POFs since the very beginning. Its history dates back to the first POF activities developed by DuPont company in the 1960s. That early PMMA material had very high transmission losses ($\sim$ 1000 dB/km at 670 nm) so their use was limited to illumination, sensing applications, and automobile and aircraft instrumental panels. Successive improvements in fiber fabrication led to a considerable decrease in attenuation, reaching values of 130 dB/km at 650 nm for a PMMA SI POF developed by Hoechst-Celanese. The theoretical attenuation limit of PMMA based fibers is estimated to be 106 dB/km at 650 nm, and it was nearly achieved in 1998 by Koeppen et al. [28]. PMMA has three loss windows at 570, 650, and 780 nm (see Figure 2.5), and its general properties are light weightiness, high transparency in the visible region and excellent corrosion resistance to both chemicals and weather. The refractive index of PMMA is $n = 1.49$ and the Tg values of commercial PMMAs range from 85 to 165 °C. PMMA-based POF show high water absorption. For some applications such as humidity [29] or moisture [30] sensors, this feature represents an advantage. However, for other applications such as strain and temperature sensing, the high humidity sensitivity of PMMA is a disadvantage [31]. Nowadays, PMMA is a mass produced cost-effective commercially available polymer widely used in microstrutured fibers [16], multicore fibers [32], and nanofibers [33], among others. PMMA has become a valuable substitute for glass in optical fibers.

Other types of polymer used in POFs are the so-called deuterated polymers. These polymers result from replacing some or all of the hydrogen atoms with deuterium. Thus, the chemical properties of the molecules remain unchanged, but the physical properties can be modified. Deuterated polymers reduce the absorption loss at the visible and the near infrared wavelengths and show higher heat capacity. The low-

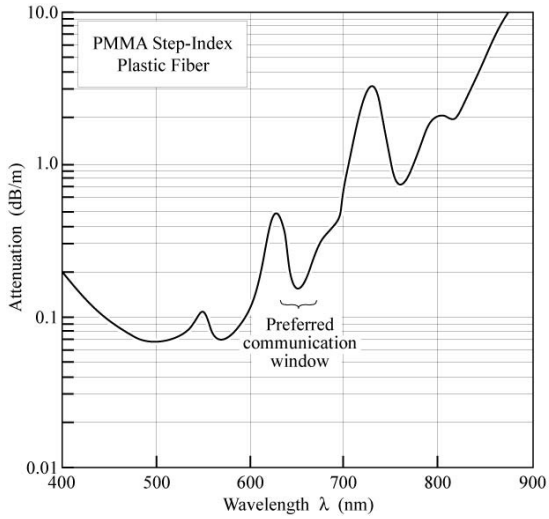

Figure 2.5: Attenuation of a PMMA step-idex POF. Preferred communication window at 650 nm. (Data from Toray Industries Ltd. [34]).

loss windows are located at longer wavelengths in comparison to those of PMMA. The first deuterated PMMA fiber (SI PMMA-d8) was manufactured by DuPont company in 1977. Many improvements were carried out during the years, reaching attenuation values of 20 dB/km at 680 nm [35]. This milestone appeared to lead to high potential fiber market, but deuterated polymers show several disadvantages that made these type of fibers not succeed. As an example, deuterated POFs show an increase in water absorption, what rises dramatically the attenuation, and the deuterated precursors needed for their production have an extremely high price, what makes them unsuitable for mass fabrication. A recent work on deuterated PMMA was carried out by Kondo where they applied a PMMA cover to protect the light-transmission from humidity [36].

Other kind of polymers investigated for POF fabrication are the perfluorinated (PF) polymers. They became popular since they further improved the potential of POFs. They are uniquely resistant to chemicals, and the vibrational absorption losses in the visible and near-infrared are

negligibly small. One of the most well-known PF polymer is the so-called CYTOP®, developed by AGC (Asahi Glass Co. Ltd.). The first CYTOP-based GI POF was commercialized in 2001 [37]. The thermal stability of CYTOP material is comparable to that of PMMA, and it exhibits fairly low light scattering because of its low refractive index ($n = 1.34$). Experimentally, an attenuation of 10 dB/km at 1000 nm has been measured, although the theoretical attenuation limit is calculated to be 0.3 dB/km at 1300 nm. Thus, it is expected that the attenuation could be lowered further by preventing contamination sources during manufacturing [4].

Among the wide variety of available polymers for POFs, we can also find poly-styrene (PS) and polycarbonate (PC). PS is transparent in the visible spectrum, inexpensive and available in large quantity. It shows advantages such as decrease in water absorption an theoretical lower attenuation in between 600 and 700 nm compared to PMMA POFs. However, the superior mechanical and chemical resistance of PMMA limited their success. PS is used as host matrix in some special applications such as fluorescent fibers or sensing [38]. On the other hand, PC shows extraordinary thermal and mechanical resistance, commonly used in high temperature scenarios. The theoretical optical properties of PC POFs are similar to those of PMMA based POFs. Nowadays, PC POFs are used in fields such as textile integrated illumination [39] or microstructured hollow core fibers [40].

In the last years, new polymers have been employed to overcome the high humidity sensitivity of PMMA. Among these materials, TOPAS® [41] (copolymer) and ZEONEX® [42] are found. Both materials are insensitive to humidity and can operate at high temperatures due to their high Tg exceeding 130°C. Moreover, due to the molecular weight and melt flow index of ZEONEX, a more stable and controllable fiber drawing

is assured, what allows a more robust fabrication of microstructured POFs [43]. Several works have been publisehd regarding mPOFs and FBG sensors based on TOPAS and ZEONEX materials [24, 31, 44, 45]. TOPAS and ZEONEX materials also present good transparency in THz frequencies [46, 47].

All the aforementioned polymers belong to the thermoplastic family. Thermoplastic materials can be repeatedly melted and cooled, being their curing processes 100% reversible as no chemical bonding takes place. This feature allows thermoplastics to be remolded above a specific temperature without negatively affecting the physical properties. They offer high strength, shrink-resistance and flexibility, which are the essential properties of POFs. However, for applications where the fibers are exposed to high-heat environments, thermoplastic POFs may not be suitable as there is a risk of softening at higher temperatures than the Tg. For these kind of environments, thermoset polymers may be of great interest. Thermoset materials contain polymers that cross-link together during the curing process to form a permanent chemical bond. This cross-linking is not reversible and resists melting when heat is applied [48]. The temperature working range for thermoset based fibers could be much wider compared to that of thermoplastic fibers such as PMMA. However, they are more brittle than thermoplastics, and they lose flexibility. The use of thermoset polymers in POFs dates back to the 1990s. However, their research field has not been very active due to the beforementioned drawbacks and the challenges on the POF fabrication process. Figure 2.6 represents the polymer structure differences of thermoplastic and thermoset polymers.

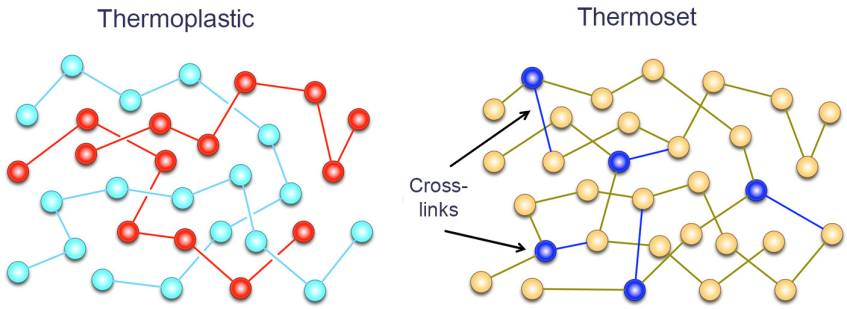

Figure 2.6: Polymer structure differences between thermoplastic and thermoset polymers [49].

2.4 Loss mechanisms in POFs

The transmission losses in an optical fiber limit the distance a signal can propagate through the fiber before it is too faint to be detected. The basic loss mechanisms in a POF are divided into two main groups: intrinsic and extrinsic (see Figure 2.7). Intrinsic losses are inherent to the material of the fiber, hence they are independent from the fabrication process and cannot be eliminated. On the other hand, extrinsic factors such as contaminants or imperfections, depend on the fabrication procedure, and by optimizing this process they can be avoided.

Among the intrinsic losses, *material absorption* and *scattering* can be found. The first contribution is basically caused by the molecular vibrational absorption of the groups C-H, N-H, and O-H, and by the absorption due to electronic transitions between energy levels. On the other hand, the second contribution results from scattering arising from microscopic variations in the material density, orientation, and composition. Regarding the extrinsic losses, they are also divided into *absorption* and *scattering* sources. The first is caused by both metallic and organic contaminants. Whereas, structural imperfections such as dust,

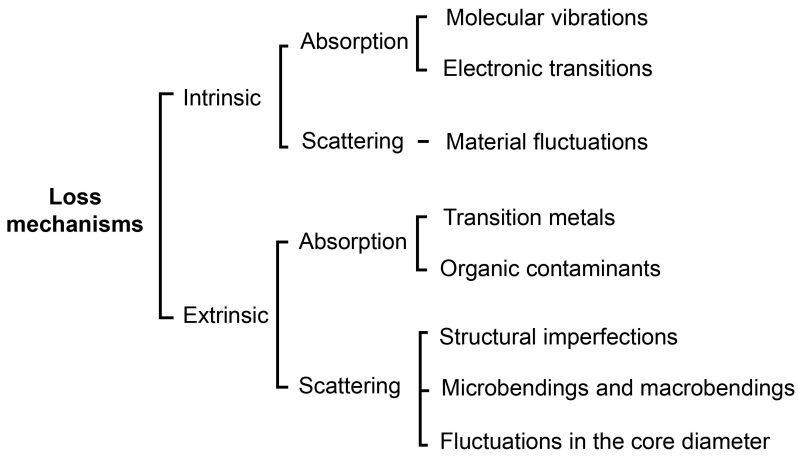

Figure 2.7: Classification of the intrinsic and extrinsic loss mechanisms in POFs

microfractures, and bubbles, are responsible of the scattering losses. Microbendings and macrobendings are also a source of scattering loss. However, they are not significant unless the bending radius is small enough, for example, ten times the fiber diameter. Fibers with small dimensions have usually higher attenuation, as the number of geometrical and structural imperfections caused during fiber fabrication increase. Besides, for smaller diameters the rays strike more frequently on the core-cladding interface, where imperfections are more common. More detailed information about transmission losses can be found in [3].

Chapter 3

Fundamentals of dye-doped POFs

Prologue— *This chapter describes the fundamentals to understand the optical processes behind a dye-doped POF. It starts with the description of the light-matter interactions in organic materials based on a band-like energy model (Jablonski diagram), comprising phenomena such as linear absorption, two-photon absorption, and emission. Different types of emission are detailed, such as spontaneous emission, stimulated emission and amplified spontaneous emission, which is the base of the light amplification in doped POFs. Moreover, a theoretical model to describe light generation and amplification in doped POFs by the so-called rate equations is presented, together with three steady state analytic expressions that will be used along the experimental results of this thesis. Finally, the photodegradation process is introduced, which represents one of the fundamental limitations of doped POFs.*

3.1 Energy level model

The molecular structure of the organic materials and the processes resulted from optical excitation can be adequately described by a band-like energy level model, known as *Jablonski diagram*. A typical illustration of this diagram is shown in Figure 3.1. Based on this model, the dye

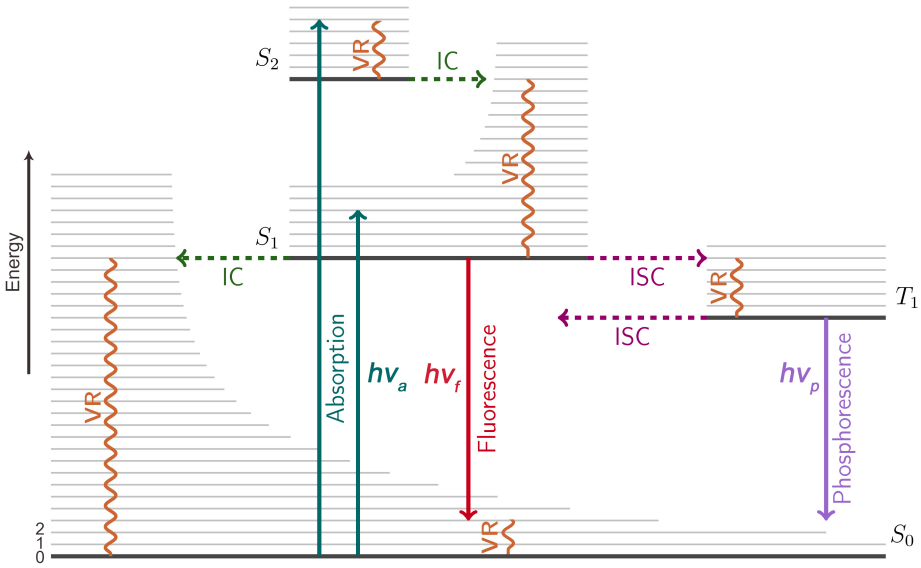

Figure 3.1: Schematic of the Jablonski diagram. $S_i(i = 1, 2, 3)$: singlet states; T_1: first triplet state; VR: vibrational relaxation; IC: internal conversion; ISC: intersystem crossing; hv_a: absorbed energy; hv_f: fluorescence emission energy; hv_p: phosphorescence emission energy.

molecular structure holds two main types of electronic levels, the *singlet* state ($S_i(i = 1, 2, ..., k)$) and the *triplet* state ($T_i(i = 1, 2, ..., k)$), illustrated by bold horizontal lines in the above diagram. The singlet state S_0 is called the *ground state* and it is the predominantly-populated energy level at thermal equilibrium. The energy gap between S_0 and the first excited state S_1 is too large for thermal excitation of S_1, and for this reason, light and no heat is used to induce fluorescence. Each of the

electronic levels consist of a number of vibrational sublevels, depicted by 0,1,2, etc. Based on quantum mechanics, electronic transitions between states with the same spin multiplicity are allowed, i.e., singlet-singlet and triplet-triplet transitions. However, transitions between singlet-triplet and vice versa are highly improbable, and therefore they are called *forbidden transitions* (even though they can be observed due to spin-orbit coupling [50]). From the before described, an incident photon excites, via absorption, a dye molecule that is on thermal equilibrium conditions. The incident photon losses its energy and promotes an electron from the ground electronic state S_0 to a vibrational level of an excited electronic state. The absorbed energy is described by hv_a, h being the Planck constant ($4.136 \cdot 10^{-15}$ eV $\cdot$ s) and v_a the absorption frequency. The excited-state electron undergoes several decay mechanisms until finding itself back to its fundamental state S_0.

The decay mechanisms that a photon may undergo can be divided into two types, *radiative* and *non-radiative* decays. The radiative downward transition generally takes place between the lowest vibrational sublevel of S_1 to one of the vibrational sublevels of the ground state. This process is called *fluorescence* and happens within $10^{-10} - 10^{-7}$ s. However, molecules in the S_1 state can also undergo a spin conversion to the first triplet state T_1, so-called intersystem crossing. The radiative emission from T_1 to S_0 is called *phosphorescence*. As transitions between T_1 ad S_0 are forbidden, phosphorescence is a slow process of around $10^{-6} - 1$ s (also called *delayed emission*). The two types of radiative transitions are illustrated in 3.1 as downward solid lines, and hv_f and hv_p are the emission energies for fluorescence and phosphorescence respectively. The non-radiative transitions are called *vibrational relaxation* (VR), *internal conversion* (IC) and *intersystem crossing* (ISC).

The VR involves a release of the excess of energy accumulated in the

vibrational levels of an excited electronic state upon excitation, unless the absorption happened to the lowest vibrational level of the excited state. It is also a decaying mechanism to the lowest vibrational level of the ground state after a radiative transition (fluorescence or phosphorescence) that ended up in one of the vibrational levels of S_0. It can also happen after a transition between isoenergetic vibrational levels of two different electronic states with similar or different spin multiplicities. All these vibrational relaxation mechanisms are illustrated in Figure 3.1 as vertical waved curves. As a consequence of the energy loss due to VR decays, the energy of the emission is less than that of the absorption, and therefore, fluorescence occurs at longer wavelengths, i.e., the emission is red-shifted with respect to the absorption. However, in most of the cases the absorption and emission spectrum are partly overlapped. This is due to the fact that at room temperature, a fraction of molecules is in a vibrational level higher than 0 in the ground state. The gap between the maximum of the absorption and the maximum of the emission is known as *Stokes shift*. Generally having large Stokes shifts is highly desirable because the reabsorption losses are considerably decreased, leading to, for example, lower thresholds for lasing. Typical timescales of the VR mechanism are on the order of $10^{-12} - 10^{-10}$ s.

3.2 Light absorption

3.2.1 Linear absorption

Absorption of an incident photon can occur when the energy of the photon, hv_a, matches the energy gap between the ground state and one of the excited states of a molecule ΔE, i.e., $\Delta E = hv_a$. When this

happens, an electron is promoted from the ground state to one of the excited states, as can be seen in the schematic shown in Figure 3.2. This mechanism is called *linear absorption*. Usually it starts from the lowest vibrational sublevel of S_0, because the majority of molecules are in this level at room temperature. The maximum absorption wavelength can be calculated as follows:

$$\lambda_{abs} = \frac{hc}{\Delta E} \tag{3.1}$$

where h is the Planck constant and c is the speed of light in vacuum.

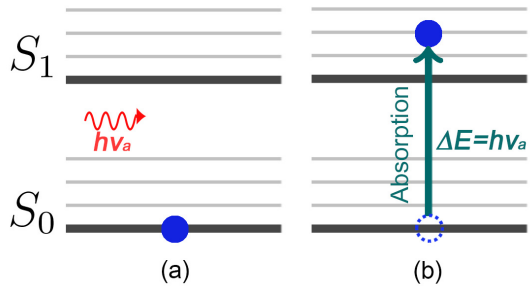

Figure 3.2: Schematic of the linear absorption mechanism: (a) Incident photon of energy $h\nu_a$, and a electron in the ground level. (b) Absorption of the incident photon, and promotion of the electron to one of the vibrational levels of the excited state corresponding to the energy gap $\Delta E = h\nu_a$.

3.2.2 Two-photon absorption

Generally, the energy required to bridge the band gap of a molecule comes from a unique photon of appropriate energy, i.e., one photon is needed per molecular transition (linear absorption). However, it is also possible that two photons that have, at least, half of the band gap energy each, are simultaneously absorbed in a non-linear absorption process, namely two-photon absorption (TPA) [50]. This mechanism occurs at much lower probability than the linear absorption, as it depends on

the square of the light intensity, and thus, it can only dominate at very high excitation intensities (like the ones obtained by focusing the output beam of a pulsed laser). The TPA process is illustrated in Figure 3.3. As can be seen, an electron is promoted from the ground level to one of the vibrational sublevels of S_1 by absorbing two incident photons simultaneously, where the sum of their energies matches the energy band gap ΔE. After this absorption mechanism, the electrons relax very fast to the lowest vibrational sublevel of S_1 and further electronic transitions such as fluorescence can occur, the same as for the one-photon excitation. TPA can be of interest for some applications. For instance, it appears to be a great tool for 3D-fluorescent imaging in human bodies [51, 52].

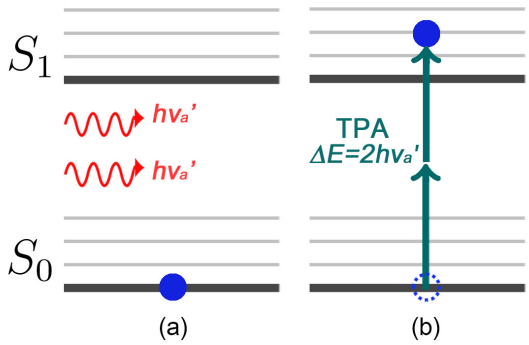

Figure 3.3: Illustration of the two-photon absorption. (a) Two incident photons with energies hv_a', and an electron on its fundamental state. (b) Absorption of the two incident photons and promotion of the electron to one of the vibrational sublevels of the excited state corresponding to $\Delta E = 2hv_a'$.

3.3 Light emission

As seen in Section 3.1, once a photon has been absorbed and an electron has been promoted from the ground state to one of the vibrational sublevels of an excited state, it may undergo several decaying mechanisms

to get itself back to its fundamental state S_0. As $T_1 \rightarrow S_0$ transition is generally forbidden and when it happens it takes longer times than fluorescence (what makes it not optimal for some applications of doped POFs, such as fast amplifiers and switchers), the following descriptions will be based on the radiative transitions $S_1 \rightarrow S_0$.

3.3.1 Spontaneous emission

When a photon reaches the lowest vibrational sublevel of S_1, it may return to its fundamental state S_0 by spontaneously (without external influences) emitting a photon. In general, the photon is emitted incoherently and randomly in all directions, with an energy of hv_f. Figure 3.4 illustrates the spontaneous emission of a photon.

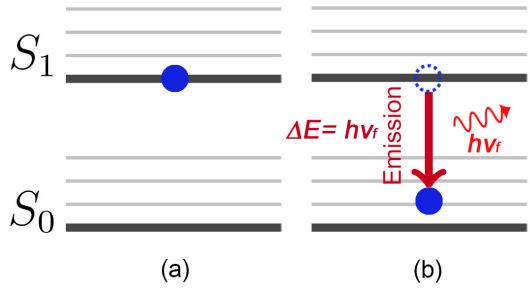

Figure 3.4: Schematic of the spontaneous emission of a photon. (a) An electron in the lowest vibrational level of S_1. (b) Relaxation of the electron to its fundamental state S_0 and random emission of a photon of energy hv_f.

The *lifetime* is a measure of the time an electron spends in the excited state before returning to S_0 by emitting a photon, and it is represented by the parameter τ. If a population of molecules is excited, τ represents the time it takes to the number of excited molecules (N_1) to decay to $1/e$ of the original population, as it is represented in Figure 3.5 (a) [50]. In

the time domain, the lifetime can be directly determined by fitting the emission curve to an exponential decay. Depending on the luminescent dopant, these lifetimes can range from the picoseconds to the milliseconds. In Figure 3.5 (b) an experimental temporal decay of a doped POF is shown, with a lifetime value of 4.84 ns.

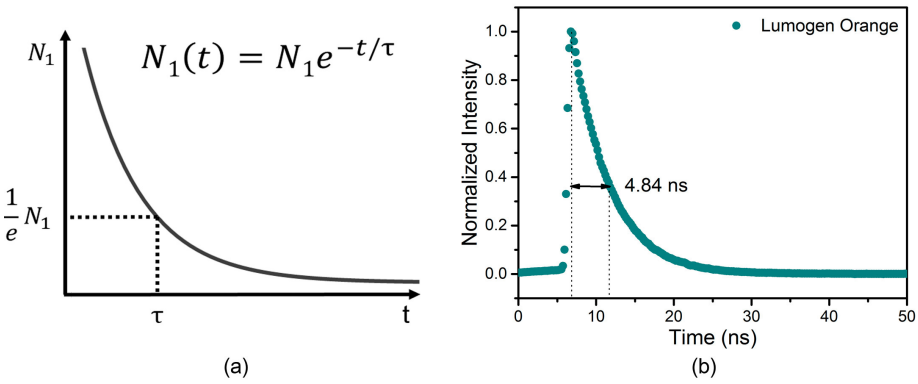

Figure 3.5: (a) Schematic representation of the fluorescence lifetime definition. (b) Experimental fluorescence curve of a lumogen orange doped POF with a lifetime of 4.84 ns.

3.3.2 Stimulated emission

Apart from the spontaneous emission, an excited molecule can also return to its fundamental state via stimulated emission. This is a process where an excited-state species interacts with an incident photon with a certain frequency, and as a result, falls back to the ground state emitting a coherent photon, i.e., same phase, direction, frequency and polarization of the incident photon (see Figure 3.6).

According to the theoretical phenomenon predicted by Albert Einstein, when the population of the excited state is higher than that of the ground state (*population inversion*), it is possible to force atoms to return to the fundamental state by incident photon stimulation, and therefore,

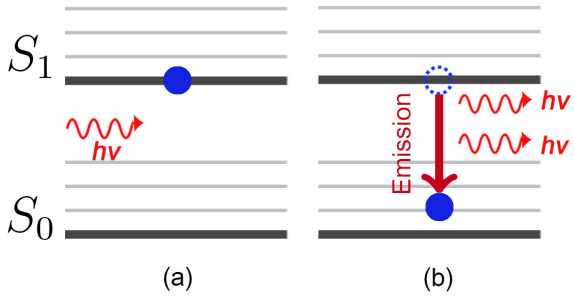

Figure 3.6: Schematic of the stimulated emission of a photon. (a) An electron in the lowest vibrational level of S_1, and the incident photon with energy hv. (b) Relaxation of the electron to its fundamental state S_0 and, coherent emission of a stimulated photon traveling along with the incident photon.

stimulated emission will become the dominant mechanism. The ratio between the population of the ground state, N_0, and the population of the excited state, N_1, is given by the Boltzmann law [50] as follows:

$$\frac{N_1}{N_0} = \exp(-\frac{\Delta E}{kT}) \tag{3.2}$$

where ΔE it the energy gap between the excited state and the ground state, k is the Boltzmann constant ($1.3807 \cdot 10^{-23}$ J/K), and T is the temperature. At room temperature the population of the excited state is less than the population of the ground state, as $\Delta E >> kT$ and the N_1/N_0 relation is vanishing small. External optical pumping is a possible method to obtain population inversion.

3.3.3 Amplified spontaneous emission

ASE is a cascade process where spontaneously emitted photons are amplified by further coherent stimulated emissions. In other words, a spontaneously emitted photon can induce stimulated emission in another excited molecule, leading to a cascade emission process and the amplifica-

tion of the original photon. This mechanism is the fundamental physical process underlying light amplification. In materials with high gain, the ASE occurs without the aid of any resonant cavities or mirrors. As before mentioned, in order to observe ASE, population inversion is necessary, and thus, relatively high pump powers are needed, i.e., above the *ASE threshold energy*. Bellow this threshold, the output energy grows with a small slope, as it corresponds mainly to the spontaneous emission. Above it, population inversion occurs and spontaneously emitted photons are amplified in a single pass through the material.

Typical signatures of ASE are the directionality of the emitted light, a narrowing of the emission spectrum, and an abrupt increase of the emitted light intensty as the pump energy increases. In Figures 3.7 and 3.8 these two characteristics can be seen. The top scheme of Figure 3.7 represents how the transmitted light increases its directonality when the pump energy raises. Below, the evolution of the output spectrum from fluorescence to ASE is shown as a function of the pump power, for a rhodamine 6G doped POF sample. As can be seen, the full width half maximum (FWHM) of the ASE spectrum is narrowed in comparison to the emission spectrum of fluorescence. This fact can be explained because of the nonlinearity of the amplification process where most of the light is emitted over a small range of wavelengths of greater gain [23]. For the same reason, a relative blue-shift of the emission spectrum can be observed. This expresses that greater gains are obtained towards the peak of the emission band, i.e., greater gains are obtained for the shorter wavelengths of the emission spectrum, and therefore, a blue-shift of the average emission wavelength occurs [53].

The ASE threshold can be defined in different ways. For some scientists it is the pump energy required for the FWHM become half of the value observed with low pump energies [54]. Another point of view

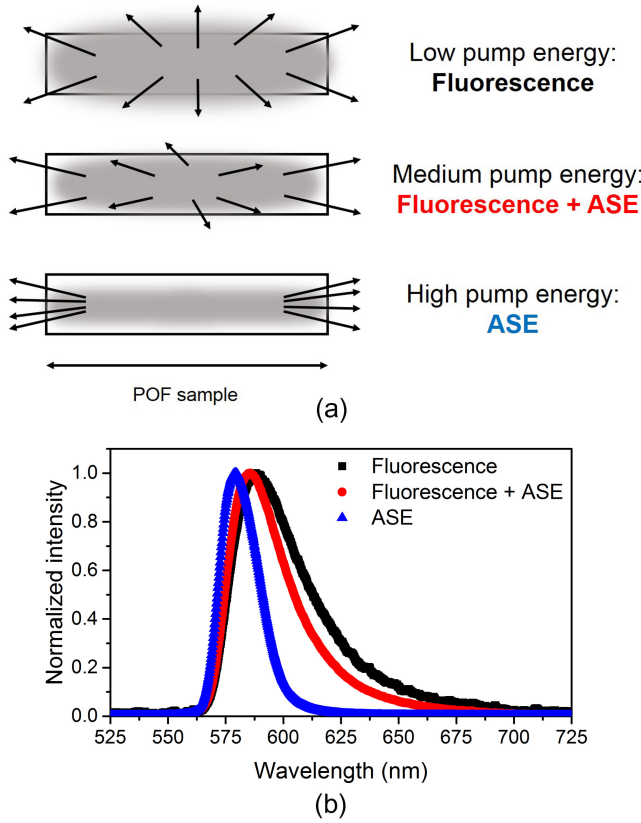

Figure 3.7: Signatures of the ASE. (a) Schematic of the evolution of the directionality of the emitted light in a POF. (b) Narrowing of the emission spectrum from fluorescence to pure ASE as the pump energy is increased. The data points are experimental values for a rhodamine 6G doped POF.

is based on the assumption that once the ASE threshold has been exceeded, the output emission can be considered linearly dependent with the pump power. In that case, the ASE threshold can be defined as the pump power at which the linear curve cuts the x-axis [55]. The slope of this straight line is known as the *slope efficiency*. Both methods are illustrated in Figure 3.8.

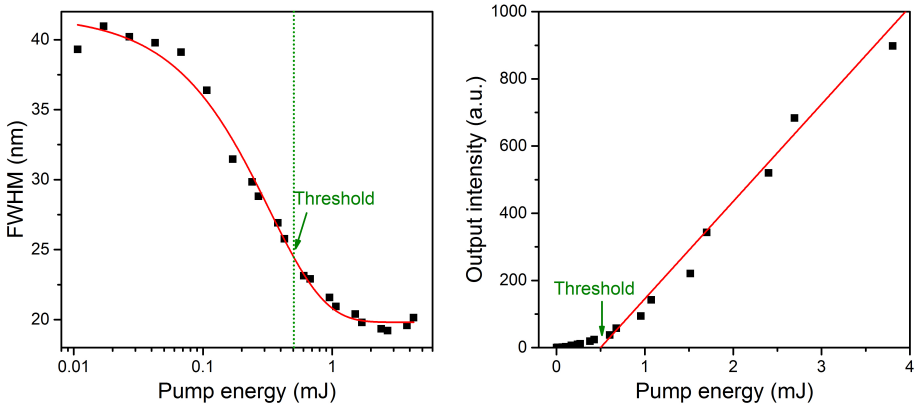

Figure 3.8: Two methods for the calculation of the ASE threshold energy. (a) Method 1: by means of the evolution of the FWHM as a function of the pump energy. (b) Method 2: by means of the evolution of the output intensity as a function of the pump energy. The data points are real experimental values of a rhodamine 6G doped POF.

3.4 Rate equations

Light generation and amplification in active dye-doped POFs can be described by the so-called *rate equations*. As a first approach,the active material is depicted as a two-level system, which is a reasonable simplification for the organic dyes typically employed in POFs [53].

When considering a set-up of longitudinal excitation, the complete system is described by three partial differential equations together with initial and boundary conditions. This model considers that the doped POF is pumped longitudinally at $z = 0$, with the axis of z oriented in the direction of the fiber symmetry axis (see Figure 3.9). Besides, only the light propagating in the positive propagation sense ($z+$) is considered, as the contribution of the light traveling in $z-$ towards the positive sense is much smaller than the directly generated power in towards the detector. To introduce the dependency with wavelength, the range of emission wavelengths of interest is divided into discrete subintervals centered at

λ_k. Possible non-linear effects that could occur at very high power densities, such as the absorption of more than one photon simultaneously, or the decrease of the absorption due to saturation or optical bleaching are not included in this model. The modal dispersion is not taken into account either.

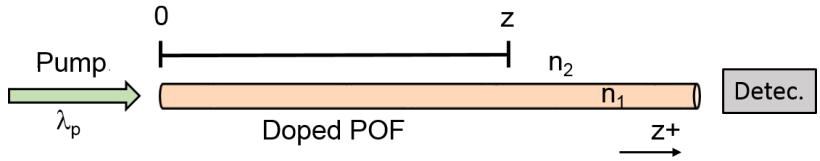

Figure 3.9: Set-up for the theoretical model under longitudinal excitation.

It is assumed that the pump laser illuminates the whole cross section of the fiber, and that the light emission is generated at random directions. A fraction of this randomly emitted light can be guided and propagated towards the fiber end, and therefore contribute to stimulated emissions along the fiber. This fraction is depicted as β, and it is calculated as reported in [53]. In SI fibers, β is constant, though in the case of GI fibers it depends on the radial distance r, as the core refractive index decreases gradually. In any case, $\beta < 1$.

Moreover, if the dopant concentration and the light density distribution change with r, the overlap between both distributions must be taken into account. This is the case of GI fibers as light is more concentrated towards the fiber symmetry axis, where the dopant concentration is also greater. As a consequence, stimulated emissions are favored and its contribution is taken into account by an overlapping factor γ, which is greater than 1. In SI fibers though, $\gamma = 1$ because the dopant concentration is constant and because the power density is uniform along the fiber cross section. The calculation of γ can also be consulted at [53].

The first differential equation governs the evolution of the pump power P_p as follows:

$$\frac{\partial P_p}{\partial z} = -\sigma^a(\lambda_p)N_0 P_p \gamma - \frac{1}{v_z}\frac{\partial P_p}{\partial t} \tag{3.3}$$

The first right hand term considers the absorption of the pump. The product of $\sigma^a(\lambda_p)N_0$ corresponds to the absorption coefficient α_p of the material at λ_p. N_0 is the population of the ground level, and it is defined as $N_0 = N - N_1$, where N is the dopant concentration and N_1 is the excited state population. The last term of the equation represents the propagation of the pump with speed v_z.

The second differential equation represents the variation of N_1 with time as follows:

$$\begin{aligned}\frac{\partial N_1}{\partial t} = -\frac{N_1}{\tau} - \frac{\sigma^e(\lambda_k)}{h(c/\lambda_k)A_{core}}N_1 P\gamma + \frac{\sigma^a(\lambda_p)}{h(c/\lambda_p)A_{core}}N_0 P_p\gamma \\ + \frac{\sigma^a(\lambda_k)}{h(c/\lambda_k)A_{core}}N_0 P\gamma\end{aligned} \tag{3.4}$$

The first term beginning from the right, represents the spontaneous emission, where τ corresponds to the spontaneous lifetime of the dopant in PMMA. The following term takes into account the decrease of N_1 due to stimulated emission, where $\sigma^e(\lambda_k)$ is the stimulated emission cross section at λ_k. The last two terms are related to the absorption of photons of P_p (excitation by the pump) and of P, also known as re-absorption of the emitted light. Reabsorption is commonly much smaller than the pump excitation, as P is normally considerably smaller than P_p, and the re-absorption cross section $\sigma^a(\lambda_k)$ is also smaller than the pump absorption cross section $\sigma^a(\lambda_p)$. A_{core} is the cross section of the fiber core, and h is the Planck constant.

Lastly, the differential equation to calculate the evolution of P through the fiber for each of the λ_k is given by:

$$\begin{aligned}\frac{\partial P}{\partial z} = \sigma^e(\lambda_k)N_1 P\gamma - \sigma^a(\lambda_k)N_0 P\gamma - \frac{1}{v_z}\frac{\partial P}{\partial t} \\ + \frac{N_1}{\tau}\left(h\frac{c}{\lambda_k}\right)\sigma^e_{sp}(\lambda_k)\beta A_{core}\end{aligned} \tag{3.5}$$

The first right-hand term considers the emissions stimulated by the incoming photons. The next term represents the attenuation due to material absorption. The third term depicts the propagation of the emitted light power inside the fiber with speed v_z. And finally, the last term represents the spontaneous emissions, where $\sigma^e_{sp}(\lambda_k)$ is the probability for spontaneous emission to take place at the wavelength subinterval around λ_k. Above the ASE threshold this last term is much smaller than the contribution of the stimulated emissions, though it is necessary to illustrate the appearance of the first photons in the light amplification.

As mentioned before, this model only considers the light propagating in the positive propagation sense ($z+$). However, when the fiber is excited transversally, as for example when employing the variable stripe length method for gain calculation, both propagation directions must be taken into account, i.e., towards the detector in the positive z direction and also towards the opposite end of the fiber ($z-$) (see Figure 3.10).

Therefore, in the transversal excitation, P^+ represents the light power propagating in the $z+$ direction, and P^- corresponds to the light power propagating in the $z-$ direction. P^- itself will not reach the detector, but it may excite molecules whose spontaneous and stimulated emissions contribute to the increasing of P^+. Therefore, the evolutions of N_1, P^+

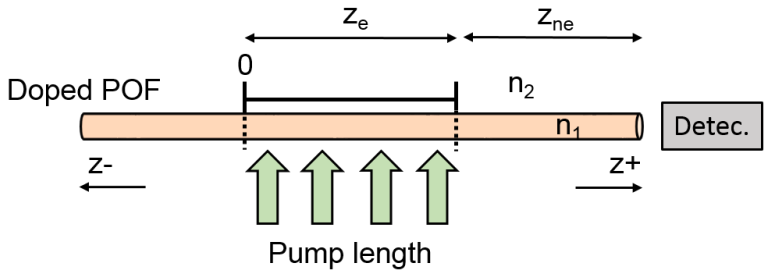

Figure 3.10: Set-up for the theoretical calculations when transversal excitation is employed. z_e: Illuminated fiber length and z_{ne} non-excited fiber length.

and P^- are represented in the transversal excitation as follows [6, 56]:

$$\frac{\partial N_1}{\partial t} = -\frac{N_1}{\tau} - \frac{\sigma^e(\lambda_k)}{h(c/\lambda_k)A_{core}} N_1 P^{\pm}\gamma + \frac{\sigma^a(\lambda_k)}{h(c/\lambda_k)A_{core}} N_0 P^{\pm}\gamma \tag{3.6}$$

$$\begin{aligned}\frac{\partial P^{\pm}}{\pm\partial z} = \sigma^e(\lambda)N_1P^{\pm}\gamma - \sigma^a(\lambda)N_0P^{\pm}\gamma - \frac{1}{v_z}\frac{\partial P^{\pm}}{\partial t} \\ + \frac{N_1}{\tau}\left(h\frac{c}{\lambda}\right)\sigma^e_{sp}(\lambda)\beta A_{core}\end{aligned} \tag{3.7}$$

Equation (3.7) itself represents two equations in which the symbol $\pm$ denotes + or –, depending on the propagation direction of light.

The contribution of the P_p in transversal excitation is introduced as the boundary condition, taking into account that the fiber is pumped transversally with an illuminated length z_e by a temporal Gaussian pulse whose effective width is σ, given by the following equation:

$$P_p(t) = \frac{E_{p,max}(z_e/z_{e,max})}{\sigma\sqrt{2\pi}} e^{\frac{-(t-t_{peak})^2}{2\sigma^2}} \qquad (for\ z\ \epsilon\ [0, z_e]) \tag{3.8}$$

where $E_{p,max}$ is the maximum pulse energy on the fiber, i.e., the energy at $z = z_{e,max}$, and t_{peak} corresponds to the instant of maximum lasing power. With regard to the initial conditions, it is assumed both that no light is propagating through the fiber ($P(z = 0) = 0$)) and that there is no excited population at $t = 0$.

3.4.1 Analytic expressions in steady state

By working out the previous equations for transversal pumping configuration in steady state, the evolution of the fiber output power can be determined both for fluorescence regime and gain regime. This later occurs when the optical gain exceeds the optical losses caused by self-absorption, light scattering from fiber imperfections, and other factors.

First, the output power evolution in fluorescence regime (losses > gain) as function of the non-exited fiber length z_{ne} is obtained from equation (3.7) and the boundary condition $P(z_{ne} = 0) = P_0$, and is given by:

$$P(z_{ne}, \lambda) = P_0 \; e^{-\alpha(\lambda) z_{ne}} \tag{3.9}$$

where $\alpha(\lambda)$ is the attenuation coefficient corresponding to a wavelength λ. The units of the attenuation coefficient are m^{-1}, though it can also be given in dB/cm from the following relation $\alpha(dB/cm) = 4.24 \; \alpha(cm^{-1})$. Equation (3.9) matches with the well-known Beer-Lambert's law, where the power of light decreases exponentially as it travels inside an active material.

Secondly, the output power evolution as function of the illuminated fiber length z_e on fluorescence regime is obtained from working out equation (3.7) and with $P(z_e = 0) = 0$ as boundary condition. It is expressed

by:

$$P(z_e, \lambda) = \frac{C}{\alpha(\lambda)}(1 - e^{-\alpha(\lambda) z_e}) \tag{3.10}$$

where C is a constant related to the spontaneous emission given by $C = N_1 A_{core} \sigma_{sp} \beta (hc/\lambda)/\tau$. This variation of the output power with z_e provides a saturation power of $C/\alpha(\lambda)$.

Finally, when gain exceeds losses, the evolution of the output power is also obtained from equation (3.7) and $P(z_e = 0) = 0$, and is given by the following expression:

$$P(z_e, \lambda) = \frac{C}{g(\lambda)}(e^{g(\lambda) z_e} - 1) \tag{3.11}$$

where $g(\lambda)$ is the gain coefficient at the considered emission wavelength λ. This equation describes the variation of the output power before reaching gain saturation. For the two-level system considered, the gain coefficients are expressed in terms of populations as:

$$g(\lambda) = [N_1 \sigma^e(\lambda) - N_0 \sigma^a(\lambda)]\gamma \tag{3.12}$$

Figure 3.11 illustrates the evolution of the power emitted in the fiber in the three cases presented before:

3.5 Photodegradation

Exposure to sunlight and to artificial light sources such as lasers, can have adverse effects on the useful life of dye-doped POFs. Long exposures may involve photochemical modifications of the fluorophore, resulting in

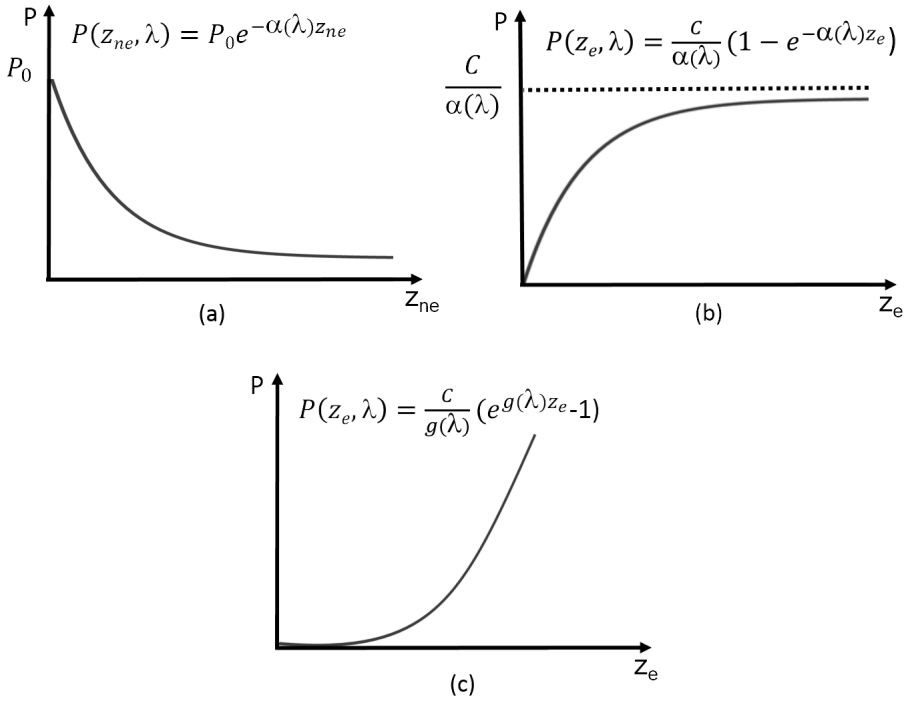

Figure 3.11: Evolution of the power through a fiber for (a) fluorescence regime as function of z_{ne}, (b) fluorescence regime as function of z_e, and (c) under presence of a positive gain as function of z_e.

the loss of its ability to emit light [57]. Oxygen is well known to be a catalyst for chemical modifications in molecules under the presence of light. It has been demonstrated that if a dye is protected from reaction with environmental molecular oxygen, the observed rate of photodegradation is lower [58, 59]. It has also been found that other parameters may also affect the photostability of a doped POF, such as the temperature, the pump frequency and the excitation intensity [57, 60]. Unfortunately, reducing photodegradation by lowering the excitation intensity leads to a reduction of the fluorescence signal, what makes the doped POF-based application less efficient [59]. Good strategies are, for example, selecting a highly stable dopant, and reducing the presence of oxygen on the sample by optimizing the fabrication process. It may also be noted that the

photostability of the dopants is further reduced under ultraviolet excitation. Finding fuorophores that work on higher wavelengths may reduce the photodegradation. In most cases the degradation of the fluorophores is irreversible. Even though, in some cases, a fluorescent molecule can be switched on again after a period of time under rest (dark state), what is called *self healing* or *recovery* [59, 57, 11]. The decay and the recovery of the emission generated in doped-polymers is nowadays being studied by the research group led by M.G. Kuzyk [61, 62]. In particular, they have shown that it may be possible to design dye-doped polymer devices with high damage threshold with the use of an electric field [62]. In Figure 3.12 a photograph of two permanently degraded POF samples is shown. As can be seen, the photodegradation for the whole excited length was so strong that it is even visible to the naked eye.

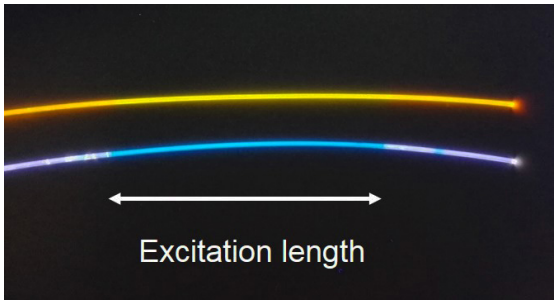

Figure 3.12: Illustration of the photodegradation that two POF samples underwent under continuous exposure to a solar simulator excitation for a specific excitation length.

Chapter 4

ASE features and gain phenomena in doped POFs

Prologue— *This chapter starts with an overview of the state-of-the-art of doped POFs in the field of POF light sources and amplifiers. Afterwards, the experimental methods and set-ups are described. Finally, results concerning ASE effects and optical gain in rhodamine-6G doped POFs are presented. The first one corresponds to two gradded-index PMMA fibers of different dopant concentrations, whereas the second one is based on two step-index thermoset fibers with the same concentration, with and without cladding. The analysis carried out includes the dependence of the ASE performance with the pump energy, with the excited fiber length, and with the pump polarization. Two-photon emission is also reported for the SI thermoset POFs.*

4.1 General background

The potential of doping POFs with a wide variety of functional materials, opened a versatile range of new applications in the fields of lasers, amplifiers, illuminators, switches and sensors in the visible region. Active POFs present a number of advantages over their glass counterparts. One the one hand, mechanical strength is higher, and the fabrication technology is simpler and cheaper. One the other hand, the much lower manufacturing temperatures of POFs (around $200°C$ compared to the $1000°C$ of glass fibers) makes it possible to embed into their core a variety of functional dopants, ranging from organic dyes [53, 63, 64] or conjugated polymers [65, 66], to rare earth ions [67, 68], quantum dots [69, 70] and noble-metal nanoparticles [71, 72]. These can be readily employed to tailor the optical, electrical and magnetic properties of the host fibers with great versatility. Besides, the fiber-waveguide structure provides several added benefits, such as optical confinement in the core area, long interaction distance between the light and the gain medium, symmetric output of the beam profile, good adaptability to fiber-optic communication systems and high ratio between surface area and volume, which allows efficient heat dissipation and minimization of thermal degradation.

Fiber light sources have proven to be useful in many-purpose standalone applications. POFs lasers are especially attractive as light sources in LAN applications since they can be easily coupled to a POF system in a similar way as the passive fibers are connected to one another. If the numerical aperture of the POF laser matches the numerical aperture of the POF system, the coupling between the two parts is straightforward, what considerably reduces the coupling losses between the light source and the optical fiber. Besides, in an optical fiber, as in any data trans-

mission cable, the transmitted signal can be significantly weakened over distance due to a number of attenuating factors, such as host absorption, light scattering or bending losses. Therefore, the loss of energy must be compensated, and the signal has to be restored in a manner that keeps its structure unchanged. A possibility to restore the optically transmitted information would be done by decoupling the light from the fiber, converting in to a electrical format, and finally, coupling it again into the fiber with a stronger intensity. However, this is a slow and costly method. A faster, cheaper and more efficient method is to employ an inline POF-based amplifier, and amplifying the signal as it travels through the fiber link. Signal amplification is also crucial in short haul POF data networks with many nodes and in high bandwidth telecommunication systems where WDM technology is used. The spectral broad-gain of POF amplifiers can be used to amplify all the channels in a WDM system with approximately the same gain. The flexibility afforded by doped polymers can be used to make a large number of all-optical fiber photonic components [23, 73].

Light generation and amplification in doped POFs has been obtained by doping the fibers with different functional materials. These are generally added before the polymerization stage in preform fabrication. Nowadays, many choices of dopants are available, resulting in amplification that covers a wide range in the visible and part of the near-infrared regions. As reported by Tagaya *et al.* in [74] the dopant used in a POF must meet five criteria to provide an optimum lasing and amplifying performance. (a) The dopant must have high fluorescent quantum efficiency in the selected polymer host, as this feature is directly related to the probability of stimulation emission; (b) The dopant must be highly photostable, as relatively high excitation intensities and cycles are required for light amplification; (c) There must be a minimal overlap between the dopant emission and absorption spectra, because amplification

rarely occur within the region of spectral overlap due to self-absorption phenomena; (d) The dopant molecules must absorb the radiation of the pump source and must maintain the population inversion required for stimulated emissions to happen; and (e) The dopants must have the proper solubility and thermal stability in the selected polymeric host.

Conjugated polyemers show interesting properties. For example, whereas dye-doped fiber lasers and amplifiers have to be pumped optically, conjugated polymers open the possibility of electrical pumping in the future, since they are capable of charge transport [75]. However, the gains reported for some conjugated polymers were much smaller than those achieved with organic dyes. The main reason of this could be because organic dyes present higher absorption and emission cross sections, and because they can generally be dissolved in greater concentrations in the host medium, what leads to higher gains. On the other hand, rare earth ions show exceptional photostability and narrow emission bands, and they have extensively been studied as dopants in glass fiber amplifiers [76, 77]. However, they are insoluble in polymer matrices what leads to the need to use organic ligands to make them compatible with polymer hosts. Besides, the fiber lengths required (several meters) for attaining optimum gain are longer than those needed with organic dyes. In light of the foregoing, organic dyes appear to be great candidates for efficient lasing and amplification. Among the extensive variety of organic dyes available, rhodamime dyes and their derivatives are widely used [78, 79, 53]. They have been studied in diverse areas of research and for commercial purposes due to their good fluorescent properties. Rhodamine 6G (R6G) is one of the most efficient fluorescent dyes, on which studies are continuously being carried out without interruption from the middle past century. It has frequently been investigated in solid-state lasers and amplifiers in a variety of different hosts, due to its high fluorescence quantum yield (0.95), low intersystem crossing rate, and its

high photostability compared to other organic dyes [80].

It was in 1988 that the first demonstration of lasing emission in a dye doped POF was demonstrated by Muto et al. [81]. In this work, they measured an slope efficiency of 10% at 435 nm employing a SI PMMA fiber of 2 cm doped with R6G. Since that first demonstration, many research has been carried out involving doped POFs as light sources. If a resonant optical cavity (a pair of mirrors on either end of the gain medium) is used, the light source is *laser radiation* and a *fiber laser* is obtained. A Fabry-Perot resonator constructed with a dielectric mirror butted to a fiber end was used to get lasing emission in several works [63, 78]. In a comparative study of the laser features between rhodamine-doped POF lasers and conventional bulk lasers it was demonstrated that the efficiency is higher and that the energy threshold is lower for fiber lasers [63]. On the other hand, in doped fibers with high gain, amplified spontaneous emission can also occur without the aid of a resonant cavity [79, 82, 83, 84, 85]. ASE presents some of the signatures of laser radiation, such as spectral narrowing, existence of a threshold-like energy and directionality. However, since ASE has not been spectrally filtered by a resonator, the output bandwidth is broader than the typical laser radiation, usually a few to a few tens of nanometers. This property makes these doped POFs suitable as light sources in applications where low coherence light is used, such as low coherence interferometry, imaging, sensing or fiber gyroscopes [86, 87, 88]. These kind of light sources are distinguished from the fiber lasers by denoting them as *ASE fiber lasers* or *mirrorless fiber lasers*. In recent years, ASE effect have been detected in SI POFs doped with several organic dyes of different concentrations by pumping the fibers either longitudinally and transversally. In the work carried out by Maier et al., it was shown the lasing efficiency for a transversely pumped rhodamine 11 B-doped fiber achieved 36% [84]. Besides, multimode laser emission was reported in a polymer optical fiber

doped with a mixture of R6G and rhodamine-B dyes, where it was confirmed that the optical feedback for the gain medium was provided by the cylindrical structure of the optical fiber, which acts as a cavity [79]. Theoretical and experimental analysis of the properties of ASE in a R6G doped GI POF was reported for the first time in 2013 by Illarramendi et al. [85]. The authors demonstrated that a theoretical model based on the laser rate equations could serve to describe successfully the spectral ASE features and their dependence with the fiber length. In the field of doped mPOFs ASE effect was observed for a 100 μm diameter and 5 cm long R6G doped fiber, obtaining a linewidth of 5 nm at 569 nm [89]. In this same work, a maximum gain of 30.3 dB was measured at 574 nm using a 2 m of the same doped mPOF with pump pulsed of 325 μJ at 532 nm. ASE performance has also been studied for new structures of doped POFs, such as nanoscale fibers [90, 91, 92] or hollow fibers [93, 94]. Nanoescale fibers fabricated by means of the electrospinning technique are also fully compatible with organic dyes, rare earth ions, conjugated polymers, and nanocrystal dopants [95, 96, 97]. A review focused on the fabrication, the characterization and the applications of doped polymer optical nanofibers is reported in [98]. Multimode laser emission has been recently observed from a R6G doped hollow POF by transverse pulsed photo-excitation [94]. Although there are some studies regarding two-photon emission of doped POFs [99, 100], only the work conducted by He et al. in 1996 reported up-converted laser radiation, where they demonstrated up-converted cavity lasing at 610 nm in a dye-doped POF under nanosecond excitation at 1064 nm [99]. Random lasing in a doped POF was demonstrated for the first time in 2013 [101], opening a window to new research and applications of these disordered systems as optoelectronic integrated devices and optical sensors.

The first POF amplifier was reported by Tagaya *et al.* using a rhodamine-B doped GI POF [102]. In that work, a maximum gain of

27 dB was obtained at 591 nm with a short fiber length of 0.5 m pumping with the second harmonic of a nanosecond Nd:YAG laser. In 1996, Peng et al. first demonstrated optical amplification in a rhodamine-B doped SI POF obtaining a net optical gain of 23 dB at 620 nm in a 90 cm fiber [103]. In the following years, researchers from all over the world have tried to improve the amplification features of POF amplifiers [74, 64, 67, 104, 105]. A possible way to improve the optical gain can be by increasing the dopant concentration in the core material. However, if the dopant concentration is increased up to the saturation limit, this could lead to aggregation of the active material and thereby increase the losses in the fiber. Another possible way to enhance the amplification features could be by embedding different dopants in the core material, in order to shift the wavelength of the maximum gain into the low attenuation windows of the PMMA material. In the work carried out by Tagaya et.al in 1997 amplification characteristics of a wide range of organic dyes were studied [64]. It is worth mentioning the gain characteristics achieved for the organic dopants R6G and oxazine-4, since the maximum amplification was tested at wavelengths close to the most used transmission window of PMMA POFs, i.e. at 650 nm. Signal gain was also detected in a SI POF doped with $Eu(DBM)_3Phen$ at 613 nm, what proved the potential of POFs doped with rare-earths as optical active devices [67].

4.2 Experimental methods

The different experimental methods employed in this chapter are addressed in this section.

- **Measurement of the absorption spectrum**

The absorption curves of the doped POFs were measured at room temperature employing a CARY 50 UV-VIS spectrophotometer equipped with a fiber-optic accessory. The sample lengths were about 1 cm so that the absorption bands of the dyes embedded in the fiber cores could be correctly detected avoiding saturation.

- **ASE Vs pump energy**

The set up employed for the study of the ASE features as function of the pump energy is illustrated in Figure 4.1. This figure also shows a photograph of a doped POF sample in the positioning system. As can be seen, the samples were transversally excited with the output beam of a frequency doubled 10 Hz Nd:YAG nanosecond laser (EKSPLA NL301HT) with an excitation wavelength of 532 nm. This source emits approximately Gaussian pulses with temporal width at half maximum of 20 ns. The excitation energy was controlled employing neutral density filters. The pump beam was expanded and collimated by means of two optical lenses (L1 and L2), and a cylindrical lens (L3) was used to convert the circular beam spot into a narrow stripe of 1 mm in height and a specific excitation length, z_e.

- **Pump polarization dependence analysis**

The electric-field polarization of the pump was controlled by two Glan-Laser Calcite polarizers with high resistance to laser damage (Newport 10GL08AR.14) (P1 horizontal polarizer and P2 vertical polarizer), and by a zero-order precision half-wave plate $\lambda/2$ (Newport 05RP32-532). These are depicted in Figure 4.1 inside a dashed red square, as it is a removable element of the set-up only used for the pump polarization

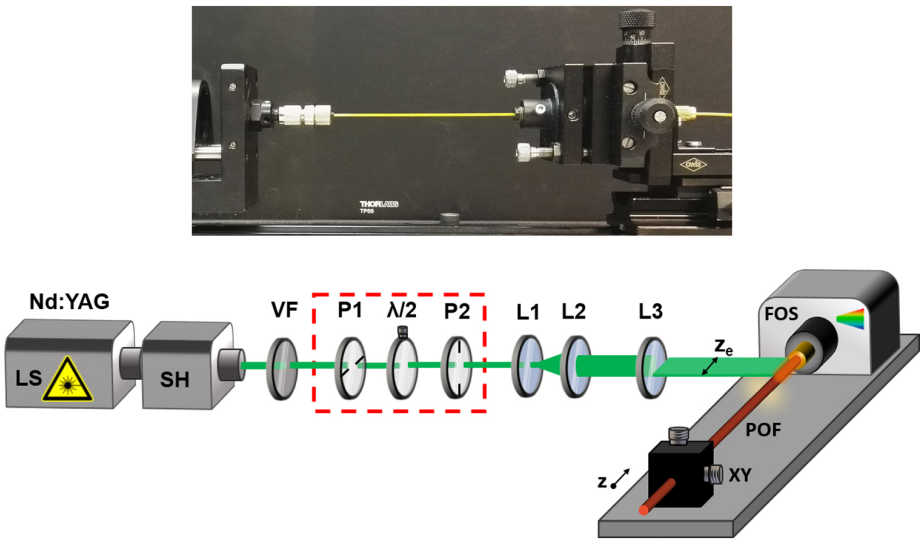

Figure 4.1: Illustration of the experimental set-up for the study of the ASE features employing transversal excitation. LS: laser source; SH: second harmonic generator; VF: variable neutral density filters; P1: horizontal polarizer; $\lambda/2$: half-wave plate; P2: vertical polarizer; L1: divergent lens; L2: convergent lens; L3: cylindrical lens; z_e: length of the excitation stripe; XY: XY positioner; FOS: fiber-optic spectrometer. Inset: photograph of the fiber positioning system.

analysis. By means of these three elements, the polarization of the excitation beam can be switched from horizontal to vertical. Figure 4.2 shows the reference system for the fiber axis and the two pumping polarizations.

- **Gain calculation: variable stripe length method**

The optical gain was measured employing the variable stripe length method (VSL). This method was first described by Shaklee and Leheny during the seventies [106], and since then it has been widely used due to its simplicity and advantages over other methods (no special sample preparation is needed and transparent or opaque samples can be studied) [107]. In this technique the active POF is transversally excited by a

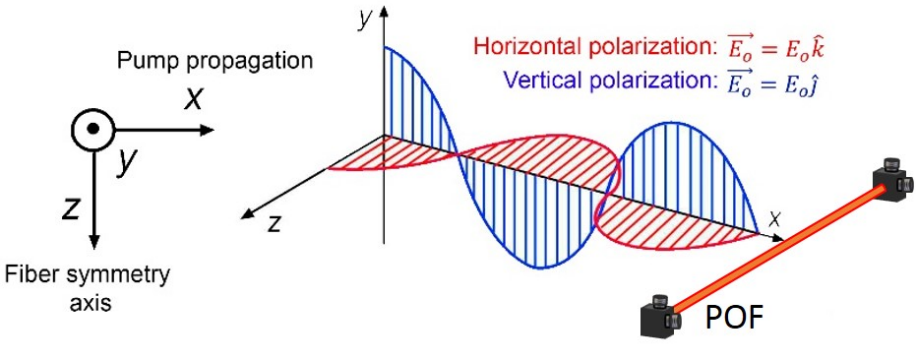

Figure 4.2: Reference system showing the fiber axis (z), the light propagation direction (x) and the vertical and horizontal pump polarizations.

narrow stripe of light, which is obtained by focusing the pump beam through a cylindrical lens. The excitation length, z_e, can be varied from 0 to a maximum value, $z_{e,max}$, by means of an adjustable slit controlled by a micrometer drive. The emission signal, $I(z_e)$, is collected at one of the fiber ends as a function of z_e. For the implementation of this technique, an adjustable slit was added to the set-up from Figure 4.1 after the cylindrical lens (L3), so that an ASE signal is collected at one of the fiber ends as a function of z_e in the range between 0 and $z_{e,max}$. An illustration the VSL technique is shown in Figure 4.3.

The gain coefficients are experimentally calculated by recording the output intensity at a desired wavelength λ as a function of z_e, and by fitting the obtained experimental points to equation (3.11). The values calculated by using the VSL method correspond to the net gain, which is the material gain minus the propagation losses.

- **Optical losses: side illumination technique**

The evolution of the output emission as function of the non-exited fiber length z_{ne} was measured employing the side illumination technique

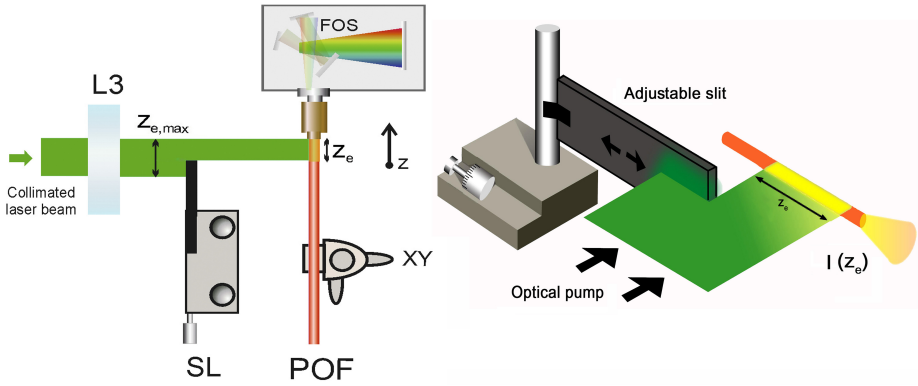

Figure 4.3: Illustration of part of the experimental VSL set-up used for gain measurements (left): L3: cylindrical lens; SL: variable slit; $z_{e,max}$: maximum excitation length; z_e: length of the excitation stripe; FOS: fiber-optic spectrometer. A detail of the VSL method (right).

(SIT) by mounting the fiber positioning system and the detector on a motor-driven linear stage. By controlling the position of the linear stage, the excitation point in the fiber is moved further from the detector, and by collecting the output emission at each position, the dependency of the emission with z_{ne} is obtained. An illustration of this set-up is shown in Figure 4.4.

The optical loss coefficients were calculated by measuring the decrease of the intensity of the fluorescence spectra as the z_{ne} increases, and by fitting the experimental points to equation (3.9) for each of the wavelengths of interest. By plotting the attenuation coefficients as function of λ, the attenuation curve is obtained.

- **Two-photon emission**

For the TPA fluorescence analysis, the samples were optically pumped using a tunable ultrafast femtosecond laser (Spectra-Physics Mai Tai HP) with a wavelength range from 690 nm to 1040 nm and 80 MHz of rep-

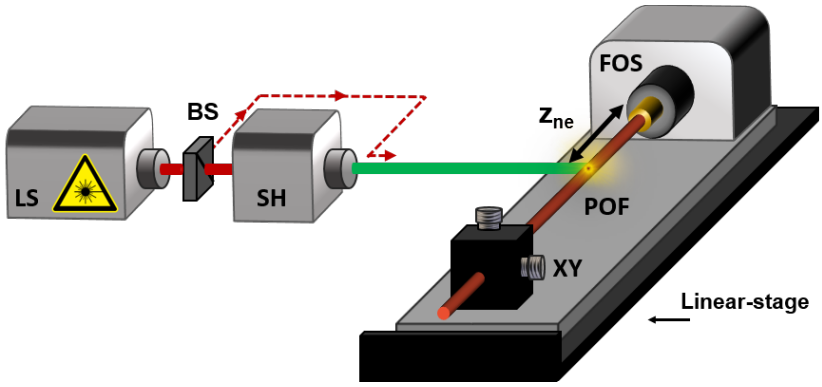

Figure 4.4: Experimental set-up for the analysis as function of the non exited fiber length z_{ne}. LS: laser source; BS: beam splitter; SH: second harmonic generator; XY: XY positioner; FOS: fiber-optic spectrometer. The dashed line represents the possibility of direct excitation from the laser source.

etition rate. This source emits Gaussian pulses with a temporal width of about 100 fs. A convergent lens with a focal length of 8 cm was used in order to concentrate all the pumping energy at a point on the fiber (as very high pump irradiances are needed for TPA). In order to remove the pump power that could propagate through the fiber, a 10SWF-800-B short-pass filter with a cut wavelength of 800 nm was inserted in a filter holder placed between the fiber end and the spectrometer. Figure 4.5 illustrates the set-up used for the TPA measurements together with a photograph of a sample fiber in the positioning system.

- **Output emission detection**

The output emission at one of the fiber ends was measured employing a fiber-optic spectrometer (Ocean Optics USB4000) with an optical resolution of 1.5 nm of FWHM. In all the measurements the emission propagates through a non-excited length of 3.3 cm before reaching the detector. This length corresponds to the size of the SMA fiber connector.

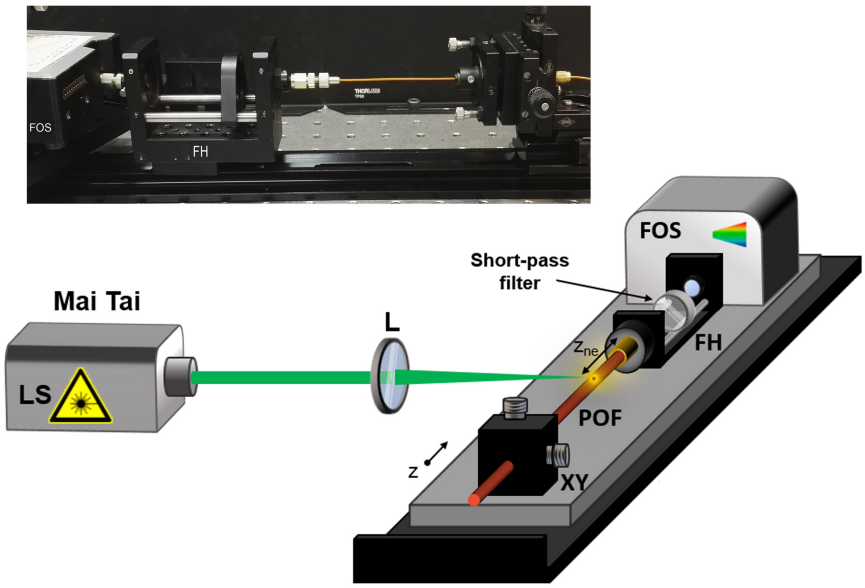

Figure 4.5: Experimental set-up for two-photon fluorescence measurements employing transversal excitation. LS: laser source; L: convergent lens; XY: XY positioner; FH: filter holder; z_{ne}: non-excited fiber length; FOS: fiber-optic spectrometer. Inset: photograph of a sample fiber in the positioning system.

4.3 Result 1: ASE and gain study employing R6G doped gradded-index PMMA POFs

In this study the properties of the amplified spontaneous emission in R6G doped PMMA GI POFs of two different dopant concentrations were analyzed, both as function of the pump energy and as function of the excited length. The pump polarization effects on the fiber emission properties were studied exciting the fiber with horizontal and vertical polarizations. Besides, the optical gains were determined employing the VSL method, and their dependence on the dopant concentration and pump polarization was analyzed. A comparison between the values of optical gain and loss, and a theoretical calculation of the evolution of the local gain are also carried out.

4.3.1 Samples

The fibers studied are two GI PMMA POFs doped with R6G in their core. Figure 4.6 illustrates the refractive index profile and the dye radial distribution of these samples. As can be seen, the variation of the refractive index is the typical one from GI POFs, which decreases gradually with the radial distance. The dopant concentration is also non-uniform, with greater concentration at smaller radial distances. The average dopant concentration is 12 ppm in one fiber, and 16 ppm in the other. These fibers were obtained from a collaboration with the research group led by Prof. Koike from Keio University in Japan. They were manufactured employing a interfacial-gel polymerization technique, in which a low refractive index monomer (methyl methacrylate, MMA) is mixed with the R6G and with an unreactive component with a high refractive index (bromobenzene) to get a gradient index in the radial direction. To obtain a PMMA cladding, a PMMA tube whit outer and inner diameters of 10 and $6-7$ mm was filled with the mixture, forming the fiber preform. Finally the preform rod was heat-drawn to a fiber at a furnace temperature of around $180-220$°C. Further details of the manufacturing technique can be found in [64, 108]. The core diameters of the two fibers analyzed are 0.58 mm and 0.71 mm for the 12 ppm and 16 ppm samples respectively. The total fiber diameter including the cladding is 1 mm in both cases. For both fibers, the refractive index at the fiber symmetry axis is $n_1 = 1.501$, and it decreases to $n_2 = 1.492$ in the cladding (see Figure 4.6). Figure 4.7 shows two microscope images of transversal cuts of the two analyzed fibers, and their main characteristics are summarized in Table 4.1.

The absorption bands of each of the R6G-doped fibers are presented in Figure 4.8. The main bands correspond to the dominant transition from the ground state S_0, to the first excited singlet state S_1, and they

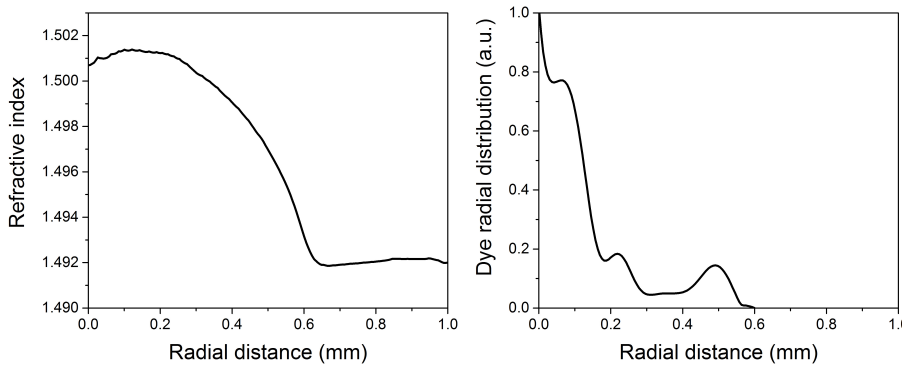

Figure 4.6: Refractive index (left) and normalized dye radial distribution (right) in a R6G doped fiber core as functions of the radial distance. (Data provided by Keio University).

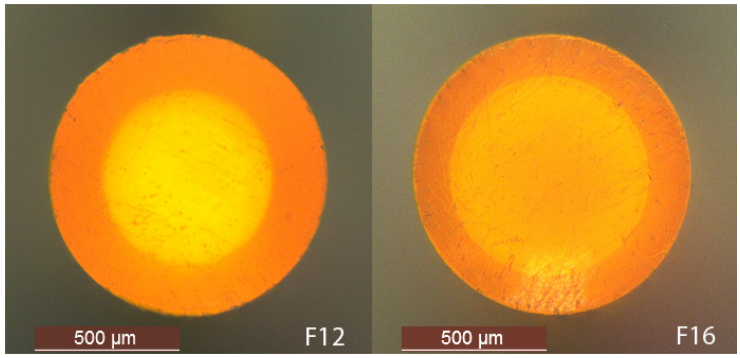

Figure 4.7: Microscope images of the transversal section of the two analyzed GI PMMA POFs, the fiber with the lowest dopant concentration (F12) on the left, and the fiber with the highest dopant concentration (F16) on the right.

Table 4.1: Summary of the characteristics of the R6G doped PMMA GI POFs.

Fiber code	Type	Host	Average concentration (ppm)	Core ⌀ (mm)	Total ⌀ (mm)
F12	GI	PMMA	12	0.58	1
F16	GI	PMMA	16	0.71	1

are located approximately in the spectral region between 490 nm and 550 mm. The flattened shape of these bands can be explained from the contributions of dye aggregates formed at the employed dopant concentrations that tend to broaden the absorption band. This flattering has also been reported in previous works with R6G-doped PMMA rods [109]. The transition from S_0 to the excited singlet state S_2 can also be seen in both fibers as a much weaker absorption band around 350 nm. It has to be noted that this absorption band is superimposed on the ultraviolet absorption curve of the PMMA host. As could be expected, the fiber with the highest dopant concentration shows higher absorption coefficients. Figure 4.8 also illustrates the normalized fluorescence spectrum of the F16 sample, corresponding to the transition from S_1 to S_0. The maximum of this emission curve is located at around 588 nm. It should be noticed that there exists an overlap between the absorption and fluorescence spectra. This fact will cause a red-shift in the emission spectrum when the distance traveled by light inside the fiber increases.

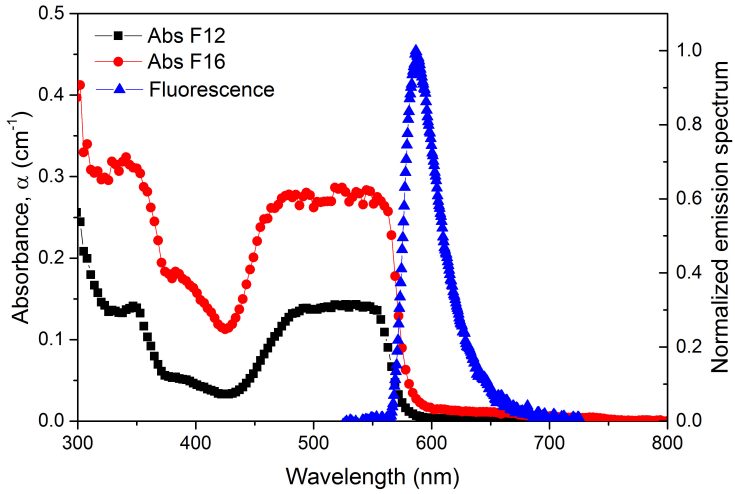

Figure 4.8: Spectral absorption coefficients (α) corresponding to F12 and F16 fibers measured employing a CARY 50 UV-VIS spectrophotometer, and normalized fluorescence spectrum of F16 sample under Nd:YAG 532 nm excitation. ($z_e = 1.2$ mm).

4.3.2 ASE features Vs pump energy

In this experiment the ASE performance of F12 and F16 fibers was studied as a function of the pump energy employing the set up showed in Figure 4.1. The excited length was set to 1.92 cm for both fibers. Figure 4.9 illustrates the evolution of the emission spectrum for different pump energies. In both graphs, as the pump energy increases, characteristics of the ASE can be seen straightforward, namely a spectral narrowing and a blue-shift towards the peak of the emission cross section of the R6G dye. According to the plotted pump energies, it can be deducted that F16 fiber requires less excitation energy than F12 to reach the ASE threshold. This result could be expected as the dye concentration of F16 is higher than that of F12. However, to obtain more precise information about the ASE threshold of each of the samples the evolution of the FWHM of the emitted spectra and of the total output intensity were examined.

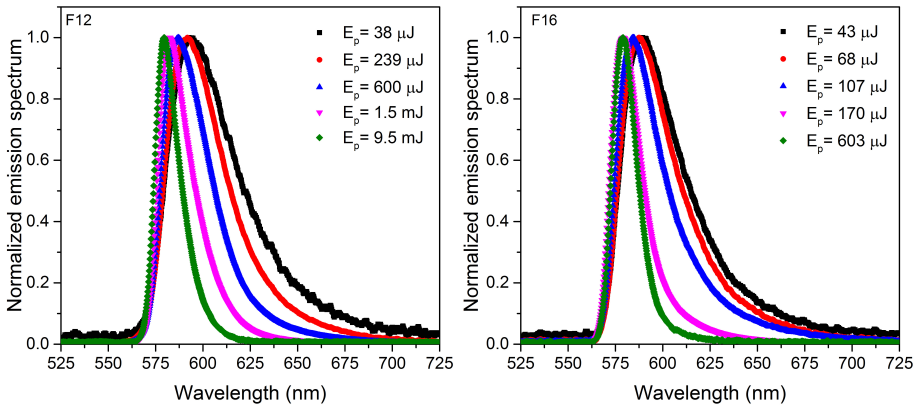

Figure 4.9: Evolution of the emission spectra of F12 (left) and F16 (right) for different excitation energies E_p. ASE characteristics such as spectral narrowing and blue-shift of the emission are observed when the pump energy is increased. ($z_e = 1.2$ mm).

As explained in Section 3.3.3, in materials with high gain, ASE may occur without the aid of any resonant cavities. This phenomenon happens above a threshold energy, which can be estimated employing both the FWHM of the emitted spectra or the output intensity curves. Figure 4.10 shows the progression of the FWHM of the emission of F12 and F16 as functions of the pump energy. It can be noted that the spectral narrowing occurs more rapidly for the F16 sample in comparison to F12, as it was expected. The ASE threshold values, calculated from the sigmoidal fitting curves (red lines in Figure 4.10), are 0.70 ± 0.05 mJ and 0.13 ± 0.06 mJ for F12 and F16 respectively. It can also be seen that the spectral narrowing reaches a saturation value due to gain-saturation effects, and the FWHM tends to become rather horizontal for high pump energies. Even if F16 sample reaches this saturation at lower pump energies than F12, for both fibers the FWHM narrows up to 15 nm, where saturation occurs. The absolute ASE narrowing is measured 29 nm for F12 and 27 nm for F16.

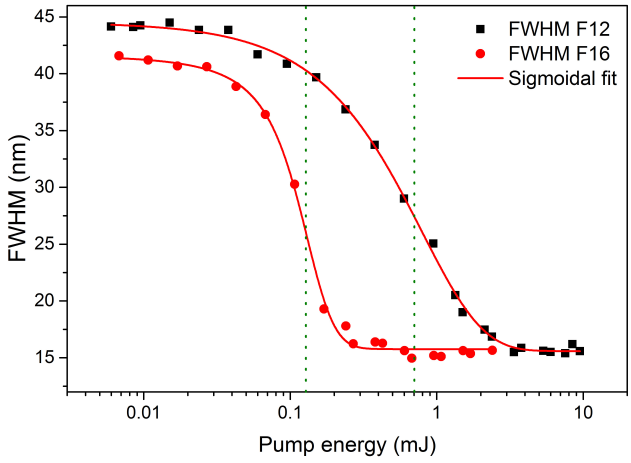

Figure 4.10: Progression of the spectral full width at half maximum for both F12 and F16 samples as functions of the pump energy. The solid red lines represent the sigmoidal fitting curves. The sigmoidal equation used is the following, $(A+B)/(1+e^{(C-x)/D})$, where parameter C defines the inflection point, which corresponds to the ASE threshold value.

Figure 4.11 illustrates the evolution of the total output intensities of F12 and F16 as functions of the pump energy. As can be seen, when the excitation energy exceeds the ASE threshold, the output intensity increases abruptly and it can be considered rather linearly dependent with the pump energy. From the pump power at which the linear curve cuts the x-axis, the ASE thresholds are determined. The values obtained are 0.81±0.08 mJ and 0.19±0.10 mJ for F12 and F16 respectively. These values slightly differ from those calculated from the FWHM curve, yet they are within the tolerance margin. F16 sample shows greater slope efficiency than F12 as can be seen from the slopes of the linear fittings.

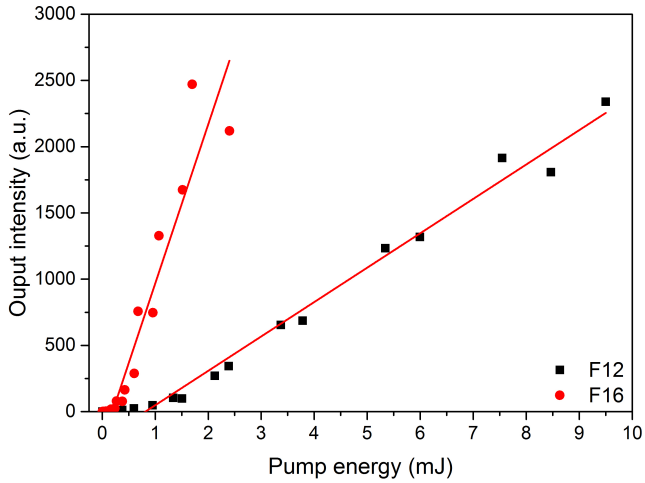

Figure 4.11: Evolution of the output intensities of F12 and F16 samples as functions of the pump energy. The solid red lines represent the linear fitting curves.

Finally, Figure 4.12 displays the pump power dependence of the average emission wavelength for both samples. This parameter is defined as $\lambda_{avg} = \int_{-\infty}^{\infty} \lambda P(\lambda) d\lambda / \int_{-\infty}^{\infty} P(\lambda) d\lambda$. As can be seen, the emission undergoes a spectral blue-shift under the presence of ASE. This effect may be explained as greater gains are obtained in the proximity of the peak of the emission cross section [53]. The initial λ_{avg} value of both samples is

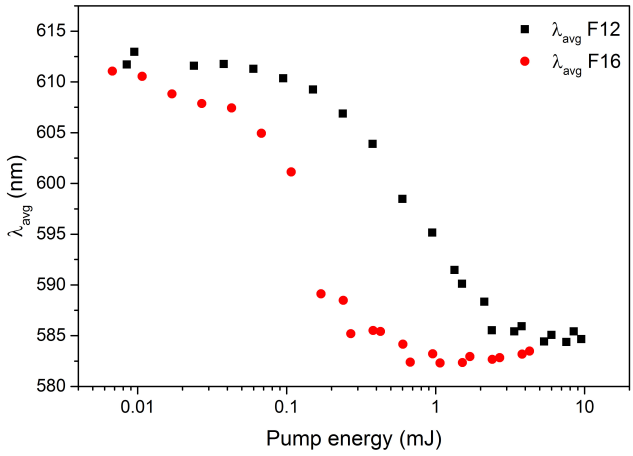

Figure 4.12: Progression of the average emission wavelength as a function of the pump energy for F12 and F16 fibers.

around 610 nm, and the final value if around 584 nm for F12 and 582 nm for F16. As it happened with the FWHM curve, the λ_{avg} curve also tends to saturate at a certain pump energy value. This saturation occurs again faster for the F16 sample, as its ASE threshold value is lower. The absolute blue-shifts calculated are 26 nm and 28 nm for F12 and F16 respectively. Table 4.2 summarizes all the aforementioned experimental values.

Table 4.2: Summary of the ASE characteristics of F12 and F16 fibers.

Fiber code	**ASE_{th} FWHM (mJ)**	**Spectral narrowing (nm)**	**ASE_{th} Intensity (mJ)**	**Blue-shift (nm)**
F12	0.70 ± 0.05	29	0.81 ± 0.08	26
F16	0.13 ± 0.06	27	0.19 ± 0.10	28

4.3.3 ASE features Vs z_e and study of the net gain

ASE can be observed not only varying the pump energy, but also as a function of the illuminated fiber length, z_e, when using an adequate pump irradiance. For this experiment the VSL method was employed, as shown in Figure 4.3.

Figure 4.13 shows an example of the evolution of the emission spectrum as a function of z_e. The data plotted correspond to F16 sample and five different illuminated lengths. As can be seen, as z_e increases, the emission narrows spectrally, and at the same time, it undergoes a blue-shift to the peak of emission. This two effects, as seen before, are signatures of ASE. A similar behavior is observed for the F12 sample.

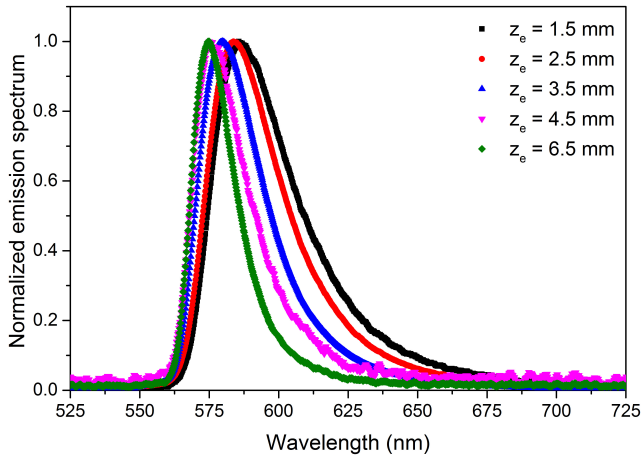

Figure 4.13: Evolution of the emission spectrum of F16 sample for different illuminated lengths, z_e. ASE characteristics such as spectral narrowing and blue-shift of the emission are observed when the z_e increases.

Continuing with this analysis, the dependency of the FWHM of the emitted spectra, the output intensity and the average emission wavelength with z_e were measured for F12 and F16 samples and for different

pump irradiances. It has to be noted that in the VSL technique the irradiance that impinges on the fiber at each step remains constant. Figures 4.14 and 4.15 illustrate the results obtained for F12 and F16 samples respectively. The data from F12 were obtained employing three different maximum excitation lengths, $z_{e,max}$ (0.64, 0.96 and 2.4 cm), and a constant pump energy of 12 mJ, what involves pump irradiances of 187, 125 and 50 mJ/cm^2 respectively. On the other hand, the data from F16 was measured for a $z_{e,max}$ of 1.92 cm and four different pump energies (0.6, 1, 1.6, and 2.5 mJ), obtaining excitation irradiances of 3.1, 5.2, 8.3, and 13 mJ/cm^2.

As can be seen in both figures, the spectral narrowing with z_e occurs faster when higher pump irradiances are employed. Therefore, the spectral width achieved for a certain z_e tends to be narrower for higher values of irradiance. However, due to gain saturation effects, the spectral width stops narrowing for long-enough values of z_e, and its curve becomes rather horizontal. This effect can clearly be seen when $z_{e,max}$ of 2.4 and 1.92 cm are used, for example in the case of 50 mJ/cm^2 in Figure 4.14 and in all cases in Figure 4.15. In the same way, the spectral blue-shift (see the evolution of the λ_{avg}) also occurs faster when higher pump irradiaces are employed, and it also saturates to a certain value for long-enough values of z_e. Note that the last data points of the output intensity curves of F16 fiber are also under the influence of gain saturation effects.

With the objective of corroborating the experimental trend with simulations, a comparison of the theoretical and experimental FWHM curves is illustrated in Figure 4.16 for F16 sample and three different pump irradiances (3.1, 5.2, and 13 mJ/cm^2). The simulations have been obtained from equations (3.6) and (3.7) when z_e is varied from 0 to $z_{e,max} = 2$ cm ($\gamma = 1.7$, $\beta = 0,07$, $\tau = 4.84$ ns, $\sigma^e = 1,46 \cdot 10^{-20}$ m^2,

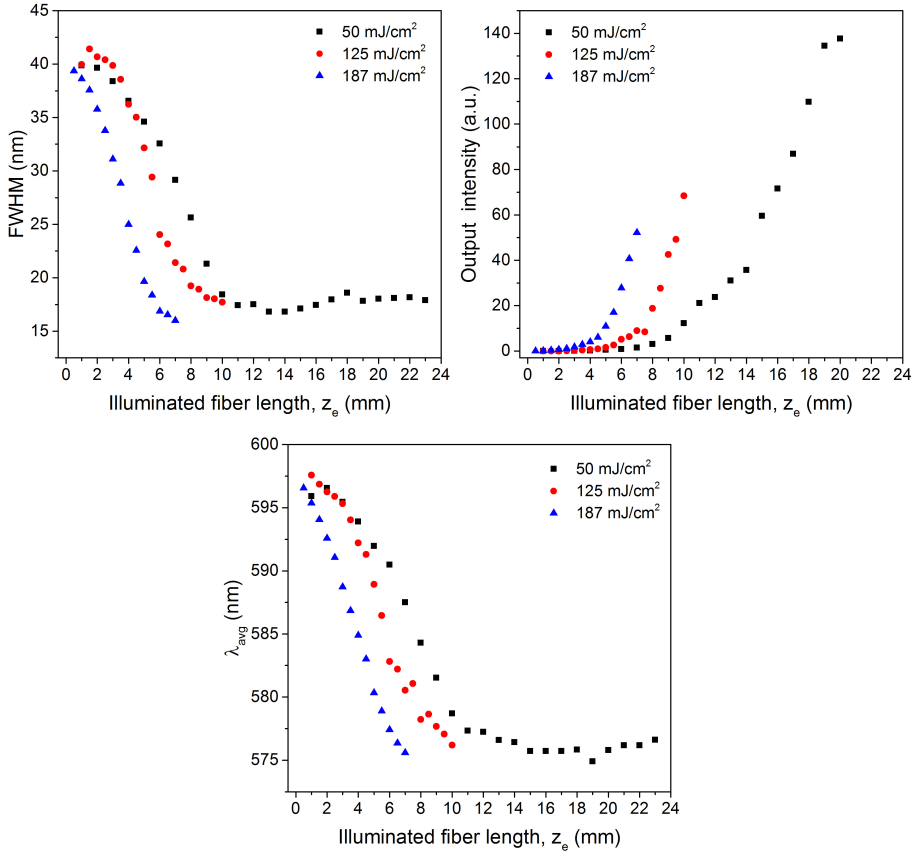

Figure 4.14: Evolution of the FWHM, the output intensity and the λ_{avg} of F12 sample as a function of z_e, for three pump irradiances of 50, 125 and 187 mJ/cm^2.

and $\sigma^a = 1.34 \cdot 10^{-21}$ m^2). As can be seen, the behavior is the same in both graphs, the FWHM curve narrows more rapidly when higher pump irradiances are used. Besides, both theoretical and experimental curves show that the spectral narrowing will never be smaller than a certain value due to saturation, e.g., 10 nm.

As seen in the previous section, the concentration of the dopant plays and important role in the ASE performing. In this case, the effect of the dopant concentration can also be observed in all the experimental re-

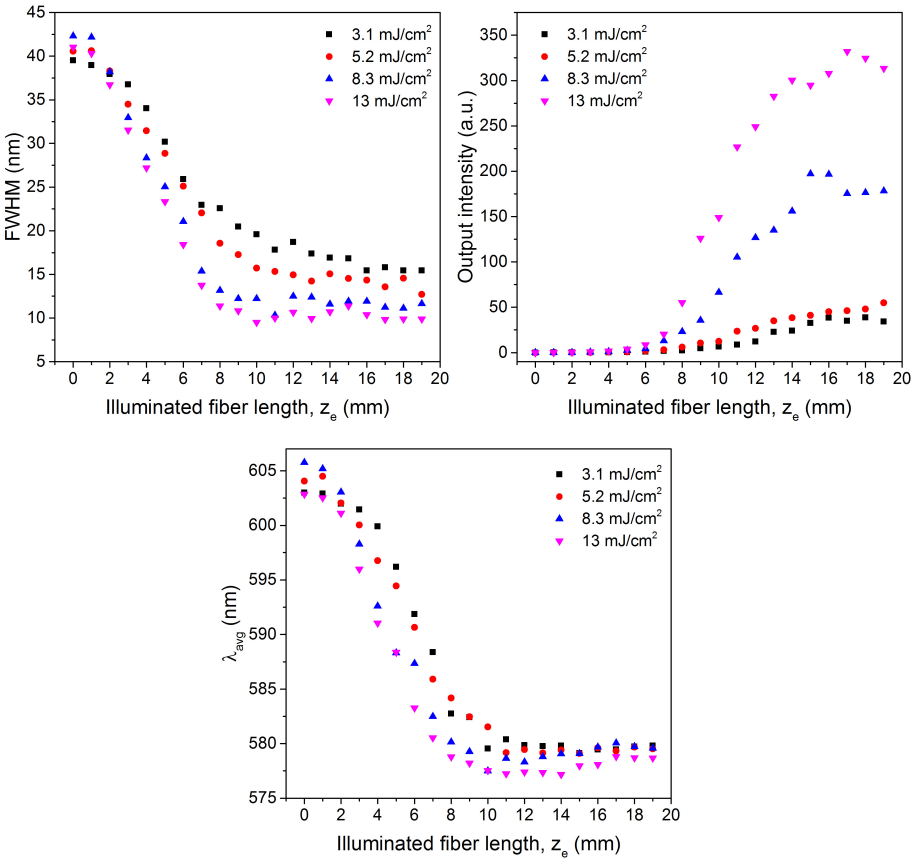

Figure 4.15: Evolution of the FWHM, the λ_{avg} and output intensity of F16 sample as a function of z_e, for four pump irradiances of 3.1, 5.2, 8.3, and 13 mJ/cm^2.

sults. As an example, for a certain value of z_e, F16 fiber experiments approximately the same spectral narrowing than F12 but for a pump irradiance much smaller. This effect is even better observed from the results obtained from the calculations of the optical gains. The optical gain coefficients were calculated by fitting the output intensities to equation (3.11) for each of the wavelengths of interest. The relative error of the obtained values was around 2.5%. An example of this method is shown in Figure 4.17 for the F16 sample and a λ of 570 nm. As can be seen, when

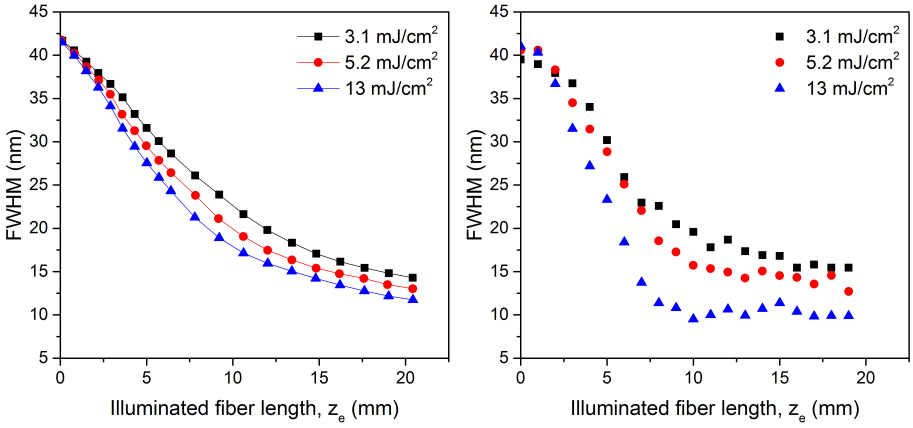

Figure 4.16: Theoretical (left) and experimental (right) evolution of the FWHM for the F16 sample and three pump irradiances (3.1, 5.2, and 13 mJ/cm^2).

the excitation length grows above a certain point, the output intensity starts saturating. This phenomenon is known as *gain saturation effect*. For the calculation of the net gain only the experimental points before saturation are taken into account, as the red fitting curve illustrates.

Figure 4.18 shows the spectral gains obtained for F12 (left) and F16 (right) for a region of interest from 550 to 590 nm. As can be seen, at all wavelengths and for both fibers, greater gains are achieved with greater excitation irradiances. The maximum gain takes place at a wavelength λ that lies in the range between 565 and 570 nm. In spite of the much greater pump irradiances employed with the F12 fibre, the gains obtained with both fibres are similar, reaching a maximum value of around 13 cm^{-1} for the case of highest pump irradiance. More precisely, for this specific case, 20 times less pump irradiance is needed for F16 fiber than for F12 fiber to get approximately the same optical gain. This fact confirms the strong influence of the dopant concentration on the ASE performance of these R6G doped GI PMMA fibers. The values of the gains obtained in this experiment are comparable to those reported

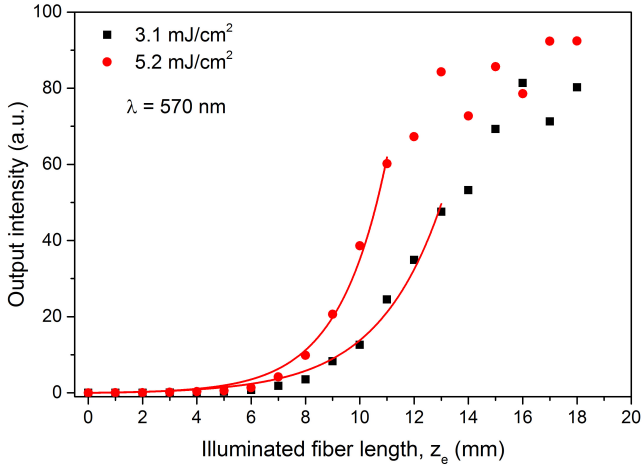

Figure 4.17: Example of the calculation of the optical gain for F16 with two different irradiances and a wavelength of interest of 570 nm. The solid red lines represent the fitting curves to equation (3.11) carried out in the range of 0 cm and 1.1 or 1.3 cm to avoid saturation effects.

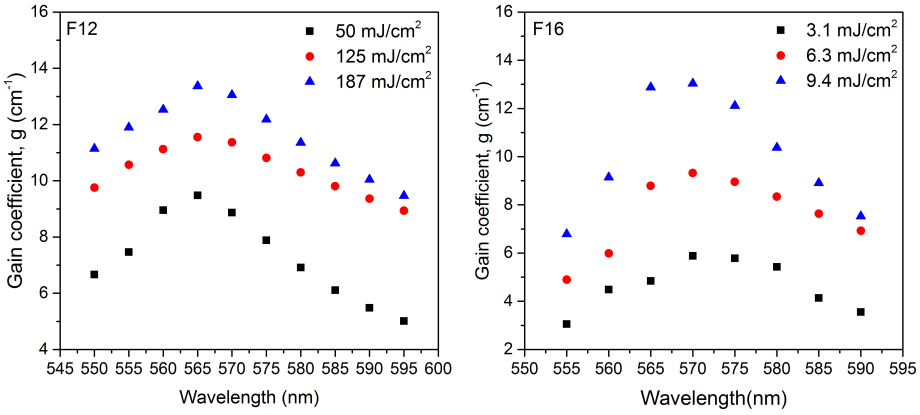

Figure 4.18: Calculated spectral net gains for F12 and F16 fibers for different pump irradiances. The relative error of the obtained gain values is $\sim 2.5\%$.

by Persano et al. in electrospun R6G doped PMMA nanofibres, whith values of 8 cm^{-1} at 600 nm [92].

On the other hand, with the aim of comparison between gain and

losses, the attenuation coefficients of F16 were calculated following the method shown in Section 4.2. As it was expected for gain regime, the gain coefficients are much greater than the attenuation coefficients for all the wavelength analyzed. As an example, at $\lambda = 570$ nm $g \approx 13$ cm^{-1} ($I = 9.4$ mJ/cm^2), and the attenuation coefficient at that same λ is $\alpha \approx 0.16$ cm^{-1}. Figure 4.19 gathers the attenuation coefficients as function of wavelength corresponding to F16 sample.

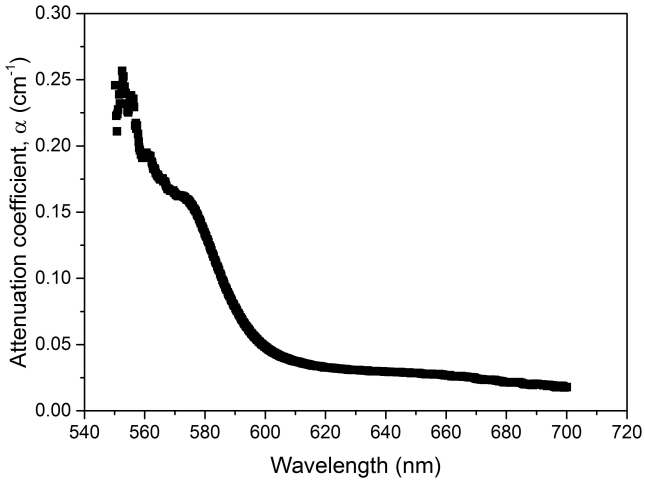

Figure 4.19: Attenuation coefficients of F16 sample obtained from the SIT. The relative error of the obtained values is $\sim 3\%$.

As a final study, the variation of the local gain along the fiber length was analyzed for the F16 fiber. The calculations were performed employing the rate equations (3.6) and (3.7), and three different values of $z_{e,max}$ (0.64 cm, 2.4 cm, and 3 cm), but maintaining a constant pump irradiance of $I_p = 8$ mJ/cm^2. Figure 4.20 illustrates the evolution of the net gain at different positions z along the fiber, starting from the edge of the excited fiber length and finishing at the fiber end, where the light detection occurs. As can be seen, when $z_{e,max}$ is 2.4 cm and 3 cm there is a zone of rather constant positive gain from a certain minimum value of z to nearly $z_{e,max}$. As z approaches $z_{e,max}$, the start of gain satura-

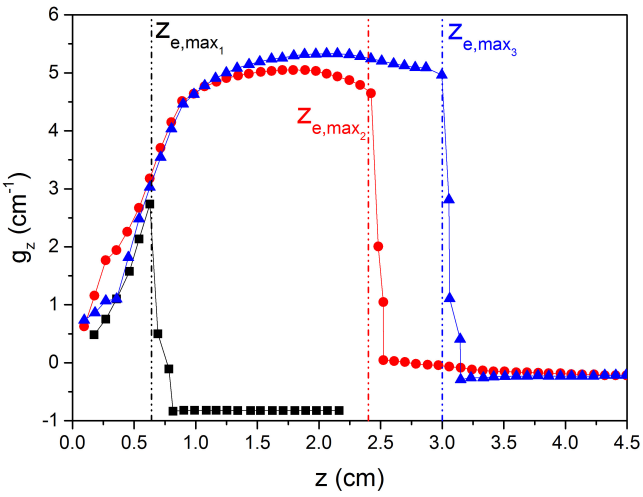

Figure 4.20: Theoretical calculation of the evolution of the local gain at different positions z on the fiber for three different $z_{e,max}$ (z_{e,max_1} = 0.64 cm, z_{e,max_2} = 2.4 cm, and z_{e,max_3} = 3 cm), and a constant pump irradiance of $I_p = 8$ mJ/cm^2. ($g_z = dlogE)/dz$).

tion can be observed, since the values of gain begin to decrease. Once $z > z_{e,max}$ there is a very rapid transition from positive to negative gains, and there is another rather constant zone of negative gain. This zone corresponds to the contribution of the non-excited length z_{ne}, as in the measurements the light that has traveled all the fiber length $z_e + z_{ne}$ is collected, thus crossing zones of positive and negative gain. The negative gain in z_{ne} is due to fiber losses, and its absolute value tends to be equal to the absorption coefficient α of the fiber. If the absolute values of gain are considered, it can be seen that they are much smaller in z_{ne} than in z_e, and thus, the contribution of the non-excited length to the output energy is relatively negligible. As seen from Figure 4.19 the value of α was measured to be around 0.16 cm^{-1} at 570 nm for the F16 sample, which is in agreement with the values shown in Figure 4.20, and confirms that the losses in z_{ne} are much smaller that the gain in z_e. Therefore, the output of the fiber can be estimated from the behavior of light in the

illuminated length z_e. From these results, it can be concluded than when $z_{e,max}$ is large, the gain becomes rather constant along a large enough length to be able to assume a constant gain inside z_e, as it was raised in equation (3.11). For the smallest values of z, the gain is variable, so it is convenient to use large enough values of z_e to obtain a constant gain.

4.3.4 Polarization effects on ASE and on the net gain

The effects of of pumping the doped POFs with vertical and horizontal polarizations is studied in this section, both as function of the pump energy and as function of the illuminated fiber length employing the VSL method.

The first analysis was carried out for the F12 sample with an excited fiber length of 1.92 cm, and employing the set up from Figure 4.1. Figure 4.21 shows the evolution of the FWHM curve (left) and of the output intensity (right) for both pump polarizations analyzed, horizontal and vertical. As can be seen, the spectral narrowing and the abrupt increase of the output intensity occurs at lower pump energies for the vertical polarization. This involves a lower ASE threshold when the sample is excited with a perpendicular polarization to the fiber symmetry axis. Besides, from the slopes of the linear fittings of the output intensity, it can be seen that the slope efficiency is greater for the vertical polarization excitation. The main reason for these phenomena could underlie in the orientation of the excited dipole moments ($\overrightarrow{p}$). For the vertical polarization, the majority of the excited dipole moments are aligned perpendicularly to the fiber axis, so that their emission lobes are mainly oriented towards the fiber symmetry axis, helping the waveguiding of the emitted light through the fiber core [110]. A schematic representation of this assumption is illustrated in Figure 4.22. The ASE thresholds values

calculated with the two methods and the spectral narrowing are gathered in Table 4.3. As can be seen, the ASE thresholds are around 2 times smaller when using vertical polarization.

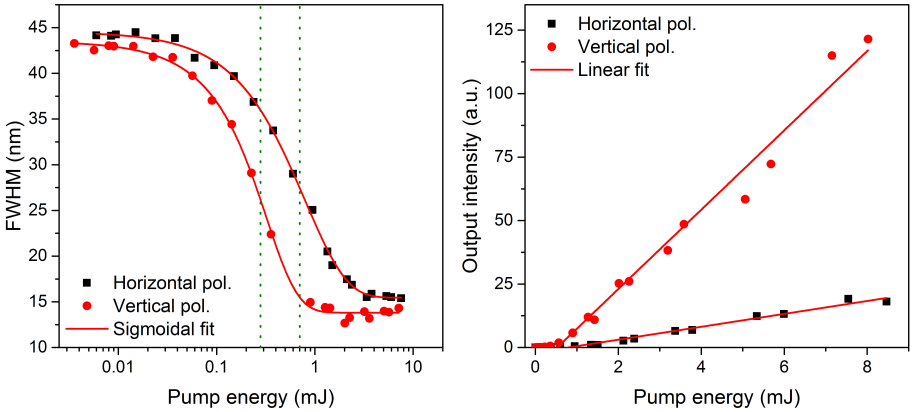

Figure 4.21: Evolution of the FWHM of the emitted spectra (left) and of the output intensity (right) of the F12 sample for horizontal and vertical polarizations. The solid red lines represent the fitting curves.

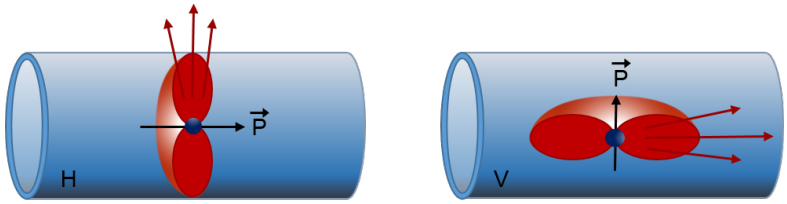

Figure 4.22: Illustration of the radiation patterns for a dipole parallel to the fiber symmetry axis (left) and for a dipole perpendicular to the fiber symmetry axis (right), corresponding to the horizontal and vertical pump polarizations respectively. $\overrightarrow{p}$ represents the dipole moment [110].

Figure 4.23 shows the progression of the λ_{avg} for the two pump polarizations, which represents the blue-shift the emission spectrum undergoes when ASE occurs. As can be seen, the blue-shift is practically the same for both pump polarizations although the spectral displacement occurs at lower pump energies for the vertical polarization. The absolute values of the spectral blue-shift are gathered in Table 4.3.

Table 4.3: Summary of the ASE characteristics of F12 sample for two pump polarizations.

Polarization	**ASE_{th} FWHM (mJ)**	**Spectral narrowing (nm)**	**ASE_{th} Intensity (mJ)**	**Blue-shift (nm)**
Horizontal	0.70 ± 0.05	29	0.81 ± 0.08	26
Vertical	0.28 ± 0.09	29	0.48 ± 0.12	27

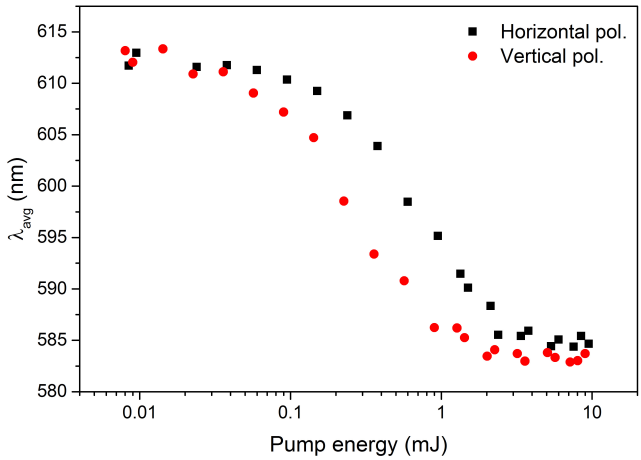

Figure 4.23: Progression of the average emission wavelength as a function of the pump energy for the F12 fiber and horizontal and vertical pump polarizations.

As a second analysis, the effects the pump polarization may have on the ASE and gain performance was studied as a function of the illuminated fiber length. The sample under test was F12 fiber with a $z_{e,max}$ of 2.4 and three different pump irradiances, namely 23, 14.5, and 10.5 mJ/cm^2, each of them studied for horizontal and vertical polarizations.

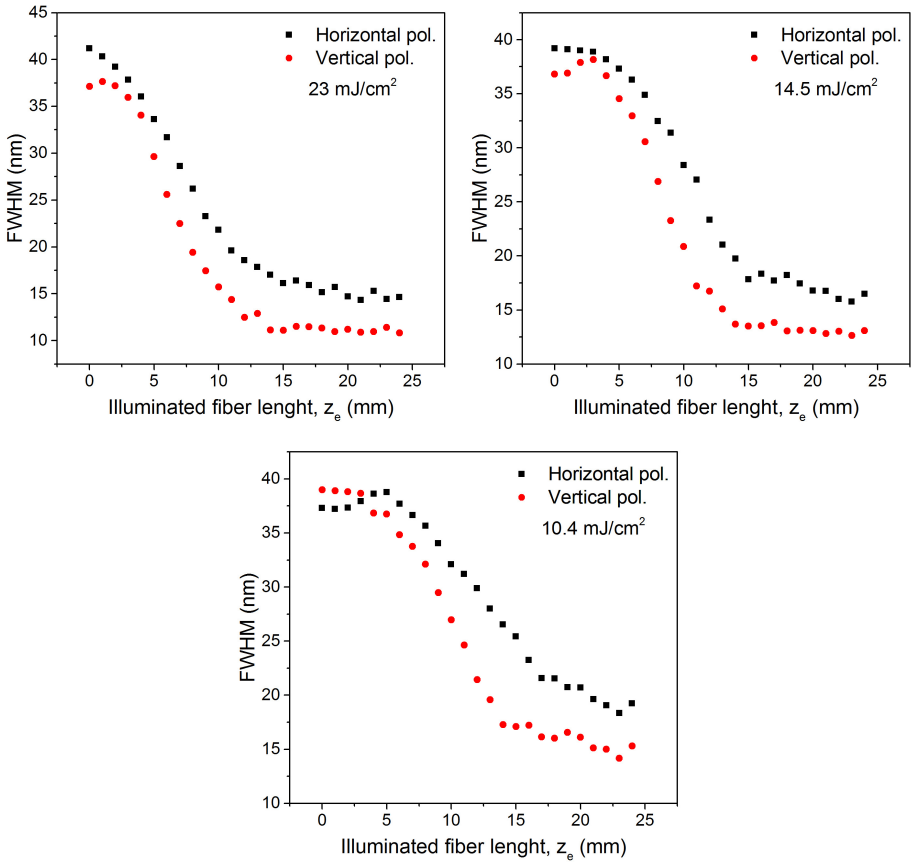

Figure 4.24: Evolution of the FWHM curve of F12 samples as a function of z_e for two different polarizations and three pump irradiances, 23, 14.5, and 10.5 mJ/cm^2.

The FWHM curves are illustrated in Figure 4.24. As can be seen, in all cases the spectral narrowing occurs at shorter illuminated lengths for the vertical polarization. Besides, it can also be observed that ASE occurs more rapid with higher pump irradiances. These results agrees with those shown in the previous section. The spectral blue-shift of the λ_{avg} was also observed at shorter z_e for the vertical polarization and for higher pump irradiances.

Finally, Figure 4.25 illustrates the output intensity curves employed for the gain coefficient calculation. It corresponds to the pump irradiance of 23 mJ/cm^2 and a emission wavelength of 575 nm. From the fittings of the experimental data to equation (3.11), gain coefficients of 3.9 ± 0.2 cm^{-1} and 4.8 ± 0.2 cm^{-1} were calculated for horizontal and vertical polarizations respectively. As it was expected, about 1.23 times grater gain is obtained for the vertical polarization under the same experimental conditions.

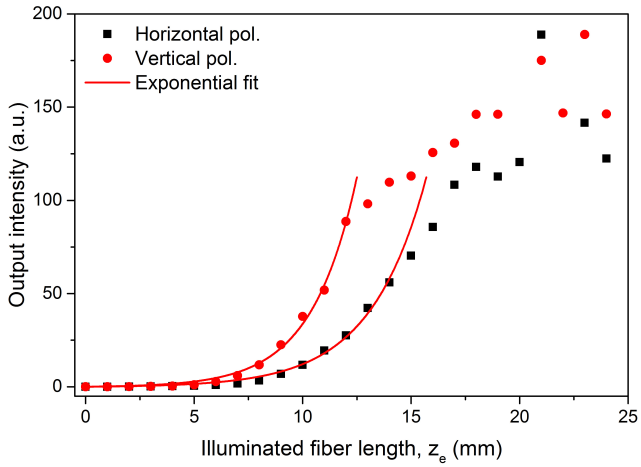

Figure 4.25: Output intensities of F12 sample as a function of z_e for a pump irradiance of 23 mJ/cm^2, a emission wavelength of 575 nm, and horizontal and vertical polarizations. The solid red lines represent the fittings of the data points to equation (3.11).

4.4 Result 2: Cladded and uncladded R6G doped thermoset SI POFs: ASE, gain and two-photon fluorescence analysis

The emission properties of R6G doped SI cladded and uncladded thermoset fibers were studied in a transversal excitation configuration. The measurements include an analysis of the ASE performance and a study of the optical gains by using the VSL method. The pump polarization influence was reported for both analysis. Besides, the evolution of the emission spectra as a function of the propagation distance was also reported for both one-photon absorption and two-photon absorption. Comparisons of the results of the cladded fiber with those of the uncladded one are presented and discussed.

4.4.1 Samples

The samples analyzed are cladded and uncladded SI thermoset POFs doped with R6G in their cores with a concentration of 300 ppm. The dye radial distribution and the refractive index are uniform all along the core. The samples were obtained from a collaboration with the fiber manufacturing company Intellisiv Ltd. (Gadera, Israel). They were fabricated by a photopolymerization process via UV-curing, where the polymerization and fiber fabrication occurs in one unique step. This fabrication method does not require solvents or polymer melting. More information about the fiber fabrication method can be found in [111, 112]. The diameter of the uncladded fiber is 870 μm, whereas the total diameter of the cladded fiber is 740 μm including a cladding of 25 μm. The core refractive index is 1.54 in both cases. Figure 4.26 shows two microscope images of the transversal sections of the samples. The main characteristics of both

fibers are gathered in Table 4.4.

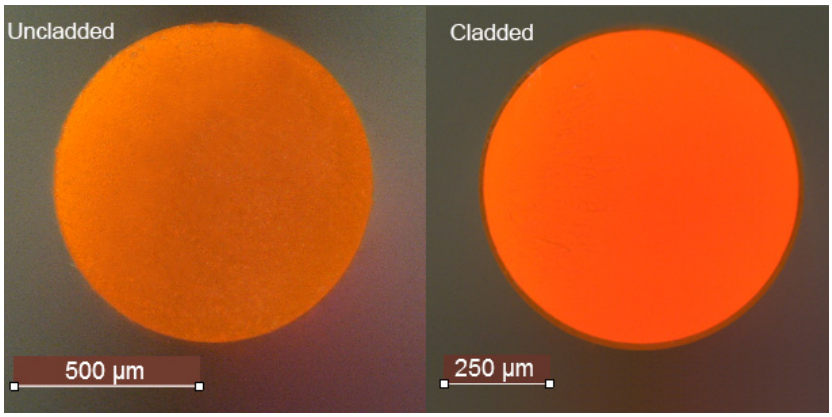

Figure 4.26: Microscope images of the transversal sections of the two thermoset POFs, the uncladded fiber on the left, and the cladded fiber on the right.

Table 4.4: Summary of the characteristics of the R6G doped thermoset SI POFs.

Fiber	**Type**	**Host**	**Conc. (ppm)**	**Core ⌀ (μm)**	**Total ⌀ (μm)**
Uncladded	SI	Thermoset polymer	300	870	870
Cladded	SI	Thermoset polymer	300	715	740

The absorption and fluorescence spectra of the cladded sample are presented in Figure 4.27. There is a strong absorption band corresponding to the dominant transition from the ground state S_0 to the first excited singlet state S_1 located approximately at the spectral region between 490 nm and 560 mm. As happened for the R6G PMMA GI samples in the previous section, the absorption band shows a flattened shape in this wavelength range, which can be explained from the contributions of dye aggregates formed at the high dopant concentrations that tend to broaden the absorption band. The normalized fluorescence spectrum corresponds to the transition from S_1 to S_0, and its is located at around

617 nm. The typical overlap between the absorption and fluorescence spectra of R6G can also be observed.

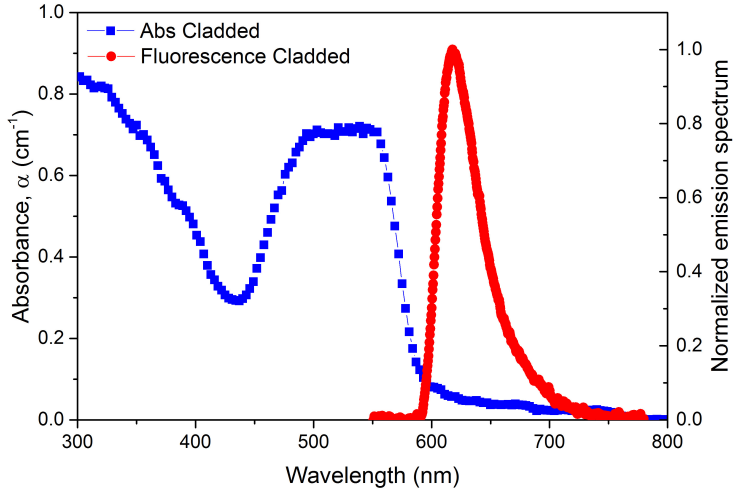

Figure 4.27: Spectral absorption coefficients (α) and normalized fluorescence spectrum corresponding to the cladded thermoset sample. ($z_e = 1.2$ mm).

4.4.2 ASE features Vs pump energy

The ASE performance of the cladded and uncladded thermoset POFs has been studied as a function of the pump energy using the set-up from Figure 4.1. The excited fiber length was 0.96 cm.

Figure 4.28 illustrates the progression of the emission spectrum as different pump energies are employed. The data correspond to the cladded sample. As can be seen, with low pump energies fluorescence dominates the emission, but as the pump energy increases, ASE occurs, i.e., a narrowing and a blue-shift of the emission spectra. These two signatures of ASE are also represented in Figure 4.29 as functions of the excitation energy for both fiber samples. It can be noted that the spectral narrowing

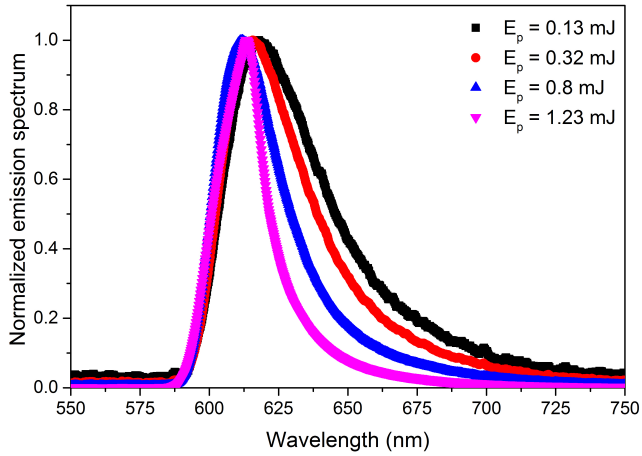

Figure 4.28: Evolution of the emission spectrum of the cladded thermoset POF for different excitation energies. ASE characteristics such as spectral narrowing and blue-shift of the emission are observed when the pump energy is increased.

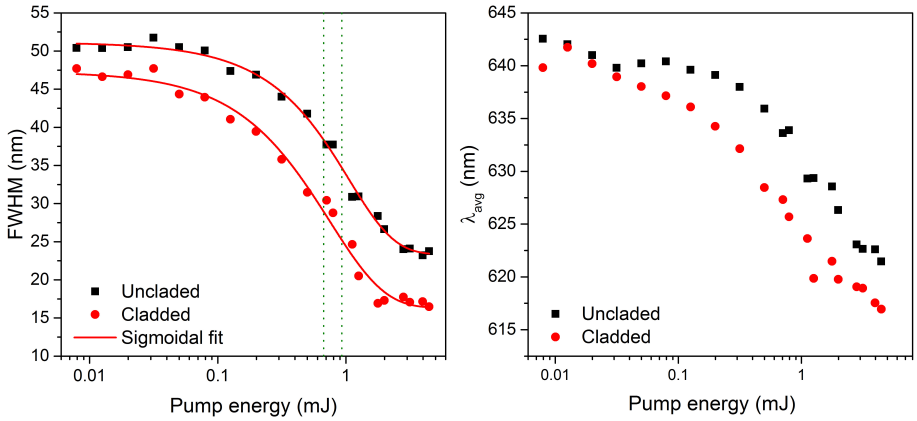

Figure 4.29: Evolution of the FWHM (left) and the λ_{avg} (right) of the emission as functions of the pump energy for the uncladded and cladded thermoset POFs. The red curves represent the sigmoidal fittings to FWHM data.

occurs faster for the cladded sample than for the uncladded one, what suggests a lower ASE threshold energy for the cladded fiber. From the fittings of sigmoidal curves to the FWHM data, the ASE thresholds were

calculated, yielding values of 0.93 ± 0.06 mJ and 0.67 ± 0.08 mJ for the uncladded and the cladded fibers respectively. In other words, approximately 30% less energy is needed in the cladded sample to ASE to occur. The FWHM of the cladded sample narrows up to 16 nm, whereas the uncladded fiber narrows up to 23 nm. The absolute ASE narrowing is measured 27 and 29 nm for the uncladded and cladded fibers. Table 4.5 summarizes the main ASE characteristics of both fibers.

Table 4.5: Summary of the ASE characteristics of the uncladded and cladded thermoset POFs.

Fiber	**ASE_{th} FWHM (mJ)**	**Spectral narrowing (nm)**	**Blue-shift (nm)**
Uncladded	0.93 ± 0.06	27	19
Cladded	0.67 ± 0.08	29	24

The main reason for obatining a best perfomance with the cladded sample may be due to the fact that the use of a cladding protects the core from, for example, scratches, fingerprints and environmental conditions that can cause the light to leak out from the fiber, while it maintains the total internal light guidance through the core. In uncladded fibers, total internal reflection also occurs, but the loss probability along the fiber surface increases because the imperfections and roughness are more noticeable and critical. This same behavior was demonstrated in the work carried out by Bikandi et al. [113], where they measured that the intensity emitted from a cladded doped POF was in average three times greater than the emitted by an uncladded sample. Besides, they demonstrated that the decay of the intensity with distance was clearly lower for the cladded fiber, what corroborated the existence of more loss sources in the core-air interface than in the core-clad interface

4.4.3 Study of the net gain

The optical gain of these thermoset POFs was studied employing the VSL set-up shown in Figure 4.3. The maximum illuminated fiber length was 0.96 cm and the pump energy was set 3 mJ, what involves a pump irradiance of 31 mJ/cm^2.

The optical gain coefficients were calculated by the fittings of equation (3.11) to the output intensities for each of the wavelengths of interest. The relative error of the obtained gain values was around 5%. An example of this calculation is shown in Figure 4.30 for the uncladded sample and two emission wavelengths (605 and 620 nm). As can be seen, the intensity curve rises more steeply for $\lambda = 605$ nm, what indicates that a higher gain will be obtained for these wavelength. Figure 4.31 shows the spectral gains calculated for both the uncladded and the cladded samples and a wavelength-range of interest between 580 and 620 nm. As it illustrates, greater gains are achieved for the cladded fiber under the same measuring conditions. As expected, this result agrees with those obtained from the analysis of the ASE performance, where it was seen that the cladded fiber shows a more efficient ASE output due to the protection the cladding provides against possible loss sources.

With the aim of comparing these results with those obtained for the GI R6G doped PMMA POFs (Section 4.3.3), Figure 4.32 has been plotted. This figure represents the optical gains achieved for the F16 R6G doped PMMA fiber, and for the cladded R6G doped thermoset POF. As a reminder, the first is a GI fiber with a core diameter of 0.710 mm doped with R6G in a concentration of 16 ppm in average, and with a PMMA host. The later, is a SI fiber with a core diameter of 0.715 mm doped with R6G in a concentration of 300 ppm, and hosted in a thermoset

polymer. A summary of the characteristics of these fibers, and the pump irradiance used at each measurement is shown in Table 4.6.

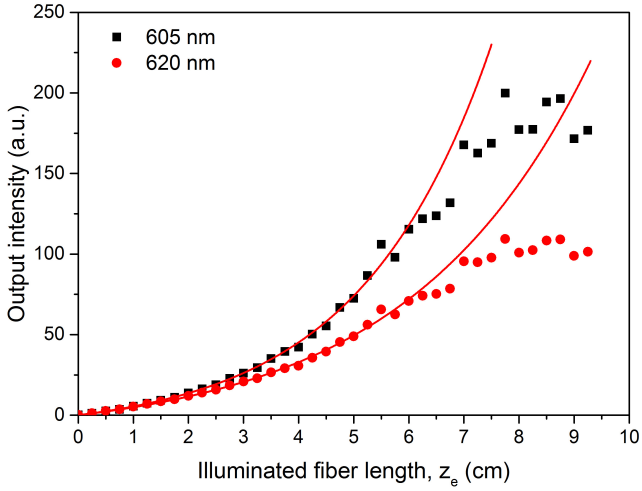

Figure 4.30: Example of the calculation of the optical gain for the uncladded thermoset and two emission wavelengths (605 and 620 nm). The pump irradiance employed is 31 mJ/cm^2. The solid red lines represent the fitting curves of equation (3.11).

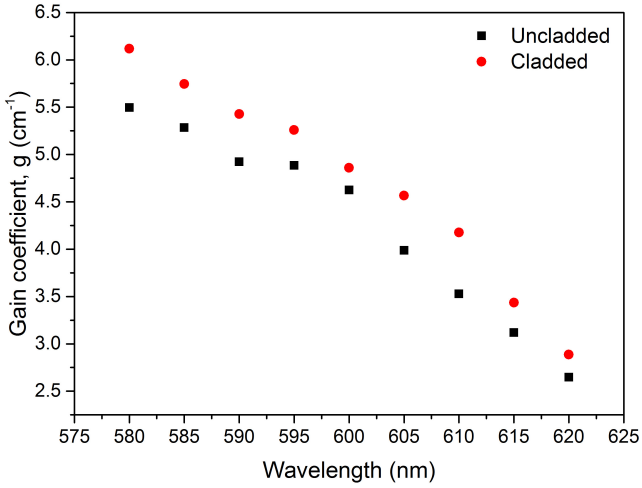

Figure 4.31: Calculated spectral gains for the uncladded and cladded thermoset fibers for a wavelength-range of interest between 580 and 620 nm. The relative error of the obtained gain values is $\sim 5\%$.

Table 4.6: Summary of the characteristics of the PMMA and thermoset samples, and the pump irradiance employed at each of the measurements.

Sample	Host	Type	Dopant	Conc. (ppm)	Core ⌀ (mm)	Irradiance (mJ/cm^2)
F16	PMMA	GI	R6G	16	0.710	6.3
Cladded	Thermoset polymer	SI	R6G	300	0.715	31

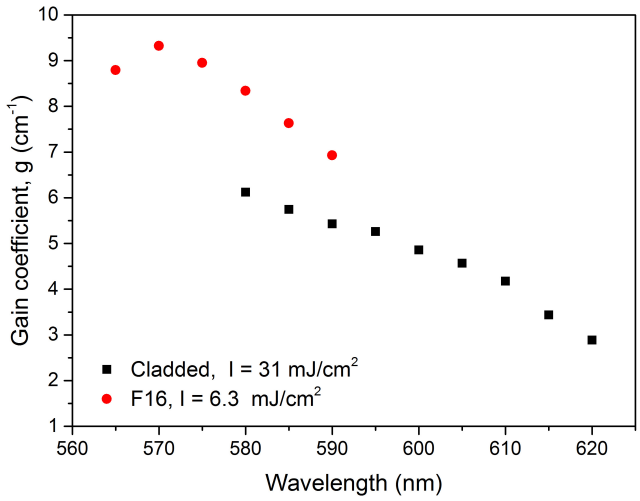

Figure 4.32: Comparison of the spectral gains for F16 PMMA sample and the cladded thermoset sample.

In spite of the greater dopant concentration and the higher pump irradiance employed with the thermoset sample, the optical gains are still higher for the PMMA sample. This effect can be explained by two main reasons. On the one hand, as seen in Section 3.4, when the power density and the dopant concentration are greater towards the fiber symmetry axis (GI fiber), the interaction between dopant and light increases ($\gamma > 1$). In other words, light interacts more efficiently with the dye molecules in GI dopant distributions, what leads to higher gain coeffcients (see in equation (3.12) that the gain is proportional to γ) [85, 114]. On the other

hand, the lower gain values obtained for the thermoset fiber can also be explained by the very high dopant concentration employed in this sample. With such a strong dye concentration the R6G molecules may not have been completely dissolved and the dye molecules may have formed aggregates. The aggregation of rhodamine has serious disadvantages in their application in amplification media. The molecular nature of the dye is strongly affected, and they exhibit changes in their absorption band. As a result there is a decrease of the fluorescence quantum efficiency and of the stimulated emission cross section of the dye [115, 116, 117].

4.4.4 Polarization effects on ASE and on the net gain

Figures 4.33 shows the evolution of the FWHM and of the λ_{avg} of the emitted spectra as functions of the pump energy for the uncladded (top) and cladded (bottom) samples respectively and horizontal and vertical polarizations (z_e = 0.96 cm) As can be seen, in both fibers the spectral narrowing and the blue-shift occurs at lower pump energies when the sample is excited with a perpendicular polarization to the fiber axis (vertical polarization). This is the same effect measured for R6G doped PMMA fibers (see Section 4.3.4), where it was seen that ASE performs more efficiently for vertical polarization excitation, obtaining lower ASE threshold values. The ASE threshold and the blue-shift values are gathered in Table 4.7.

Besides, the effects the pump polarization may have on the gain performance were also studied employing the VSL method, for a maximum illuminated fiber length of 0.96 cm and a pump irradiance of 31 mJ/cm^2. The optical polarization dependent gain curves for a wavelength range from 580 to 620 nm are shown in Figure 4.34. It can be observed that the gain coefficients are greater for the vertical polarization than for the

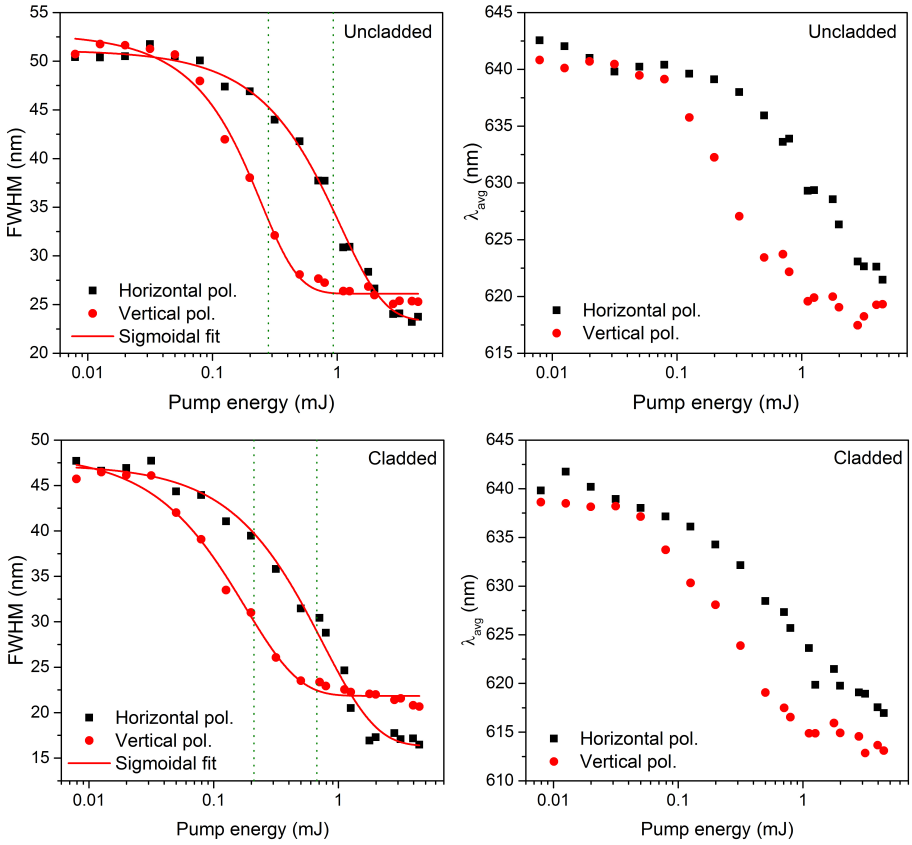

Figure 4.33: Evolution of the FWHM (left) and the λ_{avg} (right) as functions of the pump energy for the uncladded (top) and the cladded (bottom) samples and horizontal and vertical polarization. The red curves represent the sigmoidal fittings to FWHM data.

horizontal one in all the analyzed wavelengths, obtaining an improvement of around 1.5 cm^{-1} at each studied wavelength. In other words, about 1.28 times greater gain is obtained for the vertical polarization under the same measuring conditions. This result agrees with that reported in Section 4.3.4 for the PMMA GI sample, what indicates that the reason of the increase in gain with the pump polarization is provided by the fiber cavity itself. From this graph it can also been observed that greater gain values are obtained for the uncladded sample with vertical

Table 4.7: Summary of the ASE characteristics of the uncladded and cladded thermoset POFs for horizontal and vertical polarizations.

Fiber	Polarization	$\mathbf{ASE_{th}}$ FWHM (mJ)	Blue-shift (nm)
Uncladded	H	0.93 ± 0.06	19
	V	0.28 ± 0.09	22
Cladded	H	0.67 ± 0.08	24
	V	0.21 ± 0.06	25

polarization, than for the cladded sample with horizontal polarization. This result demonstrates that the pump polarization has a greater effect on the optical gain than the effect of having a cladding. In any case, the best ASE performance is obtained employing a cladded sample and a vertical polarization configuration.

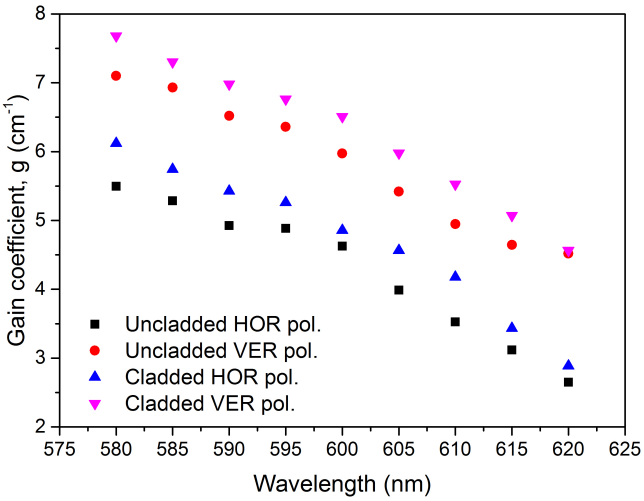

Figure 4.34: Comparison of the optical gain curves of the uncladded and cladded samples for horizontal and vertical polarizations. The pump irradiance employed is 31 mJ/cm^2 and the wavelength region of interest is from 580 to 620 nm. The relative of the optical gain values is $\sim 5\%$.

4.4.5 Two-photon emission

For studying the emission from the TPA fluorescence the set-up shown in Figure 4.5 was used. The fibers were pumped at at 1040 nm and an irradiance of 9120 W/cm^2, which was high enough for detecting emission. The OPA emission was measured with a pump irradiance of 2 W/cm^2 and a excitation wavelength of 520 nm.

The OPA and TPA emission spectra of the cladded fiber are plotted in Figure 4.35 for a $z_{ne} = 48$ mm. As can be observed, the TPA spectrum is shifted towards higher wavelengths by 11 nm in comparison with that obtained with the OPA. The same effect is observed in the uncladded fiber. A possible explanation may be related to the excitation configuration employed. In the TPA set-up, a very small point excitation is used, obtained by focusing the laser beam with a convergence lens. In this configuration of point excitation, the emitted rays would travel longer distances along the fiber and, therefore, endure greater red shifts compared to the OPA configuration, where a bigger region is excited and more parallel rays would be emitted [60]. A schematic representation of this effect is illustrated in Figure 4.36 [23].

To deepen on the study of the OPA and TPA properties, an analysis of the effects of varying the propagation distance was carried out employing a motor driven linear stage and varying z_{ne} from 38 to 150 mm. The evolution of the FWHM and of the λ_{avg} of the emitted spectra as functions of the propagation distance z_{ne} is shown in Figure 4.37 for the uncladded and the cladded samples. Focusing on the spectral widths, there are only slight variations with the propagation distance. This means that neither the OPA nor the TPA emission spectra undergo a representative change on its shape for the analyzed propagation distances. On the other hand, when the excitation point is moved further from the detector the average

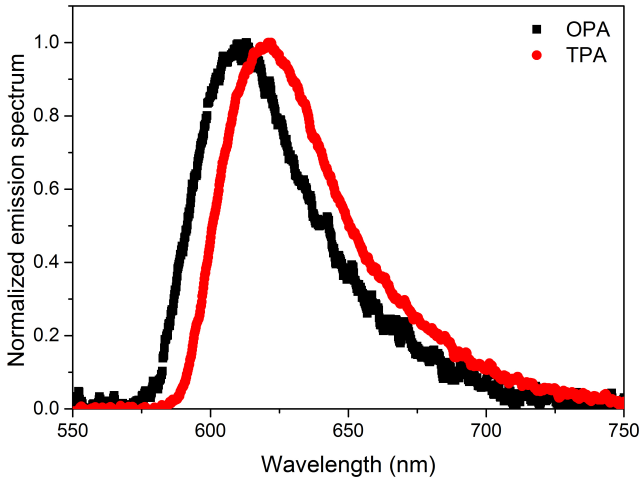

Figure 4.35: OPA and TPA emission spectra of the cladded thermoset POF for a constant light propagation distance of $z_{ne} = 48$ mm an a pump irradiance of 2 W/cm^2 ($\lambda = 520$ nm) and 9120 W/cm^2 ($\lambda = 1040$ nm) for the OPA and TPA respectively.

emission wavelength is shifted towards higher wavelengths, due to reabsorption and reemission effects. The TPA curves are clearly red-shifted by approximately 11 nm from the OPA curves for both samples, as it was shown in Figure 4.35. In spite of this red-shift, both fibers undergo similar slopes for each of the configurations, these being around 1.6 nm/cm for the uncladded fiber and around 2 nm/cm for the cladded sample. This kind of analysis can be useful for the design of displacement sensors based on doped POFs. The values of the average FWHM and the slopes of the λ_{avg} with respect to z_{ne} are gathered in Table 4.8.

4.5 Conclusions

In this chapter various R6G doped POFs have been studied with the aim of investigating their emission properties for possible applications in

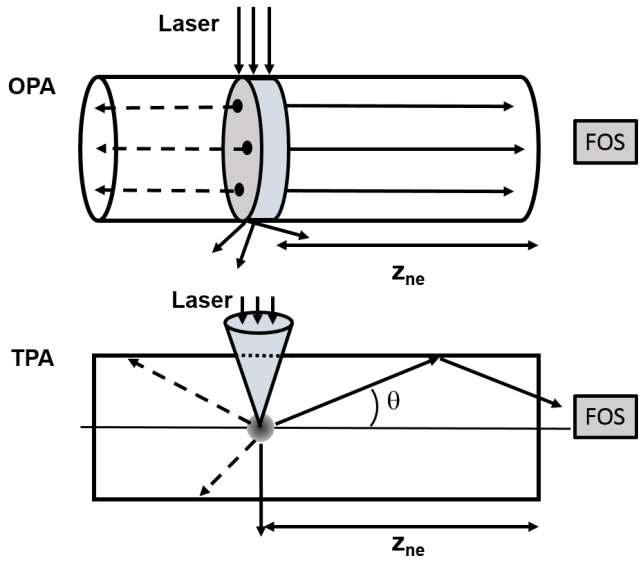

Figure 4.36: Representative illustration of the distance traveled by the rays in two excitation configuration. Excitation of a wide POF region (top). Point source excitation where the rays may travel longer distances, as in the case of TPA set-up (bottom) [23]. FOS: fiber-optic spectrometer.

Table 4.8: Values of the average FWHM and the λ_{avg} slopes with respect to z_{ne} for OPA and TPA and both uncladded and cladded thermoset samples.

Configuration		**Average FWHM (nm)**	**λ_{avg} slope (nm/cm)**
OPA	Uncladded	50 ± 1	1.66 ± 0.07
	Cladded	51 ± 1	1.94 ± 0.05
TPA	Uncladded	49 ± 1	1.61 ± 0.02
	Cladded	51 ± 1	2.05 ± 0.04

the field of ASE fiber lasers, fiber amplifiers or sensors. The study was carried out for transversal excitation and as function of the pump energy, of the illuminated fiber length by means of the VSL, and of the pump polarization.

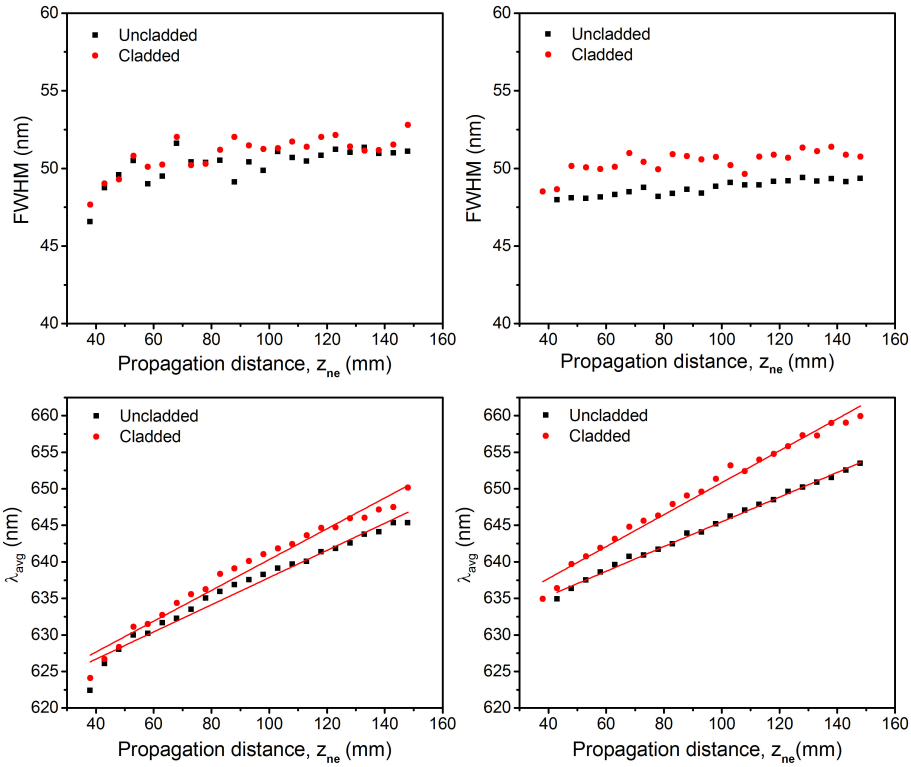

Figure 4.37: FWHM and λ_{avg} of the emitted spectra as functions of the light propagation length for OPA and TPA and uncladded and cladded samples. The red curves on the λ_{avg} represent the linear fittings for the slope calculations.

Result 1 addressed the ASE and gain properties of two R6G doped GI PMMA optical fibers of different dopant concentrations (F12 and F16). The strong influence of the dopant concentration on the ASE performance and on the optical gains of the two fibers was confirmed, obtaining lower ASE threshold and greater gains for the fiber with higher dopant concentration. In particular, 20 times less pump power is needed for this fiber to get the same optical gain. Besides, the variation of the optical gain at each position of the fiber was theoretically analyzed, reaching to the conclusion that the gain in a dye-doped POF can be considered rather constant inside z_e when large enough excitation lengths

are used. Finally, the influence of the pump polarization was determined, showing that lower ASE thresholds and greater gains are obtained when the sample is excited with a perpendicular polarization to the fiber symmetry axis (vertical polarization).

Result 2 approached a detailed study of the emission properties of R6G doped SI cladded and uncladded thermoset fibers. It was seen that lower threshold values were needed for the cladded sample to ASE to occur. Besides, this same sample showed greater gains than the uncladded fiber. For the specific emission $\lambda = 580$ nm a difference of $0,62$ cm^{-1} (2.6 dB/cm) was measured. Moreover, a lower ASE threshold and greater gains were obtained for the cladded sample being pumped with vertical polarization than with horizontal polarization. It was also seen that the uncladded sample with vertical polarization showed greater gains than for the cladded sample with horizontal polarization, what demonstrates that the pump polarization has a greater effect on the optical gain than the effect of having a cladding. With the aim of comparison, the gain values obtained for the thermoset cladded fiber and those previously reported for the GI fiber (F16) were analyzed together. It was seen that in spite of the greater dopant concentration and the higher pump irradiances employed in the thermoset sample, the optical gains are higher for the GI fiber due to the better interaction between dopant and light ($\gamma > 1$). Finally, it was seen that the TPA fluorescence curves were redshifted by approximately 11 nm from the OPA ones for both samples. Slightly greater variations of λ_{avg} with the propagation distance were obtained for the cladded sample.

From all this work, it can be concluded that the best scenario for obtaining ASE and gain from R6G doped POFs would be obtained for

a GI POF of high dopant concentration (without reaching concentration saturation), with a thin cladding, and a excitation polarization perpendicular to the fiber axis. A summary of the main results of this chapter is gathered in Table 4.9.

Table 4.9: Summary of the results from Chapter 4.

Fiber	**ASE threshold FWHM (mJ)**	**Maximum gain (cm^{-1}) / (dB/km)**	**Gain improvement factor with vertical polarization**	**λ_{avg} slope (OPA) (nm/cm)**
F12	0.70 ± 0.05	13.4 ± 0.3 / 56.6 ± 1.3 $\lambda = 565$ nm I = 187 mJ/cm^2	1.23 $\lambda = 575$ nm	—
F16	0.13 ± 0.06	13.0 ± 0.3 / 55.3 ± 1.3 $\lambda = 570$ nm I = 9.4 mJ/cm^2	—	—
Uncladded	0.93 ± 0.06	5.5 ± 0.2 / 56.6 ± 0.8 $\lambda = 580$ nm I = 31 mJ/cm^2	1.29 $\lambda = 580$ nm	1.66 ± 0.07
Cladded	0.67 ± 0.08	6.1 ± 0.3 / 25.9 ± 1.3 $\lambda = 580$ nm I = 31 mJ/cm^2	1.26 $\lambda = 580$ nm	1.94 ± 0.05

Chapter 5

Solar energy concentration using doped POFs

Prologue— *This chapter starts with an overall perspective of the energetic needs and demands of nowadays population, followed by the state-of-the-art in luminescent solar concentrators, from their very first use to nowadays improvements. It describes their operation fundamentals, together with the typical host and dopant materials employed and the common loss sources. An overview of the new concept of FFSC is also described. The first two results comprise various experiments to determine the possible application of several doped POFs as FFSC, such as the the optical losses, the side illumination coupling efficiency and the fluorescent fiber solar concentrator efficiency. Moreover, the design, fabrication and characterization under AM 1.5G standard excitation of several novel double-doped POFs is presented. An analysis of the output power, efficiency and irradiance is carried out under different lighting conditions. A calculation of the power-saturation fiber length and a photostability study are also performed. Finally, the diameter dependence of some of the double-doped fibers is experimentally and theoretically discussed.*

5.1 General background

Due to the world's economic development, the needs and demands of the ever-growing population and environmental issues, such as the global warming, the search for alternative energy sources has become of great urgency. In 2017, the 85% of the global energy consumption came from burning fossil fuels, including petroleum (oil), coal, and natural gas [118]. The use of fossil fuels represents the largest source of carbon dioxide, and as a consequence, it raises serious environmental concerns related to global warming. Furthermore, these kind of energy production are considered to be non-renewable resources, and eventually, they will become too costly to harvest. Renewable energy sources made up 10% of the primary energy consumption in 2017, 7% coming from hydroelectric power and 3% coming from modern renewables such as wind, solar, geothermal and biomass. A graphical representation of the global primary energy consumption by source is shown in Figure 5.1.

Hydroelectric technology produces the majority of power among the so-called renewable energy sources. However, there are relatively few sites where its production is viable, and most of these are already developed. Thus, the projections of a substantial growth in hydroelectric power are low. At the same time, the amount of growth that can be expected from wind power is also limited because suitable locations for wind farms are scarce. PV energy appears to be a promising route to future green energy production, as it has the largest growth prospects among the renewable energy resources. It is abundant, clean and inexhaustible, with high power availability all over the globe. Around 1000 W/m^2 are measured on a clear sky summer day at the equator, although this value decreases at higher latitudes, dropping to approximately half at 60° latitude [119]. The main solar intensity lies in the visible region, as can be

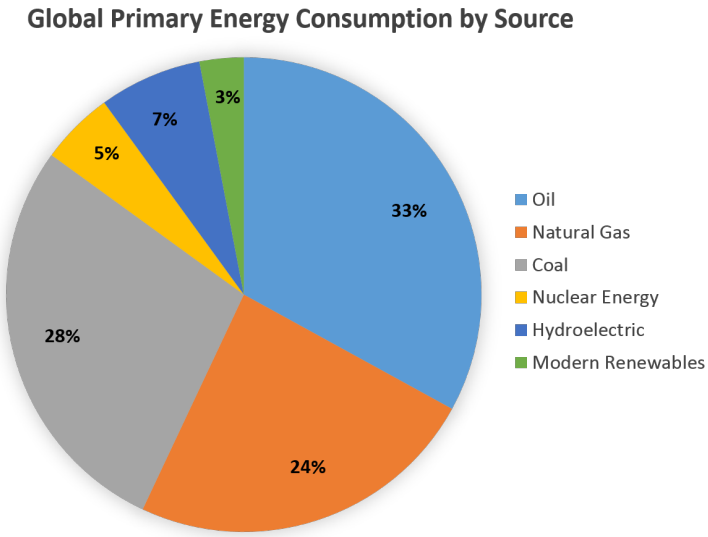

Figure 5.1: Representation of the global primary energy consumption by source in 2017. (Data from the Statistical Review of World Energy 2017 [118]).

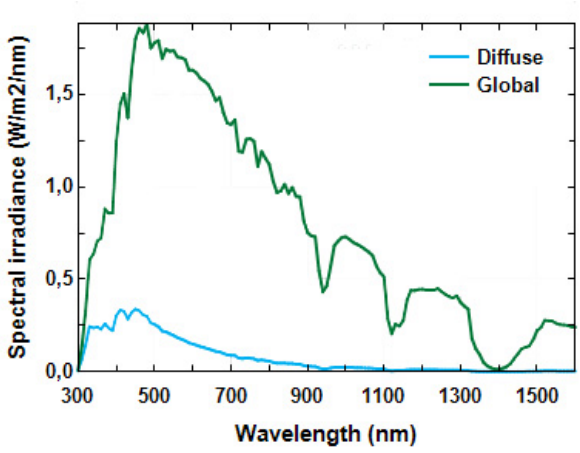

Figure 5.2: Solar radiation spectra: global standard AM 1.5G spectrum in green, and diffuse light spectrum in blue.

seen in Figure 5.2 which shows the global standard spectrum AM 1.5G that corresponds to the terrestrial blue sky conditions. This figure also illustrates the diffuse light spectrum that corresponds to the scattered

solar light by molecules and particles in the atmosphere.

The goal of converting sun-light into electricity using PV cells has been subject of active research for more than sixty years, with the silicon-based solar cells dominating the field [120]. Considerable progress has been made in PVs since then. However, the production of solar energy in a way that can compete economically with conventional energy sources remains still hard to achieve due to two major drawbacks. On the one hand, the limited resources of high purity refined silicon, together with the large areas of solar cells that are required, increase the cost of the system. On the other hand, to maintain the high conversion efficiencies of the solar cells, a very precise sun tracking system is needed, which also leads to a rise in the final cost of the system. A possible approach to reduce the expenses of the solar power harvesting system is the concentration of sunlight into a smaller area of solar cells by using less expensive optical devices, such as concentrators, mirrors and lenses, also known as geometric solar concentrators (GSC) [121, 122, 123, 124]. In Figure 5.3 some examples of these sun-light GSC systems are shown.

Despite the high power concentration efficiencies that can be achieved by these systems, there exist some major drawbacks. Very accurate alignment of the optics is required, and there is still a need of a sun tracking system. Misalignments in the optics and errors in tracking the sun can cause the sun image to fall outside the aperture of the solar cells, and thus, lead to a dramatic drop in the efficiency. These reasons make these kind of systems yet not competitive with fossil fuels in the global energy market.

It was in the 1970s that the concept of luminescent solar concentrator (LSC) was first proposed by Weber and Lambe [125]. In LSCs, luminescent materials are embedded or coated on transparent waveguides so that they absorb part of the sun-light and re-emit and transport it

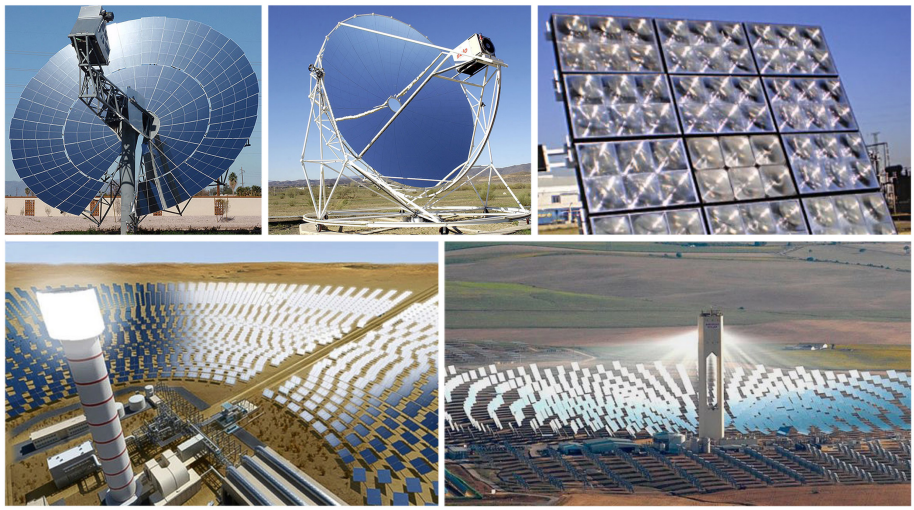

Figure 5.3: Examples of geometric solar concentrators for commercial use.

to the edges of the layer where the PV cells are attached (see Figure 5.4). These systems present multiple advantages, such as no need of a sun tracking system, invariable performance under diffuse light conditions, and distributed heat dissipation over a large area. Besides, the use of cheap transparent polymers as host materials, and the location of the PV cells at the edges of the active layer —requiring a much smaller area of them— decrease considerably the overall cost of the PV energy production. Nevertheless, the major drawback of the planar LSC lies in the limitation in coupling between the edge of the active layer and the PV cell and also the difficult wiring method for light transmission. Focusing on the aforementioned limitations, a new concept of cylindrical LSC based on doped polymer optical fibers, namely fluorescent fiber solar concentrator (FFSC), appears to be a highly competent solution. Further aspects of the LSCs and FFSCs will be detailed in the following sections.

5.2 Luminescent solar concentrators

5.2.1 Past, present and future

Research on LSCs began in 1976 with the publication of the first paper reporting the use of luminescent materials in conjunction with total internal reflection waveguide mechanism for sun-light collection [125]. In this work, four main advantages of this new light collection strategy were detailed, which are still highly considered in the research and development of nowadays LSCs: (a) no need of a sun-tracking system; (b) invariable performance under direct and diffuse light conditions; (c) reduction of heat dissipation problems in solar cells — the energy loss in shifting photons to longer wavelengths is distributed over a large area of collector—; and (d) possibility of using photocells with optimized response to certain wavelengths. Extensive theoretical and experimental studies were carried out in LSC technology in early years, investigating different methods and materials [126, 127]. However, LSCs were relegated to a period of inactivity due to the limitations of that time materials, until more advanced ones were designed. In fact, there is a significant reduction in the number of papers on LSC devices in the 1990s, raising up strongly in the 2000s. Novel luminescent luminophores such as quantum dots, rare earth ions, semiconductor polymers, and also the Lumogen series of organic luminophores developed by BASF [128], have renewed the interest in the LSC development [129, 130, 131, 132, 133]. A review covering efficiency advancements in LSCs was published in 2012 [134].

Theoretically, LSC should achieve the same conversion efficiency as a single junction PV, but they undergo a larger number of loss mechanisms. These losses involve typical conversion efficiencies remain lower

than those of standard PV-cells under direct solar radiation. Therefore, LSCs are still unlikely to see a leading role in the global solar energy market. However, due to the advantages that LSCs present combined with commonly available materials and ease of processing, there exist an opportunity to develop useful and cost-competitive devices that could find a place in niche markets. A highly potential market lie in building-integrated photovoltaics (BIPVs) in cities, where the cost of land for the installation of ground PV is prohibitively high, and the rooftop space is too scarce to accommodate PV modules. Besides, any solar energy generator destined to be used in urban scenarios will be subject to various degrees of shading and light scattering from trees, other buildings, or clouds, what decreases the performance of the system. Thus, the integration of LSC technology into building facades creating aesthetically pleasing structures while generating power for local utility is being investigated [135, 136, 134]. LSCs offer a unique possibility for 'invisible' architectural integration of solar energy harvesting devices. The implementation of LSCs in BIPV plays a key role in the transition to fully energetically sustainable architecture, so-called net zero energy buildings (NZEBs), whose energy consumption is nearly fully counterbalanced by renewable energy generated on site, what also provides rapid returns on investment. The European commission's *Energy Performance of Buildings Directive* requires that all new buildings to be NZEB by the end of 2020 [137]. Besides, a further dramatic increase in electrical demand is expected in the near future due to the widespread use of fully electrical vehicles. For all these reasons, great efforts are being dedicated to the development of integrated PV technologies. Further LSC applications include indoor day-lighting [138, 139] and energy harvesting for remote power supplying [140].

5.2.2 LSC operation

LSC consist of a polymeric or glassy optical waveguide doped or coated with luminescent species. Direct or diffuse sun-light penetrates the waveguide, and part of the solar spectrum is absorbed and re-emitted to longer wavelengths by the dopants. A fraction of the emitted light is trapped inside the waveguide and guided by total internal reflection to its edges, where small area of solar cells is attached to convert it into electricity. Figure 5.4 illustrates the operating principle of a typical planar LSC.

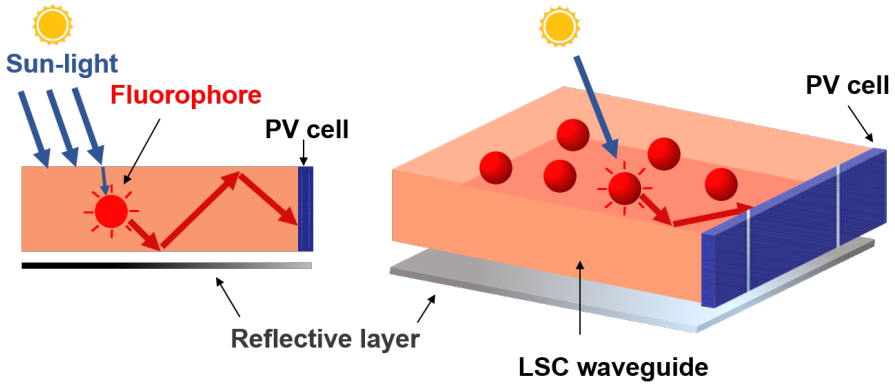

Figure 5.4: Schematic diagram of a basic square planar LSC showing its operating principle. The solar radiation enters the LSC waveguide, a photon is absorbed and re-emitted by a luminescent molecule, and then guided by total internal reflection to a PV cell attached at one of the edges.

The use of PV cells can be reduced in more than 90%, and the materials employed as host medium are much less expensive, considerably decreasing the module price. The polymer waveguide is lighter than the silicon PV cells, what involves a reduction in weight and makes LSCs viable for building integrated solar energy technology. Furthermore, they accept both direct and diffuse light from a wide range of angles, and thus, expensive sun-tracking system is not required. The

efficiencies of LSCs are nearly unaffected by shadowing and diffuse light conditions. Additionally, it has been demonstrated that LSCs are more efficient at concentrating diffuse light than direct light, with a factor of around $1.3-1.5$ times [141, 11]. On the one hand, this may be due to the blue shift of the maximum of the diffuse light spectrum in comparison to the clear sky spectrum —many dyes absorb close the near-ultraviolet and blue range—, and to the absence of long infra-red tail which is useless for photovoltaic conversion. On the other hand, the photodegradation of the LSC depends on the excitation intensity, i.e., higher excitation intensities present in direct sun-light involve higher photodegradation. Besides, non-radiative energy transfers between luminescent molecules may also increase with the excitation intensity, leading to a rise in the fluorescence quenching [142].

5.2.3 Loss mechanisms in LSCs

One of the major efficiency limitations of LSCs comes from the several processes that introduce losses all along the light path. Figure 5.5 illustrates the loss processes involved in LSCs. These loss mechanisms also occur in any other application involving doped POFs or waveguides.

Figure 5.5 represents the simplest form of a planar rectangle of a certain optical quality host material doped with luminescent species. As shown in this figure, incident solar radiation impinges on the top surface of the LSC. The luminescent dopants have finite absorption bands that covers just a part of the solar spectrum. The portion of sun-light that is not absorbed by the dopants, passes through the LSC system with no change (1). In some systems, reflective materials are placed below the LSC so that this light bounces back, and it is not lost through the bottom surface. The ideal approach would be to absorb as much of

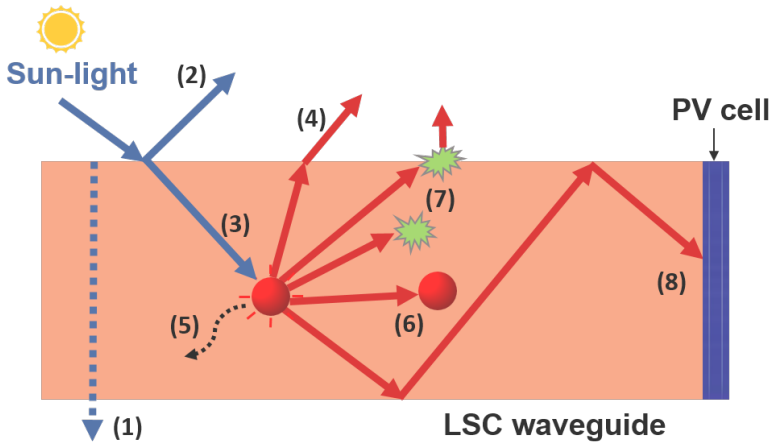

Figure 5.5: Schematic illustration of the loss mechanism processes involved in luminescent solar concentrating devices.

the solar spectrum as possible. For this purpose, dopants with broad absorption cross sections, or multiple dyes with cascade absorption and emission are used.

A small portion of the incident light will be reflected at the LSC surface (2), and part of the solar spectrum that overlaps with the absorption band of the dopant will be absorbed and emitted isotropically in the LSC (3). Some of this emitted light may arrive at the LSC surface at angles sharper than the critical angle, so that internal reflection cannot take place and light escapes out of the waveguide (4). The amount of energy lost in this way is estimated to be around 30% of all absorbed energy, which represents the major loss source of an LSC [143]. A possible approach to minimize this losses is by aligning the luminophores, and therefore, controlling the spatial distribution of the emitted light [144, 145, 146].

Another source of loss comes from the absorbed photons that are not emitted, but instead lost non-radiatively as heat and vibrations (5). Many fluorescent materials can be engineered in a way to minimize the

non-radiative energy loss, and luminophores with quantum efficiencies exceeding 0.95 are already available. Due to the overlap between the absorption and emission spectrum of the dopants, part of the emitted photons will be re-absorbed. Re-absorbed light will experience some red-shift, and will be re-emitted isotropically (6). Reabsorptions are not losses by themselves, but the probability of losing a photon increases due to limited quantum efficiencies of the luminophores —resulting in non-radiative energy dissipation—, and to re-emissions into the escape cone. Most organic dyes used in LSCs have small Stokes-shifts, involving large overlaps between the absorption and emission spectra. To reduce re-absorption events, luminophores with minimum spectral overlaps have been studied, such as lanthanides and quantum dots. Engineered materials that increase the Stokes-shifts of organic dyes have also been investigated [147]. Another approach to reduce the probability of encounters of the emitted light with other dopant molecules, is to dope the host materials only on its surface. In this way, the emission may be transported predominantly in the clear host material, and it will only encounter the dopant layer again just in every internal reflection [148]. Scattering centers in the waveguide body and surface, and intrinsic losses of the host material, also contribute as loss sources (7). These can be avoided or, at least, minimized by using high quality optical materials as host medium. Finally, a portion of the light emitted by the luminophore molecules reaches the end of the waveguide where the PV cells are attached (8). Except for some power loss due to imperfect coupling from LSC to the PV cells, this is the light available for power conversion.

5.2.4 LSC materials

5.2.4.1 Host materials

The host material of a LSC waveguide acts both as a container medium for luminescent species and as structural support for the solar concentration system. The role of the host material in the light propagation process has been long overlooked due to the dominant loss sources of the luminophores. With the synthesis of new dopants, and the research of engineered materials that increase the Stokes-shift of the luminescent species, the contribution of the host medium can no longer be negligible. The first studies discussing this fact have recently been published [149, 150].

The desired fundamental properties of the host materials include: (a) high transparency in the visible and near-infrared spectral ranges; (b) proper solubility parameters with respect to the chosen luminophores to achieve complete dissolution —what avoids scattering centers that could be formed by material aggregation—; (c) high photostability and environmental durability; (d) compatibility with the processing temperature ranges of the luminescent species; (e) suitable refractive index to minimize losses through the waveguide surface and to increase the numerical aperture; and (f) cost-effective production. The materials that have been used as hosts for LSC are polymers and glasses. However, the fabrication temperature range of glasses is not compatible with the significantly lower temperatures that organic materials can tolerate. For instance, the perylene-deriative Lumogen F series dyes can tolerate up to 300°C [128], whereas the manufacturing of glass involves temperatures up to 1100°C [151]. Besides, the weight of glass can be disadvantageous in some applications where light-weight devices are required.

As it happened with POF light sources and amplifiers, by far, the most commonly host material employed for LSCs is PMMA, due to its very good material properties. As seen in Section 2.3, it is an easy-handling material to work with, and it shows excellent transparency in the visible range. Some other polymers used as host matrices are polystyrene, and different formulations of polycarbonate. These materials also show high optical transparency in the visible and near-infrared range, environmental stability, good dye solubility, and commercial availability. Their optical qualities and efficiencies for LSC use are reported in the recent work carried out by Zettl et al. [150].

5.2.4.2 Dopant materials

When a LSC waveguide is used for sun-light concentration it will absorb a smaller fraction of solar radiation than what a silicon PV cell will do. For a single visible-emitting dye with a FWHM of around 100 nm this percentage is estimated to be about 20% of the incident AM 1.5G radiation. From the material point of view, the greatest efforts in LSC research have been put on the study and development of the luminescent materials.

To maximize the output power of an LSC, it is necessary to harvest as much solar radiation as possible, thus the ideal dopant material should have a broad absorption band designed to efficiently absorb the solar spectrum. Some other properties that the dopant for LSCs should meet are those listed for POF light sources and amplifiers, such as high quantum efficiency, high solubility in the doped medium, a small overlap between absorption and emission bands, and high thermal and photochemical stability to be capable to endure hazardous outdoor environmental conditions. In general, organic and inorganic materials possess

unique characteristics that satisfy some but not all of the aforementioned criteria, and thus, finding all these ideal properties in a unique material remains still a challenge. In Table 5.1 the ideal properties for LSC are shown for organic, inorganic, and hybrid materials (organic-inorganic). As can be seen, is seems likely that all the desired properties shown in this table could be met by combining organic and inorganic materials into a hybrid device.

Table 5.1: Summary of the desired dopant properties for LSC operation and characteristics of the organic, inorganic, and hybrid materials [131].

Desired property	**Organic**	**Inorganic**		**Hybrid**
		rare earths	**QDs**	
High absorption cross-section	✓	x	✓	✓
Minimal re-absorption	x	✓	x	✓
Quantum efficiency $> 90\%$	✓	✓	x	✓
Stable for > 10 years	✓[a]	✓	x	✓

[a]Not all materials

Initial LSC research employed organic dyes originally developed for dye-lasers, such as rhodamine 6G, DCM, and Coumarin, as the chemistry of mixing them with polymers was well-characterized and they were widely available. Many of these dyes have near-unity quantum efficiencies, what make them ideally suited for LSCs. However, their use showed two main drawbacks: they have limited photostability, and they exhibit high self-absorption due to small Stokes-shifts (it has to be noted that large Stokes-shifts eventually goes together with low quantum efficiencies, as the spectral shift results from non-radiative relaxations). This fact resulted in a downward period in LSC research after the initial peak

in the 1970s. During the last years of the 20th-century, several new luminescent materials were developed, including novel organic dyes. In 1997, BASF company released the Lumogen F series dyes [128]. These perylene derivatives, also known as collector dyes, have quantum efficiencies close to 1, and are highly photostable so that they can be used in outdoor environments. An example of the absorption and emission bands of one these dyes is shown in Figure 5.6, specifically the Lumogen F Orange 240 dye. An outdoor study carried out by Mansour et al. employing BASF dyes doped in PMMA showed that the BASF-241 dye degraded 6.2% of its initial value after a year of daylight exposure [152]. Some other studies showed that the most degraded dye was the Lumogen F Violet 570, due to its susceptibility to UV light, and that the most stable one was the Lumogen F Red 305 [153]. These dyes have extensively been studied in LSC systems [154] and in daylighting applications among others [155].

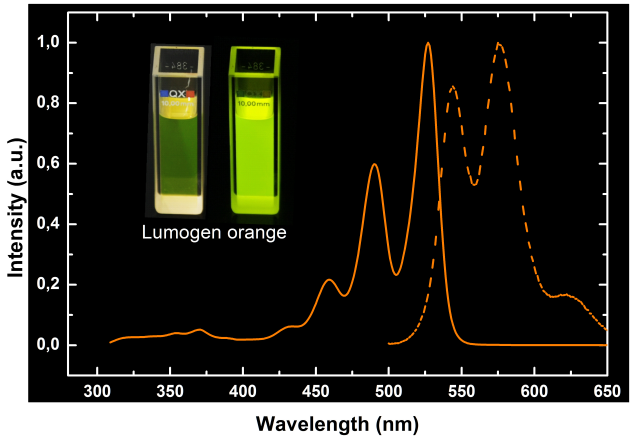

Figure 5.6: Absorption and emission bands of the Lumogen F orange 240 dye. Inset: photograph of the dye in dissolution with environmental illumination (left) and under UV excitation (right).

To improve the performance of the organic dye-based LSCs, some approaches have been investigated. By employing material engineering, the dye molecules can be aligned in the host material in a desired way so

that the emitted light distribution can be controlled, and therefore, the optical losses through the escape cone are considerably reduced [144, 145, 146]. Besides, multiple dyes with cascade absorption and emission can be employed together in the same matrix, or in separate parallel waveguides, to cover a larger solar spectrum range. It has been shown by Batchelder et al. that up to 75% of the solar spectrum can be absorbed using a multidye system [127]. In this configuration, the emission spectrum of each of the dyes needs to match the absorption spectrum of the next dye, while the output emission of the system corresponds to that of the dye with longest emission wavelength [156].

Among inorganic luminescent species, rare earth ions and quantum dots (QDs) have extensively been studied due to their considerably differing properties. QDs have broad absorption and emission bands, and their emission peaks can be tuned from 850 nm to 1900 nm. However, the quantum efficiencies of the commercially available QDs are low, and they lack of long-term stability. On the other hand, rare earth ions present excellent photostability and minimum re-absorption losses. The quantum efficiency of these materials vary a lot depending on the host matrix and dopant concentrations, but values above 90% have been reported [157]. Nevertheless, they have low absorption coefficients, and high dopant concentrations are required to harvest a significant fraction of the solar spectrum. For overcoming the drawback of having low absorption coefficients, organic molecules and rare earth ions can be combined forming a organo-metallic complex or chelate. The organic ligand absorbs the solar radiation and transfers the energy to the rare-earth ion. Because an organic molecule is used, higher absorption cross sections are obtained (similar to those of organic dyes) in comparison to the ones of rare-earth particles. An example of an organo-metallic chelate is shown in Figure 5.7, illustrating the absorption and emission bands of the $Eu(TTFA)_3Phen$ dopant.

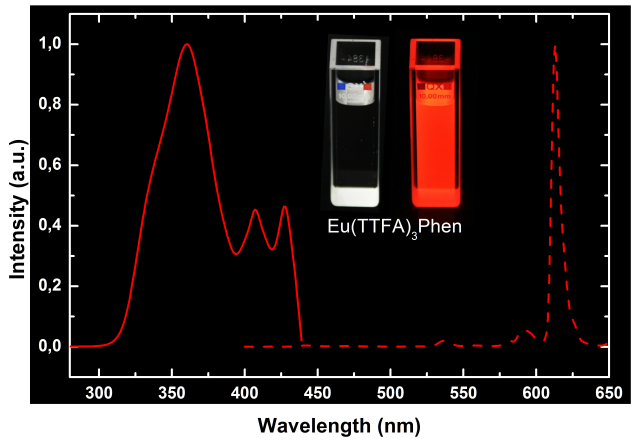

Figure 5.7: Absorption and emission band of the $Eu(TTFA)_3Phen$ chelate. Inset: photograph of the complex in dissolution with environmental illumination (left) and under UV excitation (right).

5.3 Fluorescent fiber solar concentrators

The geometry of the LSCs plays a very important role in the device performance and design. Traditionally, most of the researched LSCs have planar configuration. Nevertheless, as the light produced by these devices is not a point light source, the planar LSCs show a major limitation in coupling between the edges of the active layer and the PV-cell, and also to passive POFs for remote energy conversion. In some applications, such as in BIPV, sunlight is not able to reach many areas as roofs, basements, and electrical panel rooms, among others. Therefore, there is a need of waveguiding light to remote areas for both remote light-to-electricity conversion and indoor day-lighting. One of the most important features involved in light transportation lies in the wiring method, which must be as easy as for electrical wires. Only optical fibers appears to be competent for this requirement. Focusing on the aforementioned needs and demands, FFSCs have been proposed as an efficient solution. In these de-

vices, the doped POF absorbs the incident sunlight on its outer surface, and it plays the role of a waveguide for transmitting this fluorescence to the fiber edges where PV-cells are attached (see Figure 5.8 (left)). The cylindrical waveguide structure of POFs adds several benefits. On the one hand, they are light-weight, thin and flexible, which permits an easy manipulation by the user. On the other hand, they can easily be attached to transparent optical fibers for light waveguiding, which allows spatial separation between the light harvesting system and the final system placement when needed (see Figure 5.8 (right)). Moreover, the use of doped POFs to realize flexible and low-weight LSCs may enable solar energy harvesting in mobile applications.

Some theoretical studies have been carried out in the last years involving comparisons between cylindrical and planar LSCs [158, 159, 160]. These theoretical analysis suggest that the cylindrical geometry allows an increase of the concentration factor of the LSC device, due to the larger area-ratio between the illuminated length and the edges. In the research developed by K.R. McIntosh et al. it was found that when luminescent emission occurs close to the surface, the optical concentration of a cylindrical LSC is 1.0–1.9 times greater than an equivalent planar LSC, and therefore, that the cylindrical LSC requires a smaller area of solar cells to produce the same amount of electricity as an equivalent square LSC [158]. It has also been found that for the proper functioning of a FFSC, the luminescent molecules must absorb and re-emit light very close to the surface. For this reason, clad-only doped fibers have started to be investigated [161, 148]. Recently, a study on different fiber structures has been published targeting on the increase on the efficiency of the FFSC [162].

A single piece of fiber forms an independent LSC itself, and the juxtaposition of multiple fibers enables to cover a large collection surface.

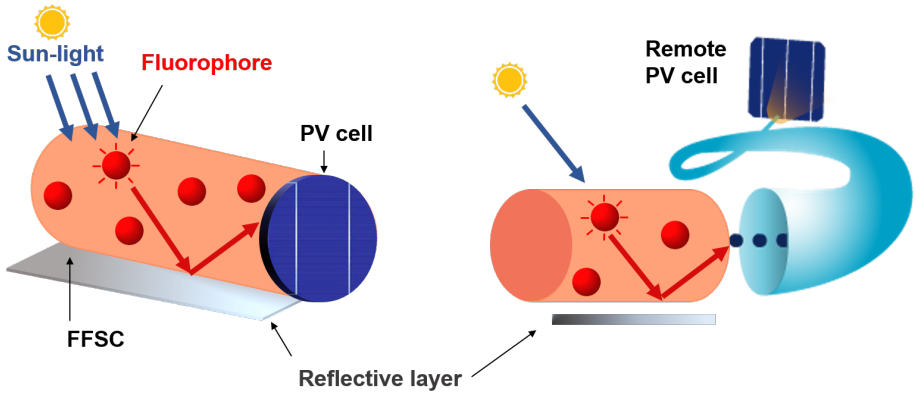

Figure 5.8: Schematic diagram of a fluorescent fiber solar concentrator. The solar radiation enters the FFSC waveguide, a photon is absorbed and re-emitted by a luminophore molecule, and then guided by total internal reflection to a PV cell attached at one of the edges (left). Schematic of the operating principle of a FFSC for remote energy production. The active fiber is butt-coupled to a passive POF to waveguide the luminescence to a remote PV cell (right).

These fibers can be gathered into bundles that are directly attached to PV-cells, or they can be independently butt-coupled to passive optical fibers when the energy conversion takes place at a distance from the light collection area.

5.4 Experimental methods: efficiency calculations

- **Side illumination coupling efficiency, η_{SIC}**

An important feature of a FFSC relies on how much light is absorbed through its surface. To study this, the power absorbed by each of the fibers, P_{abs}, is calculated as a function of the side excitation power P_{pump}. The excitation dimensions of the light source was adjusted to cover the whole section of the fiber, i.e., a spot of 1 mm. The P_{abs} is defined as the

subtraction between the P_{pump} and the power measured with a silicon photodetector (Newport, 818-SL) just on the other side of the fiber, P_{back}, as it is illustrated in Figure 5.9. The side illumination coupling efficiency $\eta_{SIC}(\lambda)$ when the fiber is excited at a specific wavelength was calculated from the following equation:

$$\eta_{SIC}(\lambda) = \frac{P_{pump} - P_{back}}{P_{pump}} 100 = \frac{P_{abs}}{P_{pump}} 100 \ (\%) \tag{5.1}$$

The η_{SIC} was also calculated employing a broadband light source (Energetiq, EQ-99-FC LDLS) that covers a wavelength range from 1900 to 2100 nm. In this case the η_{SIC} would not be calculated for a specific λ but to the sum of all the excitation wavelengths.

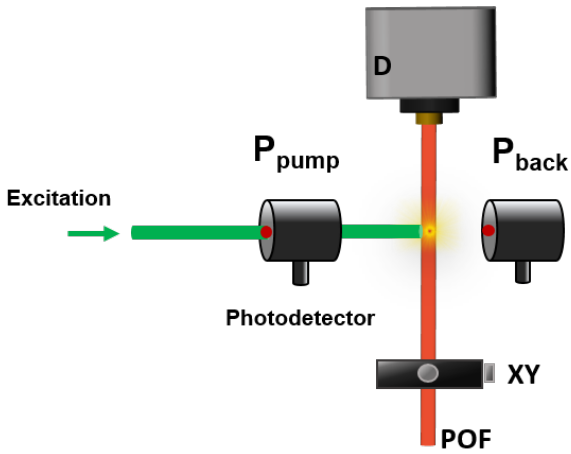

Figure 5.9: Illustration of the side illumination coupling efficiency η_{SIC} calculation.

- **Fluorescent fiber solar concentrator efficiency $\eta_{\mathbf{FFSC}}$**

The FFSC efficiency relates the power that impinges on a specific fiber length z_e, and the output power that the fiber is able to generate

from this excitation at one of its ends. Analytically, it is defined as the ratio between the power measured at the fiber end P_{fiber}, and the lamp power that impinges on the fiber surface P_{lamp}, as depicted in the following equation:

$$\eta_{FFSC} = \frac{P_{fiber}}{P_{lamp}} 100 \ (\%) \tag{5.2}$$

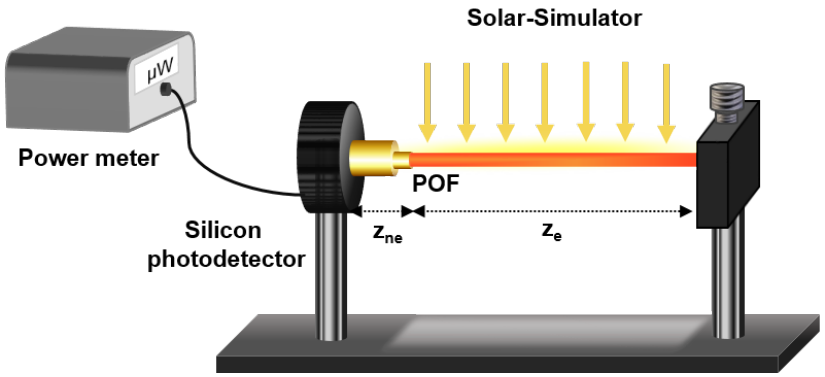

Figure 5.10: Illustration of the fluorescent fiber solar concentration efficiency η_{FFSC} calculation.

An illustration of the experimental set-up for η_{FFSC} measurements is shown in Figure 5.10. As can be seen, a light source excites the fiber laterally on a length z_e. The output power is measured by means of a silicon photodetector with a power meter. The recorded power values were corrected employing the responsivity curve of the photodetector and the emission spectra of the fibers. Two different types of lamps have been employed. For the first two results a halogen lamp (OSRAM, Haloline Eco) was employed, whereas for the double-doped fibers a 1 Sun AM 1.5G solar simulator (Newport, Oriel Desktop 91160-1000) was used.

5.5 Result1: POFs doped with organic materials as FFSCs

The aim of this study was to carry out an optical characterization of several POFs doped with lumogen red and conjugated polymers, targeting FFSC applications. The analysis includes a characterization of the optical losses, and a calculation of the side illumination coupling efficiency and of the fluorescent fiber solar concentration efficiency. The results were thoroughly compared, and interesting conclusions were obtained for upcoming works on the field of FFSCs.

5.5.1 Samples

The main characteristics of the fibers analyzed are summarized in Table 5.2. Lumogen red doped samples (LR01 to LR04) were manufactured by our research collaborators from Technical University Braunschweig (TUB [163]). The preforms were polymerized in bulk, filling borosilicate tubes of 10 mm with a nitrogen saturated solution of MMA, Lumogen F Red 300 in different concentrations, lauroylperoxide (0.03 mol%) and 1-butyl-mercaptan (0.2 mol%). These tubes were sealed and transferred to a heating cabinet, where they were heated to 100°C over five days and they were maintained at that constant temperature for another day before cooling them down to room temperature along 24 h. After removing the glasses, the preforms were heated up to 230°C in the heater unit of the drawing tower and drawn to fiber by applying a constant force. In the case of the cladded fiber, a film of 20 μm of commercial PC404F-AP material was applied through a nozzle and cured by UV-irradiation to form the cladding. The last three fibers are doped with three different conjugated polymers, namely poly(9,9-dioctylfluorene)-

alt-benzothiadiazole (F8BT), poly(9,9-dioctylfluorene-alt-bithiophene) -(F8T2), and poly[2,7-(9,9bis(2ethylhexyl)fluorene)-alt-2,5-terthiophene] (PF3T). They were produced by the Italian POF manufacturing company Luceat S.p.A using an adapted preform-drawing technique, of which further details are described in [164]. The total fiber diameter of all the samples is 1 mm and the host polymer is PMMA in all cases.

Table 5.2: Summary of the main characteristics of the POFs doped with lumogen red and conjugated polymers.

Fiber code	**Type**	**Dopant**	**Conc. mol%**	**Manufac.**
LR01	SI cladded	Lumogen F Red 300	0.0001	TUB
LR02	SI cladded	Lumogen F Red 300	0.0005	TUB
LR03	SI cladded	Lumogen F Red 300	0.03	TUB
LR04	SI uncladded	Lumogen F Red 300	0.03	TUB
F8BT	SI uncladded	poly(9,9-dioctylfluorene) -alt-benzothiadiazole	0.003	Luceat
F8T2	SI uncladded	poly(9,9-dioctylfluorene-) alt-bithiophene	0.003	Luceat
PF3T	SI uncladded	poly[2,7-(9,9bis(2ethylhexyl)) fluorene)-alt-2, 5-terthiophene	0.003	Luceat

An example of the absorption and emission spectra of two of the samples are shown in Figure 5.11 measured following the method described in Section 4.2. As can be seen, there exists an overlap between the absorption and emission curves on both fibers. This overlap is a typical signature of dye dopants and was detected for all the analyzed fibers. For FFSC applications where the number of emitted photons plays an important role on the final efficiency, the overlap should be as small as possible to avoid photon loss by reabsorption events.

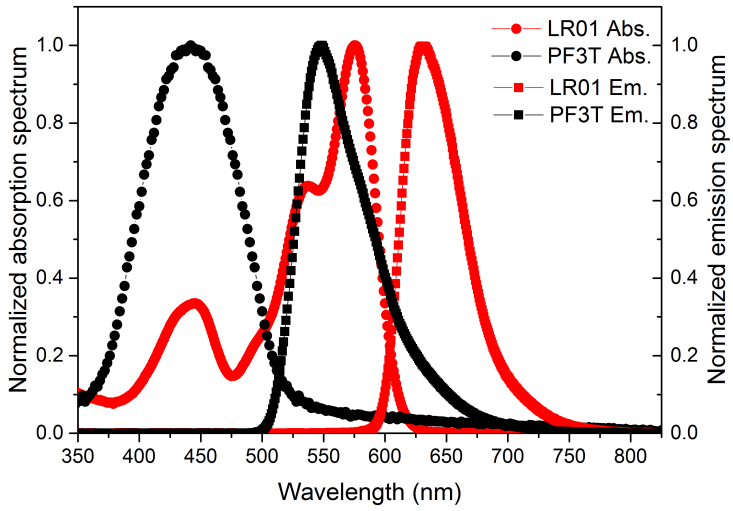

Figure 5.11: Absorption and emission spectra of the LR01 and PF3T samples.

5.5.2 Optical losses

In this subsection, the dependency with the propagation distance up to the detector z_{ne} is analyzed, and the attenuation coefficients are calculated. The experimental method employed was the SIT showed in Figure 4.4. The excitation was enabled by a tunable laser, and each sample was excited around its maximum of absorption (520 nm for the LR01-04 samples, and 457 nm for the conjugated polymers) with a low pump irradiance of around 20 mW/cm^2.

Figure 5.12 represents the progression of the average emission wavelength λ_{avg} for all samples. As expected, all fibers undergo a red-shift on their emission spectrum when the non-excited length of the fiber is increased, which is directly related to the overlap between the absorption and the emission spectra. For the fibers analyzed, lumogen red doped samples exhibit the smallest red-shift.

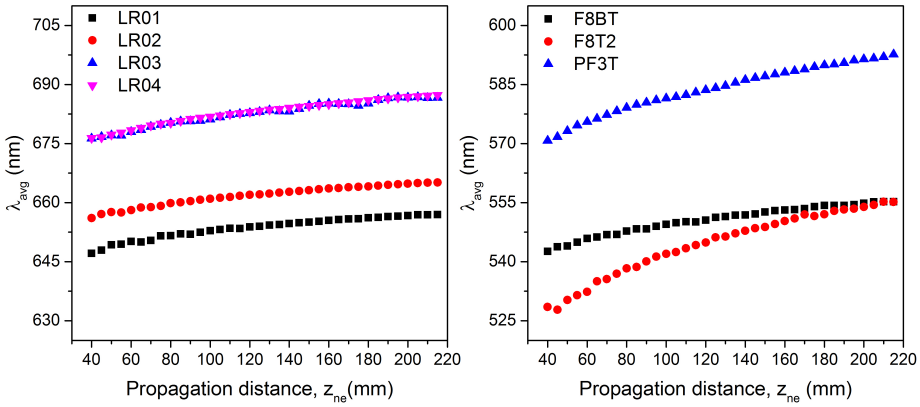

Figure 5.12: Evolution of λ_{avg} as function of z_{ne}. LR01-04 samples were excited at 520 nm, whereas the conjugated polymers were pumped at 457 nm. $I = 20$ nW/cm^2.

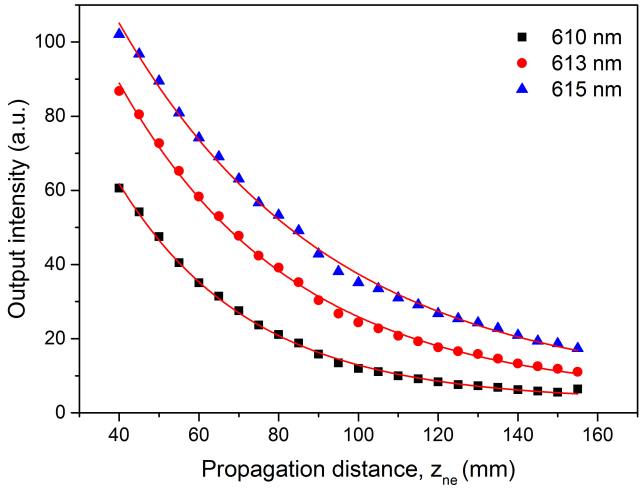

Figure 5.13: Evolution of the output intensity with z_{ne} at three different wavelengths (610, 613 and 615 mm) for LR02 sample. The solid red lines represent the fitted curves of equation (3.9).

Figure 5.13 shows an example of the decrease on the intensity with z_{ne} for three different emission wavelengths (610, 613 and 615 nm) for LR02 sample. The attenuation curves obtained by fitting equation (3.9) to the output intensity curves for several wavelengths are shown in Figure

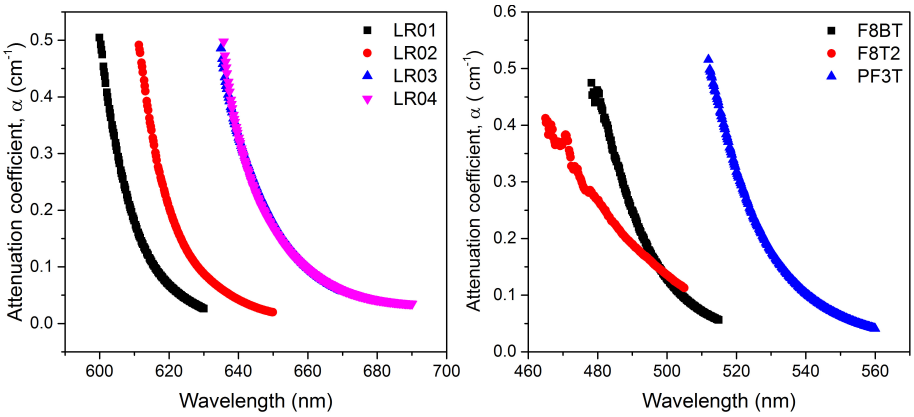

Figure 5.14: Attenuation coefficients of LR and conjugated polymer samples measured by the SIT. LR samples were excited at 520 nm, whereas the conjugated polymers were pumped at 457 nm. The relative error in the obtained attenuation coefficients is $\sim 4\%$.

5.14. As can be observed, the fibers doped with conjugated polymers show slightly higher values of attenuation in the region where the dopant absorption tends to be negligible. In particular, the F8T2 sample is the one with the highest values of attenuation, what could be due to the characteristics of the fiber fabrication method.

5.5.3 Side illumination coupling efficiency

The samples were excited by a tunable laser with an excitation length of 1.2 mm, and a pump power range from 1 mW to 30 mW. The lumogen doped fibers were pumped at 520 mm, whereas the conjugated polymer doped samples were excited at 435 mm, wavelengths that correspond to values around their absorption peaks.

Figure 5.15 shows the power absorbed by each of the samples as a function of the pump power measured as described in Section 5.4. As can be seen, the experimental points follow a linear dependence with

the pump power, with relative errors less than 1%. The values of η_{SIC} calculated following equation (5.1) are gathered in Table 5.3. As can be seen, the fibers with the highest η_{SIC} turned out to be LR03 and LR04 with values of around 95%. LR02 also demonstrates high enough values of η_{SIC}, but fibers doped with conjugated polymers show values below 60% in all cases.

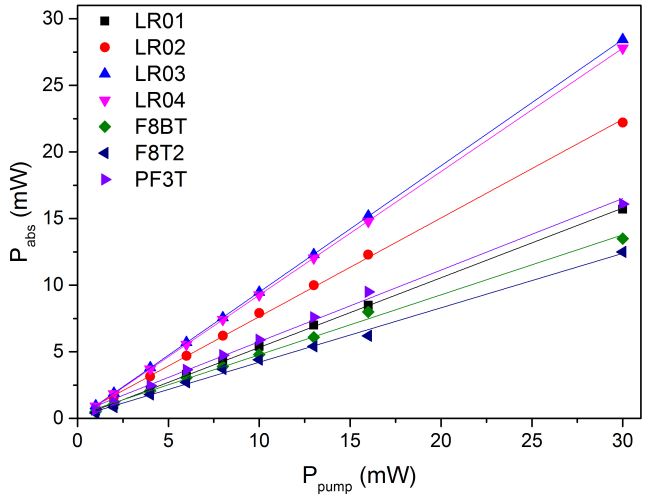

Figure 5.15: Power absorbed sideways as a function of the pump power for η_{SIC} calculation. The fibers were pumped with a femtosecond laser at wavelengths around their absorption peaks. The solid lines represent linear fittings.

From these study, it has been proven that there exists a strong dependence with the dopant concentration and the η_{SIC}, as it could be expected. Focusing on lumogen red doped fibers LR01, LR02 and LR03 with dopant concentrations of 0.0001 mol%, 0.0005 mol% and 0.03 mol% respectively, it can be observed that greater dopant concentrations yield higher η_{SIC}. Following these results, it could be thought that greater dopant concentrations would always result in higher η_{SIC}, and therefore, become more suitable for FFSC applications. However, there also exists a saturation concentration level induced by the aggregates molecules

formed when high dopant concentrations are used, which could become counterproductive leading to a drastically decrease of the fluorescence emission induced by self-quenching and an increase of the losses [165]. Nevertheless, as for the samples analyzed in this study the efficiency still increases with concentration, it could be affirmed that dopant saturation limit is not reached yet.

Table 5.3: Values of the side illumination coupling efficiencies η_{SIC} of POFs doped with lumogen red and conjugated polymers. The relative error of the obtained values is less than 1% in all cases.

	LR01	**LR02**	**LR03**	**LR04**	**F8BT**	**F8T2**	**PF3T**
η_{SIC} (%)	53	77	95	93	48	39	58

5.5.4 FFSC efficiency

In this last section, the η_{FFSC} was calculated following the set-up shown in Section 5.4 and equation (5.2). The excitation source was halogen lamp with an intensity at a distance from the fiber of 36 cm of 0.38 kW/m^2, which corresponds to approximately half the sun radiation in the range between 400 and 1100 nm. The power emitted by the fiber was measured at one of the fiber ends with a total illuminated fiber length of 4.5 cm and a non-excited fiber length of 3.3 cm corresponding to the SMA connector.

The η_{FFSC} values for each of the fibers are shown in Table 5.4. As can be observed, the fiber with the highest η_{FFSC} results to be LR03 with a value of 0.26 (%). It should be noted that there is a considerable difference between LR03 and LR04, which are fibers with the same dopant concentration with the only difference that LR03 has a thin cladding and LR04 is an only core fiber. In the previous section it was demon-

strated that these two fibers showed the same side illumination coupling efficiency, as it was expected for the same dopant concentration. However, LR03 presents 2.6 times greater η_{FFSC} than LR04. These results reinforce the fact seen in the previous chapter that the presence of a thin cladding is essential to help the emission to be trapped and guided through the core, and to minimize surface scattering losses (see Section 4.4). The fibers with the lowest η_{FFSC} are those doped with conjugated polymers. This may be caused because their absorption spectra lie in the near-ultraviolet spectral region where the lamp radiation (and the solar radiation) is weaker. It can also be related to the low dopant concentration employed in these fibers.

Table 5.4: Values of the fluorescent fiber solar concentration efficiencies η_{FFSC} of POFs doped with lumogen red and conjugated polymers.

	LR01	**LR02**	**LR03**	**LR04**	**F8BT**	**F8T2**	**PF3T**
$\boldsymbol{\eta_{FFSC}}$ **(%)**	0.045	0.12	0.26	0.1	0.007	0.003	0.005

5.5.5 Conclusions

In this work, an optical characterization of four lumogen red doped and three conjugated polymer doped POFs was carried out focusing on future applicabilities in the field of FFSCs. It was seen that all fibers undergo red-shifts on their emission spectra when the non-excited length of the fiber is increased, and the optical losses were characterized. Moreover, the η_{SIC} was calculated, obtaining the best values for lumogen red doped fibers. A strong dependence with the dopant concentration was observed, yielding higher η_{SIC} as the concentration increases. The η_{FFSC} was also calculated employing a halogen lamp. The highest values were achieved for the LR03 sample. It was demonstrated that the presence of

a thin cladding is essential in order to minimize the transmission losses, and consequently, to increase the overall efficiency of the device. From these preliminary results, it can be concluded that lumogen red doped fibers with high dopant concentration and thin cladding seem to be good candidates for possible applications in the field of FFSCs.

5.6 Result 2: POFs doped with lumogen dyes as FFSCs

In this section four different POFs doped with perylene and naphtalimide derivatives are studied, focusing on their possible use as FFSCs. The samples were fabricated in the drawing tower of the Applied Photonics Group of Bilbao (APG), with the collaboration of the Spanish National Research Council (CSIC, [166]) for the preform fabrication. The side illumination technique was employed in order to determine some of the optical properties of the fabricated fibers, such as the optical losses, the η_{SIC} and their performance under solar simulator excitation.

5.6.1 Samples

The fibers used in this work were fabricated following a two-step process of preform extrusion and fiber drawing, using PMMA as host material and dyes derivatives from perylene and naphtalimide as active dopants, namely, Lumogen F Violet 570 (LV), Lumogen F Yellow 083 (LY), Lumogen F Orange 240 (LO), and Lumogen F Red 305 (LR). The dyes were obtained from BASF and the concentration employed was 0.003 wt% in all cases. The chemical structure of these dyes is illustrated in Figure 5.16. The preforms were produced by an extru-

sion process, where the doped material (the mixture of PMMA and dye) was fed into the reaction chamber of a homemade extruder. There, it was melted at 165°C and, then, directed to the screw extruder. The material was pushed through a small nozzle, and, finally, the preform was generated with a diameter of 11 mm. The performs were annealed over 14 days in a climate temperature system before drawing them to 1 mm diameter only-core fibers using a POF-drawing-tower at a maximum furnace-temperature of 185°C. The maximum diameter deviation was kept below 7%. A photograph of the four samples is shown in Figure 5.17, and the main characteristics of the fibers are summarized in Table 5.5.

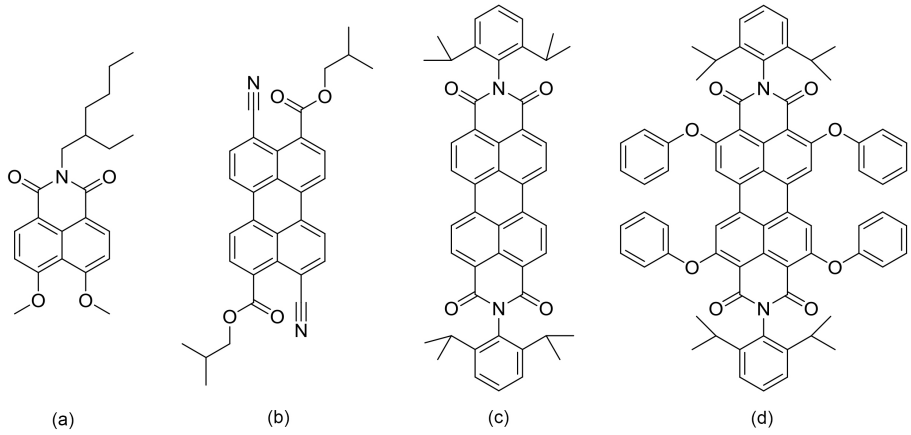

Figure 5.16: Scheme of the chemical structures of (a) Lumogen F Violet 570; (b) Lumogen F Yellow 083; (c) Lumogen F Orange 240; and (d) Lumogen F Red 305.

Figure 5.18 illustrates the absorption and emission curves of the four fibers measured with a CARY spectrometer as seen in Section 4.2. The emission spectra were recorded exciting each of the fibers at their maximum absorption wavelength, except for the LR sample, which was excited at 520 nm due to the wavelength range limitation of the laser source. The main absorption peaks corresponding to the transition from the ground

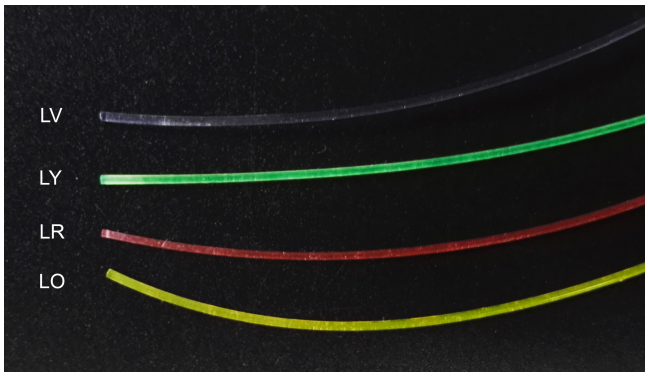

Figure 5.17: Photograph of the 1 mm POFs doped with lumogen violet (LV), yellow (LY), red (LR), and orange (LO).

Table 5.5: Summary of the main characteristics of the fibers doped with lumogen dyes.

Fiber code	**Type**	**Host**	**Dopant**	**Conc. wt%**	**⌀ (mm)**
LV	SI uncladded	PMMA	Lumogen F Violet 570	0.003	1
LY	SI uncladded	PMMA	Lumogen F Yellow 083	0.003	1
LO	SI uncladded	PMMA	Lumogen F Orange 240	0.003	1
LR	SI uncladded	PMMA	Lumogen F Red 305	0.003	1

state S_0 to the first excited singlet state S_1 are located at 392, 472, 524, and 575 nm for LV, LY, LO, and LR respectively, and the emission peaks corresponding to this transition are shown at 423, 515, 571, and 613 nm. The transition from S_0 to the excited singlet state S_2 can also be seen in three of the fibers (LY,LO, and LR) as a weaker absorption band next to the main absorption. Besides, a small band at around 900 nm should be noted, which is due to the infrared absorption of the PMMA matrix. These lumogen-doped fibers present broad absorption bands, what makes a wide wavelength range suitable to be absorbed and converted

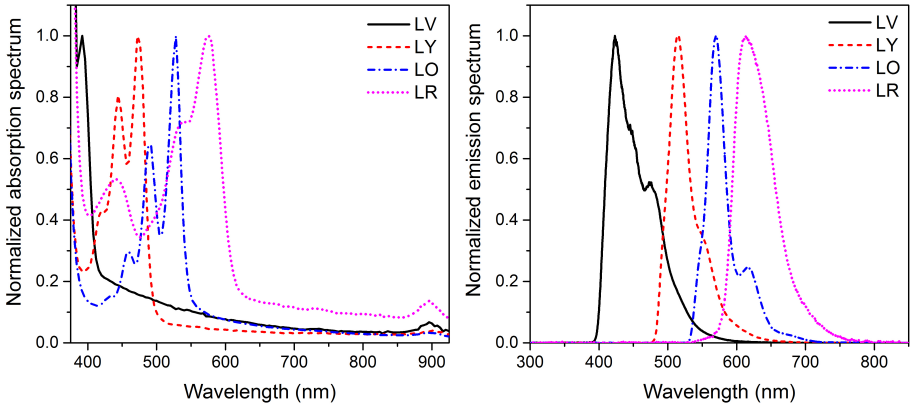

Figure 5.18: Absorption (left) and emission (right) bands of the lumogen doped POFs.

to higher wavelengths. However, their main drawback lies in the overlap between the absorption and emission spectra that, as seen before, causes a red-shift of the emission spectrum and increases the probability of non-radiative emissions.

5.6.2 Optical losses

In this subsection, the effects of varying the propagation length of the fiber z_{ne} are analyzed. The samples were excited with a tunable laser at their maximum absorption wavelengths, except for LR, that was excited at 520 mm.

Figure 5.19 shows the evolution of the output intensity and of the λ_{avg} as a function of z_{ne}. Focusing on the intensity curves, the fiber that undergoes the lowest attenuation appears to be the LR sample, whereas the other three samples show similar transmission losses. This statement will be corroborated later with the calculation of the absorption coefficients. Besides, all samples undergo similar red-shifts on their emission

spectra of around 2.2 nm/cm, which have been calculated by linear fittings to the experimental points.

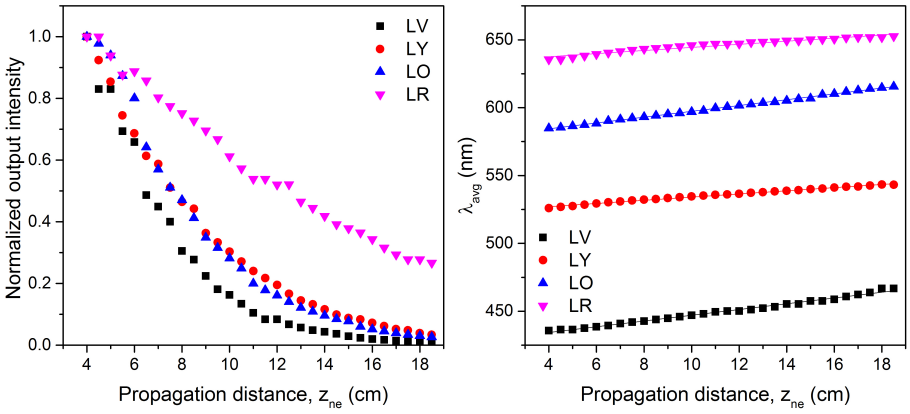

Figure 5.19: Evolution of the output intensity for all emitted wavelengths and of the λ_{avg} as functions of the propagation distance for the four lumogen doped POFs (z_e = 1.2 mm, and a pump irradiance of 52 W/m^2).

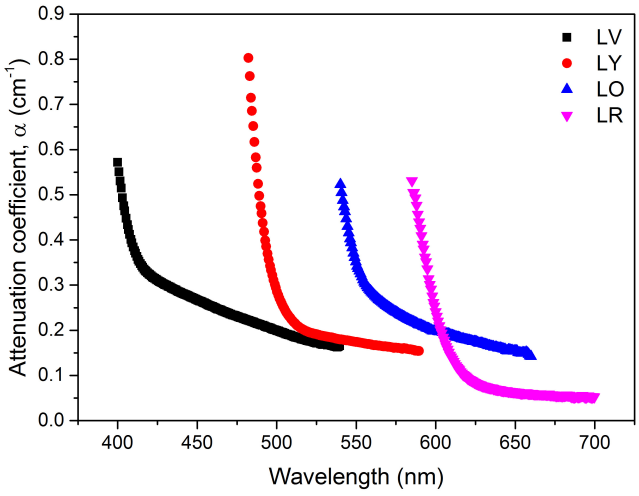

Figure 5.20: Optical attenuation coefficients for the four lumogen doped POFs (z_e = 1.2 mm, and a pump irradiance of 52 W/m^2). The relative error of the obtained coefficients is $\sim 5\%$.

The optical loss coefficients have been calculated as seen in Section 4.2. The attenuation curves obtained are shown in Figure 5.20. As expected, LV, LY, and LO samples undergo similar attenuation values of around 0.15 cm^{-1} in the flat region where the dopant absorption should be negligible. These values appear to be slightly higher than those documented for dye-doped fibers (see Figure 4.19). However, the attenuation measured for the LR doped fiber, with a value of around 0.05 cm^{-1}, is in good agreement with the previously reported numbers for lumogen red doped POFs. In applications where the output power represents a critical factor, such as FFSCs, one of the main goals of the fabrication process would be to reduce the transmission losses as much as possible, by controlling the fabrication parameters from the preform fabrication to the last step of fiber drawing, and by controlling the optimum dopant concentration to avoid saturation and extra reabsorption effects.

5.6.3 Side illumination coupling efficiency

As shown in Section 5.5.3, for applications such as FFSC, the amount of light that the fiber absorbs sideways is an important feature to be quantified. This time, instead of exciting the fibers at ther maximum absoprtion, they were transversally pumped employing a broadband light source with an excitation length of 1 mm. The η_{SIC} values were calculated as shown in equation (5.1) but for the whole excitation spectrum.

Figure 5.21 shows the power absorbed by each fiber as a function of the pump power. As can be seen, the absorbed power increases linearly with the pump power for all fibers, leading to η_{SIC} values of 48%, 54%, 52%, and 48% for LV, LY, LO, and LR respectively with a relative error less than $\sim$ 3%. This means that around 50% of the light coming sideways is absorbed by the fibers. However, as seen in Section 5.2.3 there

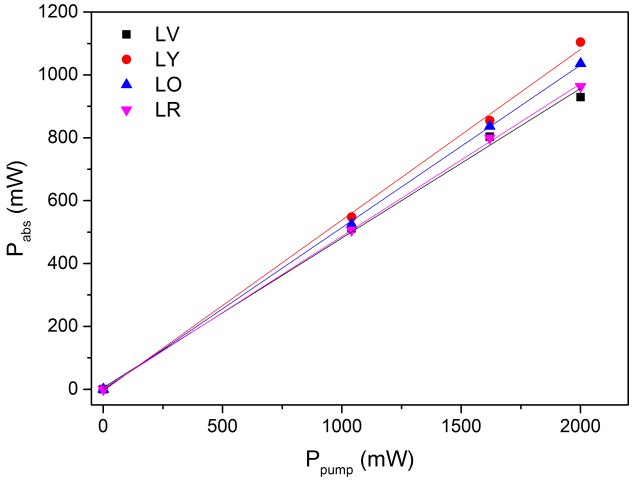

Figure 5.21: Power absorbed sideways by the lumogen doped POFs as a function of the pump power for η_{SIC} calculation. The fibers were pumped with a tunable laser at wavelengths around their absorption peaks. The solid lines represent linear fittings, and the relative errors of the experimental data to these fittings are less than 3%.

are multiple loss mechanism inside the fibers, and not all the absorbed light will reach the fiber end.

5.6.4 Analysis under solar simulator

In this last section, the power-saturation fiber length, the photostability, and the η_{FFSC} were analyzed under halogen lamp excitation ($I = 0.38$ kW/m^2).

To calculate the maximum active length of each sample, an analysis of the evolution of the output power as a function of the illuminated fiber length z_e was conducted. In order to achieve this, the excited fiber length was increased step by step, maintaining a $z_{ne} = 3.3$ cm constant. The results obtained are shown in Figure 5.22. As can be observed, for short illuminated lengths, the output power increases quite rapidly,

but afterwards, it tends to saturate to a maximum output power value. As seen in Section 3.4.1, this evolution is described by equation (3.10). However, as a broadband excitation and detection is used, the equation can be rewritten as:

$$P(z_e) = \frac{C}{\alpha^*}(1 - \exp(-z_e\alpha^*)) \tag{5.3}$$

where, α^* represents an average loss coefficient corresponding to all emission wavelengths. From the fittings of equation (5.3) to the experimental data, the values of α^* were determined. Besides, the fiber length at which the output power curve saturates, L_{sat}, was also determined as the fiber length at which the variation of the output power is less than 0.5%.

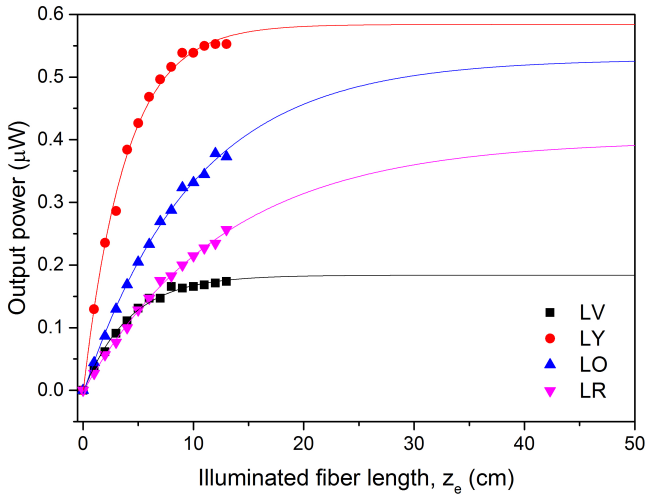

Figure 5.22: Evolution of the output power as a function of z_e for the lumogen doped POFs under lamp excitation. The solid lines represent the fittings of equation (5.3) to the experimental points.

The values of α^* and the saturation length L_{sat} are gathered in Table 5.6. The longest fiber length before reaching saturation is obtained for the LR sample with a value of around 76 cm. This result could be ex-

pected as it is the sample with the lowest optical losses. Besides it agrees with previous experimental values reported for lumogen red doped fibers with the same diameter [167]. Focusing on the α^* values, it has to be noted that they are approximately the values obtained in Figure 5.20 in the the flat part of the optical loss coefficient curves.

Table 5.6: Average loss coefficients α^* and saturation fiber lengths for the four samples L_{sat}. The relative error in the L_{sat} calculation is around 15%.

Fiber code	α^* **(cm^{-1})**	$\mathbf{L_{sat}}$ **(cm)**
LV	0.24 ± 0.02	20
LY	0.26 ± 0.01	22
LO	0.1 ± 0.01	53
LR	0.07 ± 0.01	76

As a second experiment, the photostability of the fibers was analyzed during a 10 h exposure period. The evolution of the temperature of the fiber surface was also measured as a function of the exposure time by means of a thermocouple. The experimental data are shown in Figure 5.23. As can be seen, the output power of all samples is rather stable along the measurement period, which agrees with previous works that demonstrated that dyes derived from perylene exhibit long-term stability in PMMA hosts [168]. Moreover, taking into account that the temperature of the fiber surface increases during the first few hours of exposure and then stabilizes more than 20 °C above the initial temperature, the results obtained also agree with previously reported thermal analysis on different dyes derived from perylene, where high thermal stability was demonstrated [169, 170]. Although in this study, no dependence of the output power with the increase of the temperature has been observed, longer-term outdoor measurements should be carried out in future works

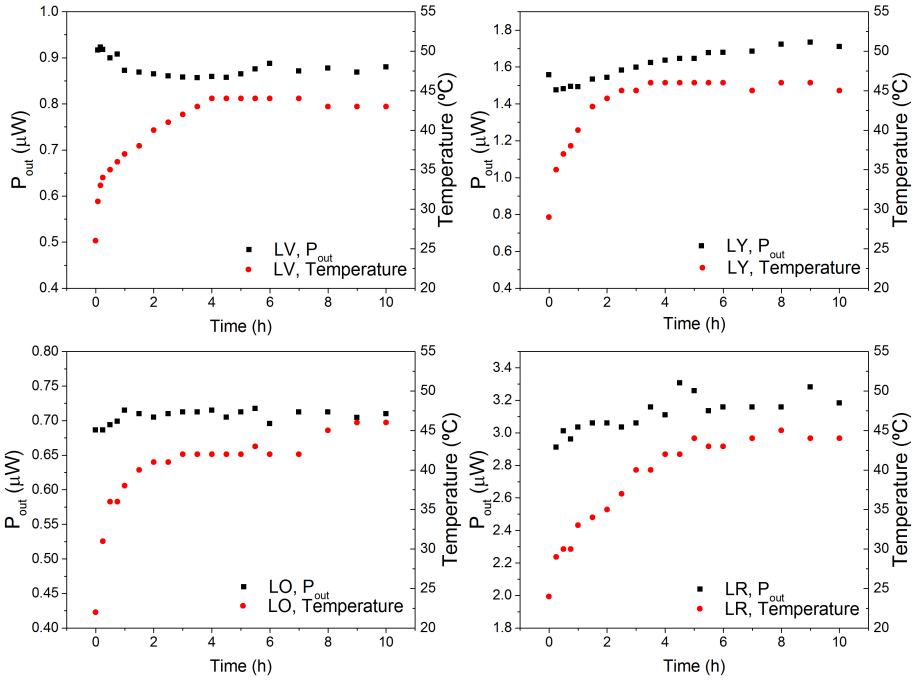

Figure 5.23: Evolution of the output power and the fiber surface temperature along 10 h of lamp exposure ($I = 0,38$ kW/m^2, $z_e = 4.5$ cm).

to determine the fiber useful-lives and the effects of real solar radiation conditions on their stability.

Regarding the η_{FFSC}, the calculated values were around 0.005%, 0.01%, 0.004% and 0.02% for LV, LY, LO and LR respectively obtained for a z_e of 4.5 cm. This values can be considered quite low, though as is the first time our group fabricates and characterizes lumogen-doped POFs, it is believe that these values could easily be improved by employing higher dopant concentrations, and by optimizing the fiber fabrication parameters.

5.6.5 Conclusions

In this work, four different lumogen-doped POFs fabricated by the APG/CSIC collaboration were studied targeting applications in the field of FFSCs. It was seen that all fibers undergo similar red-shifts on their emission spectra when the non-excited length of the fiber is increased, due to reabsorption events. It was also seen that three of the samples show moderate attenuation coefficients in the region where the dopant absorption should be negligible, but for the lumogen red sample, the optical attenuation coefficient values were comparable to those previously reported for lumogen red doped fibers. Besides, it was demonstrated that half of the light that comes sideways is coupled into the fiber, with values of η_{SIC} of around 50% for all the samples. Finally, a study of the power-saturation fiber length and of the photostability was carried out under a solar simulator lamp. Lumogen red sample achieved the longest active length before reaching power saturation, around 76 cm. No variations on the output power were detected after 10 h of continuous light exposure in all fibers, demonstrating the high stability of the dyes. Improvements of the fabrication parameters are the goal for next works.

5.7 Result 3: High performance FFSCs employing double-doped POFs

This work combines the design, fabrication and characterization of novel double-doped POFs for fluorescent fiber solar concentration applications. The proposed sun-light concentration system, combines the benefits of the cylindrical structure of POFs with those of using a hybrid combination of dopants, mixing organic dyes and metal-organic materials. The broad absorption and emission bands of the hybrid dopant

combination permits a broad utilization of the solar spectrum, and the absence of overlap between absorption and emission spectra of metal organic materials contribute to minimize the reabsorption losses. The obtained fibers were characterized under standard AM 1.5G solar simulator excitation. The results obtained may have a strong impact in the field of FFSCs as they offer a promising cost-effective route to green energy production. The entire experimental process was carried out in the facilities of the Applied Organic Materials Group form TUB along a PhD research stay.

5.7.1 Samples and characterization methods

As seen in Section 5.2.4.2, finding all the optimal FFSC properties in a unique luminescent material remains still a challenge. However, it was recently reported that all these ideal characteristics could be found by combining organic and inorganic materials into a hybrid device [131]. For this reason, hybrid combinations of organic-inorganic dopants were chosen for this work, focusing on a broad and efficient utilization of the solar spectrum. After a preliminary study of the absorption, excitation and emission spectra of various dopants in dichloromethane dissolution on a Cary Eclipse G9800A spectrophotometer (Agilent Technologies), five double-doped combinations were selected employing five different dopants (see their chemical structures in Figure 5.24). $Eu(TTFA)_3Phen$ is characterized by its large separation between the absorption and emission bands (around 272 nm), its broad absorption band in the near ultraviolet region, and its narrow emission band at around 615 nm [171]. On the other hand, the selected organic dyes show broad absorption and emission cross sections, long-term stability and high quantum efficiencies in PMMA [172, 168]. These five dopants have good solubility in MMA, which is a determining factor for the correct polymerization pro-

cess. They further survive the rough polymerization conditions with long-term thermal stress at 100°C.

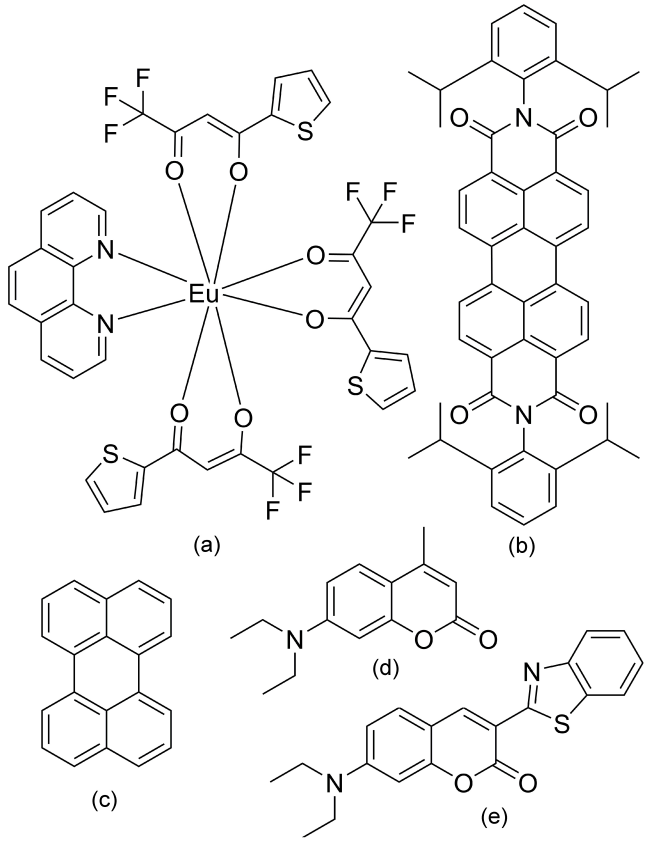

Figure 5.24: Chemical structures of (a) $Eu(TTFA)_3Phen$, (b) Lumogen Orange, (c) Perylene, (d) Coumarin-1, (e) and Coumarin-6.

The selected combinations are the following: $Eu(TTFA)_3Phen$ + Perylene ([Eu/P]); $Eu(TTFA)_3Phen$ + Coumarin-1 ([Eu/C1]); $Eu(TTFA)_3Phen$ + Lumogen Orange ([Eu/L]); $Eu(TTFA)_3Phen$ + Coumrin-6 ([Eu/C6]); and Coumarin-1 + Coumarin-6 ([C1/C6]) (their combined absorption and emission bands can be consulted in Section 5.7.3). From these five combinations, thirteen fibers were fabricated employing different dopant concentrations. Information about the assigned fiber codes

and the dopants employed is gathered in Table 5.7. This table also shows the values of glass transition temperature (Tg) obtained from the differential scanning calorimeter (DSC) (Mettler Toledo), and the number average molecular weight (Mn) and the polydispersity index (PDI) calculated from the size exclusion chromatography (SEC) (SECurity GPC 1260 Infinity system). This polymer analytic gave control information about the polymerization process and was useful for adjusting the parameters of the fiber drawing tower. Figure 5.25 shows an outdoor photograph of one of the [Eu/L] samples excited by the sunlight.

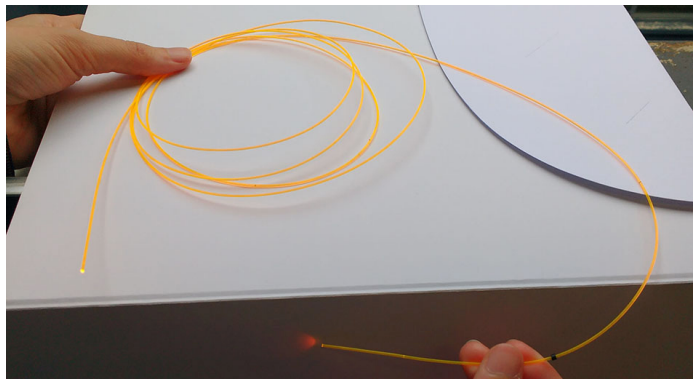

Figure 5.25: Outdoor photograph of the emission of one of the [Eu/L] samples being excited by sunlight.

For characterizing the performance of the fabricated fibers as FFSC, a solar-simulator (Newport Oriel Desktop 91160-1000) was used under the standard 1 Sun AM 1.5G simulated solar radiation [173]. The lamp intensity was calibrated using a reference solar cell. The fibers were placed perpendicularly to the light source at a distance of 24 cm, allowing side excitation at a uniform area of 6 x 6 cm^2. The emission spectra were recorded with a fiber-optic spectrometer (Ocean optics USB2000) with an optical resolution of 1.5 nm of full width at half maximum. The output power at one of the fiber ends was measured employing a silicon

photodetector (Thorlabs S120VC) and a double-channel power meter (Thorlabs PM320E). For the η_{FFSC} measurements and the analysis of the photostability, the excited length of the fiber, z_e, was set to 6 cm. For the study of the performance under simulated weather scenarios, three optical density (OD) filters (1, 0.5 and 0.2) were employed to attenuate the intensity of the solar-simulator, and the z_e was adjusted to 4.5 cm due to the filter characteristics. Two photographs of the experimental set-up are shown in Figure 5.26.

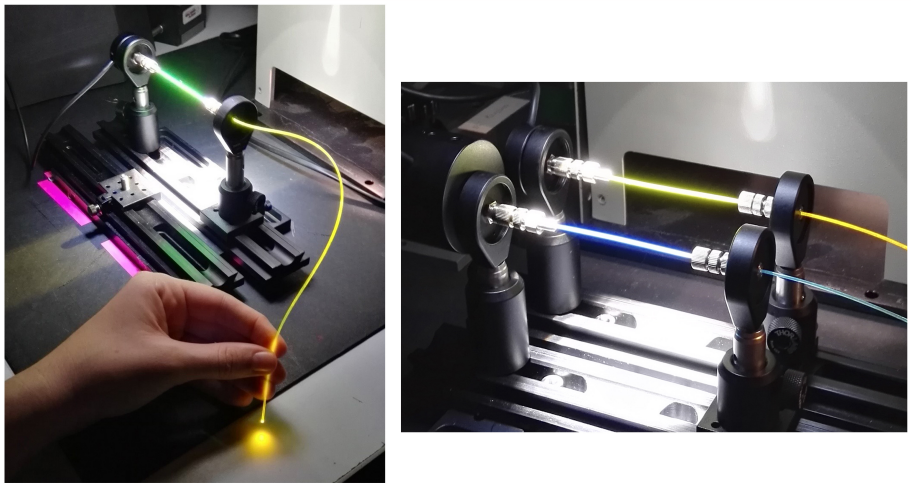

Figure 5.26: Two photographs of some fibers in the set-up under solar simulator excitation.

5.7.2 Fiber fabrication

The fibers were self-fabricated using a double step process of bulk polymerization and fiber drawing. For the preform polymerization, various concentrations of a combination of two different dopants, lauroylperoxide in 0.03 mol% (polymerization initiator), and 1-butyl-mercaptan 0.1 mol% (polymerization inhibitor) were solved in a nitrogen saturated MMA solution at room temperature. The monomer solution was filtered

Table 5.7: Information about the dopants employed in each of the double-doped fibers and the measured values of glass transition temperature (Tg), molecular weight (Mn), and polydispersity index (PDI).

Fiber code	Dopant 1	Dopant 1 conc. (mol%)	Dopant 2	Dopant 2 conc. (mol%)	PDI	Mn (g/mol)	Tg (°C)
F1[Eu/P]$_1$	Eu(TTFA)$_3$Phen	0.001	Perylene	0.002	1.6424	1.2643 E5	120.5
F1[Eu/P]$_2$	Eu(TTFA)$_3$Phen	0.003	Perylene	0.007	1.7007	1.2420 E5	123.6
F2[Eu/C1]$_1$	Eu(TTFA)$_3$Phen	0.001	Coumarin-1	0.0003	1.6452	1.2417 E5	120.9
F2[Eu/C1]$_2$	Eu(TTFA)$_3$Phen	0.003	Coumarin-1	0.0009	1.6945	1.2312 E5	123.7
F3[Eu/L]1	Eu(TTFA)$_3$Phen	0.001	Lumogen Orange	0.001	1.7032	1.2457 E5	121.5
F3[Eu/L]$_2$	Eu(TTFA)$_3$Phen	0.003	Lumogen Orange	0.003	1.7383	1.2315 E5	123.0
F3[Eu/L]$_3$	Eu(TTFA)$_3$Phen	0.005	Lumogen Orange	0.003	1.7046	1.1652 E5	122.5
F4[Eu/C6]$_1$	Eu(TTFA)$_3$Phen	0.001	Coumarin-6	0.003	1.6268	1.2843 E5	123.4
F4[Eu/C6]$_2$	Eu(TTFA)$_3$Phen	0.003	Coumarin-6	0.01	1.68	1.2311 E5	121.8
F4[Eu/C6]$_3$	Eu(TTFA)$_3$Phen	0.005	Coumarin-6	0.005	1.7153	1.1838 E5	119.3
F5[C1/C6]$_1$	Coumarin-1	0.006	Coumarin-6	0.001	1.677	1.2616 E5	122.5
F5[C1/C6]$_2$	Coumarin-1	0.02	Coumarin-6	0.003	1.6860	1.2537 E5	121.3
F5[C1/C6]$_3$	Coumarin-1	0.007	Coumarin-6	0.01	1.6890	1.2046 E5	122.7

into borosilicate tubes with a diameter of 8 mm. These were sealed with silicon plugs and transferred into a programmable heating cabinet. The preforms were heated along five days up to 100°C. This temperature was maintained constant for 1 day before cooling them to 20°C along 24 h. The glasses were carefully removed and the polymer rods were cleaned with isopropanol. Afterwards, they were mounted in the heater unit of a fiber drawing tower, heated to 220°C, and pulled by applying a constant force. For standard SI-POF, a core diameter of 980 μm was targeted, which was monitored and controlled by a laser measuring unit. In a second step, a 20 μm film of PC404F-AP was applied through a nozzle and cured by UV light irradiation to form the cladding. Photographs of some of the double-doped preforms and of two of the fabricated fibers under UV excitation are shown in Figure 5.27.

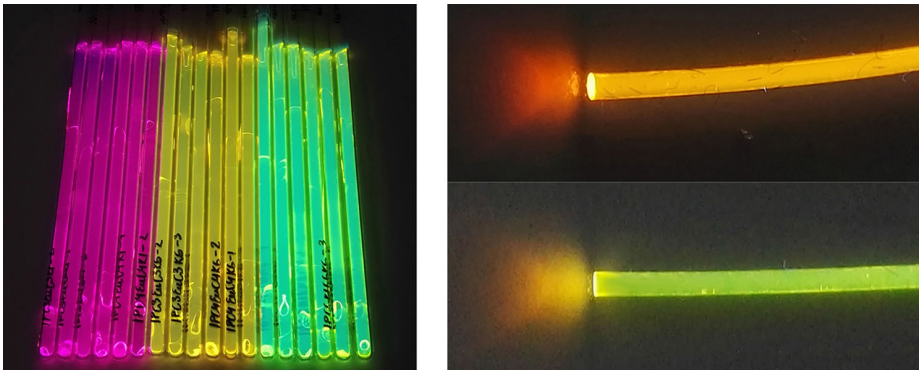

Figure 5.27: Photographs of some of the preforms (left) and two fibers (right) under UV excitation.

5.7.3 Hybrid absorption and emission bands

The standard AM 1.5G radiation spectrum (data source: ASTM G173-03 standard), the measured emission spectrum of the solar-simulator and the absorption and emission bands of the hybrid combinations mea-

sured in dichloromethane dissolution are shown in Figure 5.28. It has to be noted that the spectrum of the solar-simulator was measured employing a fiber-optic spectrometer and a passive PMMA POF as light collector. PMMA starts showing absorption peaks above 700 nm, and thus, the near infrared part of the spectrum could not be detected. The output spectrum data of the solar-simulator can be found in Oriel-Newport products specifications (model 91160).

As can be seen, the absorption spectrum of the $Eu(TTFA)_3Phen$ covers a broad wavelength range of around 130 nm in the near ultraviolet region. Combining the absorption of the Eu(III)-chelate with those of the organic dyes, a remarkable broad absorption band is obtained, with a very small overlap between the absorption and emission spectrum (see graphs (b), (c), (d), and (e)). Also with the combination of two organic dyes (see graph (f)), a considerably broad absorption band is obtained, but with a stronger overlap. However, as we demonstrate in upcoming sections, the fraction of light that could be lost by reabsorption processes corresponds to a very small portion of the total light generated by the double-doped fibers due to their high performance.

5.7.4 Output power and FFSC efficiency

The output power of each of the fibers were measured for an illuminated length of 6 cm and a non-excited length of 3.3 cm up to the detector (SMA connector). The incident power was 60 mW, corresponding to an illuminated area of 6 x 0.1 cm^2 (dimensions of the illuminated fiber piece). The η_{FFSC}, was calculated as seen in equation (5.2). Apart from the output power and η_{FFSC}, an important parameter to determine is the output irradiance, calculated from the output power values and the cross-section area of the fiber (1 mm diameter fibers). This parameter

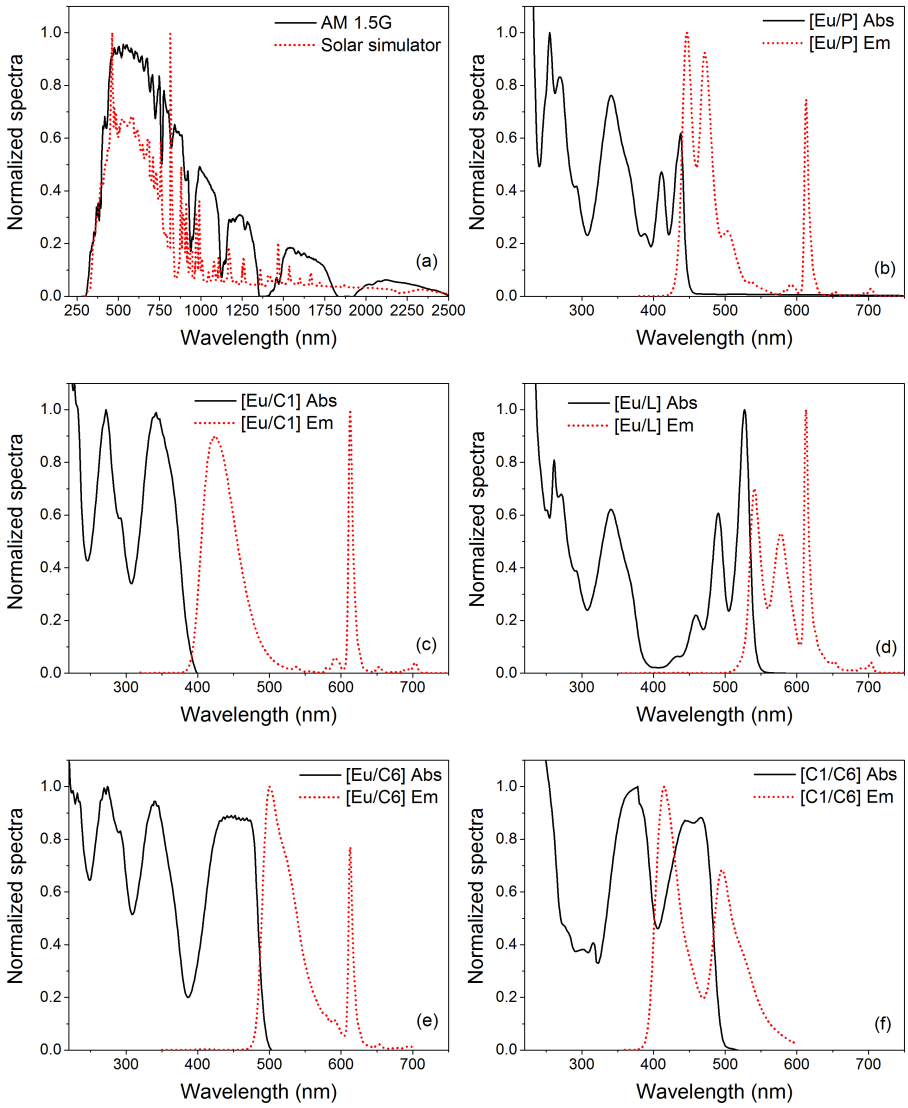

Figure 5.28: Emission of the AM 1.5G radiation and of the solar-simulator (a), and absorption (Abs) and emission (Em) bands of the five double-doped combinations in DCM dissolution: [Eu/P] (b); [Eu/C1] (c); [Eu/L] (d); [Eu/C6](e), and [C1/C6] (f).

represents the light concentration capacity of the fibers.

The output power, output irradiance, and η_{FFSC} values are gathered

in Table 5.8. As can be seen, for all the dopant combinations, there exists a dependence with the dopant concentration, leading to higher power values, and therefore, higher conversion efficiencies and irradiances when greater dopant concentrations are used. From the results obtained, it can be affirmed that it was not reached dopant saturation yet, as the performance improves with an increase in concentration. This tendency is in agreement with a previously reported work that demonstrated that by increasing the Lumogen Red 305 dye concentration, the LSC efficiency also increased [174]. The best performance was obtained for the F3[Eu/L]$_3$, F4[Eu/C6]$_3$, and F5[C1/C6]$_3$ fibers, with power values between 120 and 140 μW, output irradiances of around 0.18 mW/mm^2, and η_{FFSC} of about 0.23%. The combination of [Eu/P] also demonstrates good potential as FFSC with power values of around 50 μW for quite low dopant concentrations, with the possibility of being improved for higher concentrations. We found that the combination of [Eu/C1] is not suitable as FFSC under the solar-simulator illumination conditions. This may be due to fact that [Eu/C1] combination absorbs deep into the near ultraviolet with practically zero absorption in the visible region.

As a second part of the experiment, a mirror like surface was placed bellow the fibers under test at a distance of 4.5 cm, with the purpose of studying the improvements that can be achieved by employing this kind of reflective layers (see Figure 5.29). The results obtained from this analysis are also gathered in Table 5.8. F3[Eu/L]$_3$ and F4[Eu/C6]$_3$ fibers got the highest output power values of around 250 μW for a single piece of fiber of 6 cm in length. This involves a η_{FFSC} of around 0.41% and a concentrated intensity at the fiber end of 0.31 mW/mm^2, which corresponds approximately to one third of the theoretical sun intensity at the earth surface on a fully sunny day. Besides, the relative power improvements as $(P_{+mirror} - P)/P$ were calculated, obtaining results

of more than 63% of improvement for all the samples. The fibers that demonstrated the best performance as FFSC along this first analysis were selected for the upcoming experiments, namely F3[Eu/L]$_2$, F3[Eu/L]$_3$, F4[Eu/C6]$_2$, F4[Eu/C6]$_3$, F5[C1/C6]$_2$, and F5[C1/C6]$_3$.

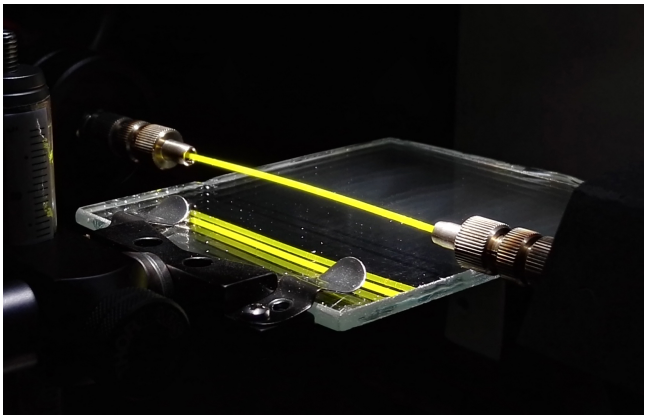

Figure 5.29: Photograph of the reflective layer placed bellow one of the samples under test ([C1/C6]).

5.7.5 Performance under simulated weather scenarios

Going one step further in the characterization of the potential of these fibers, their performance under different excitation intensities was tested. For this purpose, OD filters were employed to attenuate the power of the incident radiation, and to recreate cloudy-day conditions. It is well known that the irradiance that reaches the earth surface is around 1000 W/m^2 in a summer sunny day (clear sky conditions), which corresponds to a power of 45 mW for an excited area of 4.5 x 0.1 cm^2. This irradiance value can decrease to around 300 W/m^2 in a summer fully cloudy day, which implies 3.3 times lower power. This condition can be well recreated by using the OD 0.5 filter, where the pump power is decreased 3.16 times. Furthermore, the irradiance on a fully cloudy

Table 5.8: Output power (P) (with and without mirror), output intensity (I) (with and without mirror), fluorescent fiber solar concentration efficiencies (η_{FFSC}) (with and without mirror), and relative power improvements for 6 cm illuminated fiber length.

Fiber Code	**P (μW) 6 cm**	**I (mW/mm^2) 6 cm**	$\eta_{\mathbf{FFSC}}(\%)$	**P (μW) + mirror**	**I (mW/mm^2) 6 cm + mirror**	$\eta_{\mathbf{FFSC}}(\%)$ **+ mirror**	**Power improvement (%)**
F1[Eu/P]$_1$	46	0.06	0.08	75	0.10	0.12	63
F1[Eu/P]$_2$	52	0.07	0.09	87	0.11	0.14	67
F2[Eu/C1]$_1$	4.8	0.01	0.01	8	0.01	0.013	67
F2[Eu/C1]$_2$	8.7	0.01	0.015	16	0.02	0.26	84
F3[Eu/L]$_1$	85	0.11	0.14	141	0.18	0.24	66
F3[Eu/L]$_2$	125	0.16	0.21	214	0.27	0.36	71
F3[Eu/L]$_3$	140	0.18	0.23	247	0.31	0.41	76
F4[Eu/C6]$_1$	83	0.11	0.14	142	0.18	0.24	72
F4[Eu/C6]$_2$	121	0.15	0.2	208	0.26	0.35	58
F4[Eu/C6]$_3$	136	0.17	0.23	246	0.31	0.41	81
F5[C1/C6]$_3$	69	0.09	0.11	113	0.14	0.19	64
F5[C1/C6]$_2$	95	0.12	0.16	170	0.22	0.28	79
F5[C1/C6]$_3$	120	0.15	0.2	215	0.27	0.36	79

winter day can be in between 6 and 20 times smaller than the one on a clear sky sunny day. This state can be simulated employing the OD 1 filter, lowering 10 times the pump power. Finally, using the OD 0.2 filter, a partially cloudy day (scattered clouds) can be recreated with 1.6 times lower incident power.

Figure 5.30 shows the η_{FFSC} values calculated for three different samples as a function of the incident pump power for a $z_e = 4.5$ cm. As can be seen, the three samples undergo the same evolution pattern, obtaining slightly higher values as the pump power is decreased. This tendency may be explained by two main reasons. On the one hand, the photodegradation of the fibers depends on the excitation intensity. Greater excitation intensities cause an increase in the photodegradation of the samples. On the other hand, possible non-radiative energy transfers between the two involved dopants may also increase with the excitation intensity, leading to a rise in the fluorescence quenching [142, 175]. These two facts, may lead to a lowering in the power conversion potential of these fibers when higher excitation intensities are used. The relative η_{FFSC} improvements were calculated for each of the three different simulated weather conditions taking as reference the efficiency obtained without any filter. This results are gathered in Table 5.9. As can be seen, F3[Eu/L]$_2$ fiber shows slightly lower improvements in the η_{FFSC} than the other two samples, although it is the fiber with the highest efficiency values in all simulated weather conditions. With this experiment, it was successfully demonstrated that these fibers can be used in any kind of weather scenarios, and what is more, they even show small efficiency improvements for cloudy-day conditions.

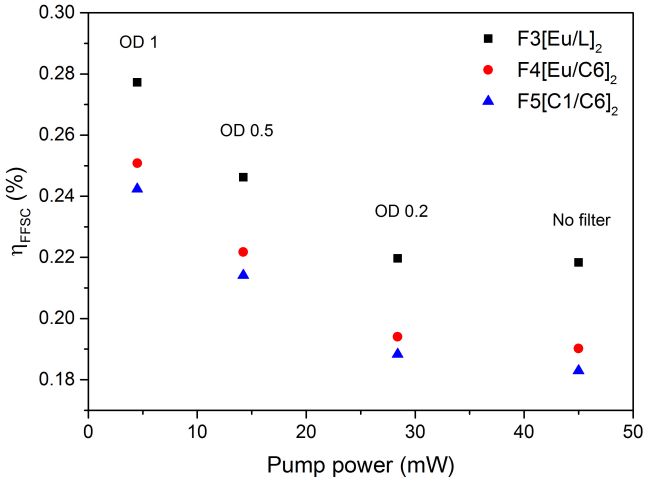

Figure 5.30: Evolution of the η_{FFSC} for three of the samples for an illuminated length of 4.5 cm as a function of the incident pump power.

Table 5.9: Relative η_{FFSC} improvements for each of the simulated weather scenarios.

Fiber code	$\eta_{\mathbf{FFSC}}$ **improvement with OD 0.5** (%) **(cloudy summer day)**	$\eta_{\mathbf{FFSC}}$ **improvement with OD 1** (%) **(cloudy winter day)**	$\eta_{\mathbf{FFSC}}$ **improvement with OD 0.2** (%) **(partially cloudy)**
F3[Eu/L]$_2$	0.13	0.27	0.6
F4[Eu/C6]$_2$	0.17	0.32	2.5
F5[C1/C6]$_2$	0.17	0.32	0.03

5.7.6 Power-saturation fiber length

In this subsection, the evolution of the output power as a function of the illuminated fiber length was studied, for a pump irradiance of 1000 W/m^2. As can be seen in Figure 5.31, the fiber was rolled step by step into loops, increasing the illuminated area, and the output power was measured stepwise at the fiber end closer to the detector.

The curves obtained are shown in Figure 5.32. As can be observed, according to equation (3.10) for short fiber lengths the output power

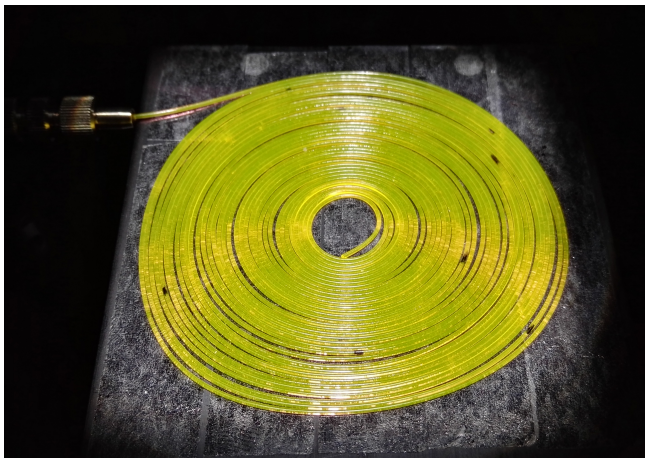

Figure 5.31: Photograph of a [Eu/L] sample rolled into several loops under the solar simulator excitation.

increases quite abruptly for all samples, but afterwards, it tends to saturate. The power-saturation fiber length L_{sat} was calculated from fitting equation (5.2) to the experimental data. It corresponds to the length were the variation of the output power of the fitting curves is less than 0.5%. Taking into account the uncertainty of the detector, the relative error in the calculation of L_{sat} is around 25%. The saturation power value is represented as P_{sat}, and from this, the saturation irradiance is calculated as $I_{sat} = P_{sat}/(\pi r^2)$. The values of P_{sat}, L_{sat}, and I_{sat}, are gathered in Table 5.10.

From this results, it can be seen that F4[Eu/C6]$_3$ and F5[C1/C6]$_3$ fibers obtained the best performance with distance, achieving effective lengths of around 6 m in both cases, and power saturation levels of 1 mW and 890 μW respectively. These results lead to I_{sat} values at the output of a single 1 mm diameter fiber of 1.28 mW/mm^2 and 1.13 mW/mm^2. Taking into account that the intensity of the sun-light is estimated to be around 1 mW/mm^2 at the earth surface, these results are of relevant interest in the field of solar energy harvesting.

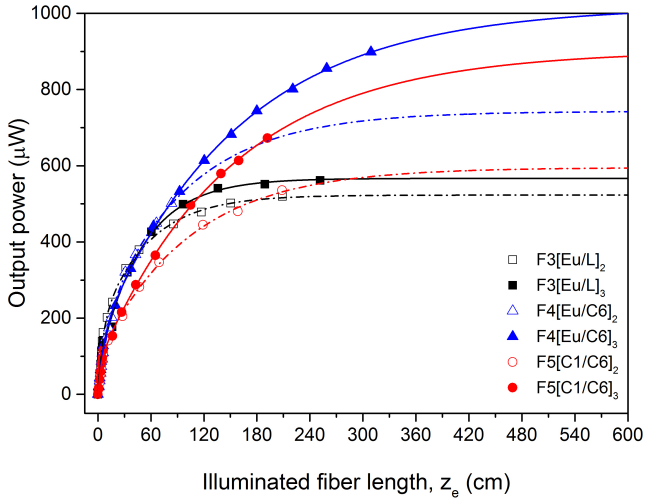

Figure 5.32: Evolution of the output power in one of the fiber ends as a function of the illuminated fiber length. Symbols: experimental points; lines: fitted curves to equation (5.2).

Table 5.10: Saturation fiber length L_{sat}, output saturation power P_{sat} and output saturation irradiance I_{sat} for each sample under test. The relative error in L_{sat} is around 25%.

Fiber code	$\mathbf{L_{sat}}$ **(cm)**	$\mathbf{P_{sat}}$ **(μW)**	$\mathbf{I_{sat}}$ **(mW/mm^2)**
F3[Eu/L]$_2$	243	519	0.66
F3[Eu/L]$_3$	240	563	0.72
F4[Eu/C6]$_2$	428	736	0.94
F4[Eu/C6]$_3$	647	1005	1.28
F5[C1/C6]$_2$	415	586	0.75
F5[C1/C6]$_3$	624	890	1.13

5.7.7 Photostability

Finally, a study of the photodegradation of the double-doped fibers was carried out under constant solar-simulator illumination of 1000 W/m^2 and an excited fiber length of 6 cm. The first experiment addressed a continuous exposure along 160 h, without any recovering slot. The output power was continuously monitored and recorded. The experimental data were well reproduced by a two-phase exponential decay as can be observed in Figure 5.33. The coefficients of determination of these fittings are shown in Table 5.11.

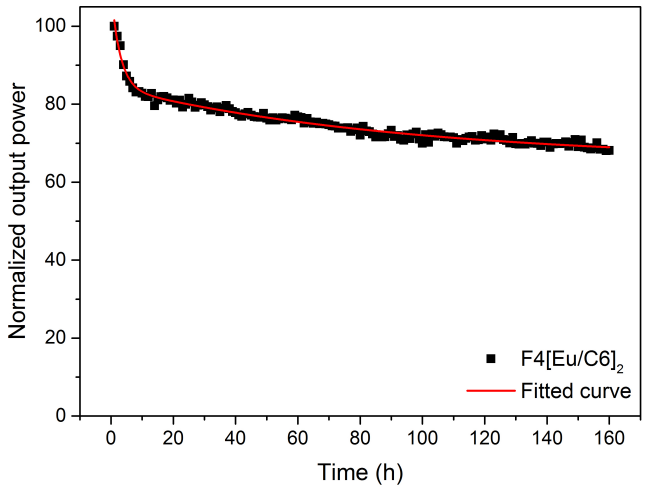

Figure 5.33: Example of the evolution of the normalized output power of F4[Eu/C6]$_2$ sample as a function of the measurement time after 160 h of exposure. Squares: data points; line: fitted curve.

From these fittings, three different parameters have been calculated: The exposure time until reaching 65% of the initial emission (PD65%); the exposure time until reaching 50% of the initial emission (PD50%); and the level at which the degradation tends to saturate (saturation level). The values obtained are summarized in Table 5.11. In this study,

the photodegradation of F1[Eu/P]$_2$ was also analyzed as it is an important feature to determine. As can be seen, the fiber with the best photostability is the F4[Eu/C6]$_2$ sample, with an estimated value of PD65% of around 600 h of continuous illumination, and a saturation level of 64%. F3[Eu/L]$_2$ and F4[Eu/C6]$_3$ samples also demonstrated good performance under continuous illumination, reaching saturation at around 59% and 46% of the initial emission respectively. The fitted curves of F3[Eu/L]$_2$ and F4[Eu/C6]$_2$ tends to saturate before reaching 50% of photodegradation. The samples with the worst performance are those that combine only organic dyes ([C1/C6]) and the combination of [Eu/P]. This latter can be explained from the poor stability of the perylene dye, since it was recently demonstrated that the perylene dye forms stable radicals during the bulk polymerization of the doped PMMA material. Those radicals are trapped in the polymer matrix and might act as photosensitizer resulting in a faster degradation of the dye during the first illumination run [176].

Table 5.11: Exposure time in hours until reaching 65% (PD65%) and 50% (PD50%) of the initial emission, and degradation saturation level. The relative error of the obtained parameters is less than 10% in all cases.

	PD65% (**h**)	**PD50**% (**h**)	**Saturation level** (%)
F1[Eu/P]$_2$	26	63	28
F3[Eu/L]$_2$	180	–	59
F4[Eu/C6]$_2$	600	–	64
F4[Eu/C6]$_3$	114	350	46
F5[C1/C6]$_2$	28	107	30
F5[C1/C6]$_3$	79	181	30

As a second part of the photostability analysis, the partial recovery of the optical properties of the PMMA/double-doped combination was

studied. The experiment was carried out for F4[Eu/C6]$_3$ and F5[C1/C6]$_3$ fibers, along a total period of 508 h, with two recovery slots of 103 h and 73 h. The samples were placed under the solar-simulator without changing their position along the whole experiment, so that the excited area remained invariable. The recovery slots consisted of a period of time under complete darkness, and the recovery percentages were calculated taking as reference the last power value of each of the photodegradation rounds, and the first power value obtained after the rest period. The evolution of the normalized output power is shown in Figure 5.34. During the first excitation round of 160 h the output power of both fibers decreased following a two-exponential decay, as shown in the first part of this section. The samples were then put to rest for 103 h (recovery-1). After this period, the samples underwent a partial recovery of 35% and 42% for F4[Eu/C6]$_3$ and F5[C1/C6]$_3$ respectively. During the second round of radiation exposure of 87 h hours, the output power followed the same photodegradation tendency of a two exponential decay. The fibers were put to rest again for 73 h (recovery-2). After this second recovery period, there was a partial recovery of 17% and 19%. As can be seen, the auto-healing potential of the dopants molecules was diminished in comparison to the first recovery percentages. Finally, a third round of continuous exposure of 78 h was performed where the same decay tendency was observed. The partial recovery percentages are gathered in Table 5.12. It has to be noted that these results may be considerably improved in real sun-light excitation conditions as the light exposure is not continuous (day/night sun cycle) and the probability of self-healing of the dopant molecules increases. This effect was demonstrated in the work of Mansour et al. where they carried out stability and degradation experiments on PMMA/perylene samples under continuous arc lamp irradiation and under sun-light. They reported that the degradation rate due to daylight was less than that due to arc lamp, because the dark pe-

riods at night permitted an incomplete recovery of the optical properties of PMMA/perylene [170].

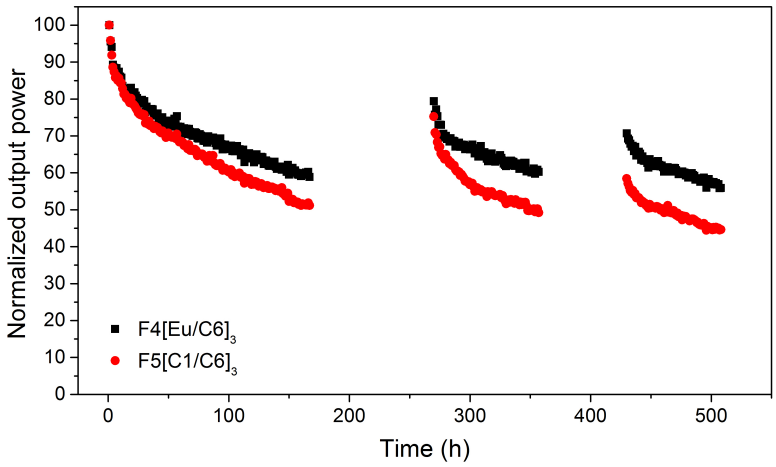

Figure 5.34: Evolution of the normalized output power during the excitation/recovery tests as a function of the measurement time.

Table 5.12: Partial recovery percentages after darkness resting. Recovery-1: 103 h; Recovery-2: 72 h.

Fiber Code	**Recovery-1 (103 h)**	**Recovery-2 (72 h)**
$F4[Eu/C6]_3$	35%	17%
$F5[C1/C6]_3$	42%	19%

As a final analysis of the results obtained from this second part of the experiment, the time that takes to reach 15% of the initial emission in each of the radiation exposures was calculated. The values obtained are given in Table 5.13. From these values it can be deducted that non-degraded dopant molecules reach this 15% decrease in power in a short time, but for the second and third radiation exposure the time needed increases, which in the long run would lead to saturation. This may be caused for two main reasons. On the one hand, as photodegradation

occurred before, less dopant molecules are available, and therefore, the probability of destroying them by chance decreases. On the other hand, the photodegradation in the fiber may also occur due to thermal degradation. The presence of less dopant molecules would lead to less absorption events in the fiber, and hence, less energy would be dissipated as thermal radiation. For this reason, the temperature in the fiber would decrease and the losses related to thermal degradation would also be lower.

Table 5.13: Time in hours (h) until reaching 15% of the initial emission for each of the radiation period.

Fiber Code	**1st round 15% (h)**	**2nd round 15% (h)**	**3rd round 15% (h)**
F4[Eu/C6]$_3$	11	18	35
F5[C1/C6]$_3$	9	12	30

5.7.8 Conclusions

In this work, polymer optical fibers doped with a combination of organic dyes and metal-organic materials were fabricated for the first time, employing a bulk polymerization and fiber drawing process to produce high performance FFSCs. The optical properties of these double-doped POFs were reported and analyzed under AM 1.5G solar simulator, and the feasibility of the proposed FFSC system was demonstrated by the promising results obtained. The output power of each of the samples was measured for a short illuminated fiber length of 6 cm obtaining around 250 μW in the best case, which involves a power conversion efficiency of 0.41% and an intensity of 0.31 mW/mm^2. Their performance under different daylight conditions was also studied, demonstrating the applicability of the proposed FFSCs in any kind of weather scenarios, even showing small efficiency improvements for cloudy-day conditions.

Active fiber lengths of more than 6 m were reported for some of the studied samples, with output intensities of around 1.3 mW/mm^2, 1.3 times higher than the intensity that would impinge onto the PV cell with direct sun-light. Finally, a photostability study was presented obtaining a degradation saturation level of 64% for the best sample after more than 600 h of continuous solar simulator exposure, which shows very interesting results for the search of a long-lasting and competent materials for FFSCs. With output intensities comparable to those from the sun, their performance under different weather conditions and the no need of a sun tracking system, the presented FFSC technology appears to be a cost-effective solution to the expensive solar energy production. The findings of this work motivate a follow-up study to further investigate the performance of this FFSC systems.

5.8 Result 4: Diameter dependence on double-doped POFs for FFSCs

This study analyses the diameter dependence of the FFSC performance of three different double-doped POFs. It follows up the previously reported work, where the benefits of using the POF geometry with a hybrid combination of dopants was demonstrated. The aim of this work focused on providing a complete diameter dependence analysis under AM 1.5G radiation, to determine the optimal characteristics of the designed novel FFSC system. The results achieved are of great interest in the search for an optimum cost-effective green energy production device.

5.8.1 Samples and characterization methods

The fibers selected for this work were the three samples that showed the best performance in the previous study, namely F3[Eu/L]$_3$, F4[Eu/C6]$_3$, and F5[C1/C6]$_3$. Information about the dopants employed, their concentration and polymer analysis parameters can be consulted in Table 5.7. For each of the dopant combinations five different fiber diameters were fabricated, which are summarized in Table 5.14. These samples were self-manufactured following the process explained in Section 5.7.2. To obtain fibers with greater diameters, preforms of different sizes were used (7, 10 and 16 mm). Photographs of the preforms before and after polymerization under environmental lighting and UV excitation can be seen in Figure 5.35. The experimental methods employed along the characterization of the samples were the same as those shown in Section 5.7.1. Finally, the absorption and emission bands of the chosen dopant combinations measured in dissolution can be checked in Figure 5.28.

Table 5.14: Summary of the five fiber diameters.

Fiber diameter (μ**m**)	**Core diameter** (μ**m**)	**Cladding thickness** (μ**m**)
600	500	50
750	645	47
1000	980	10
1500	1300	100
2000	1825	87

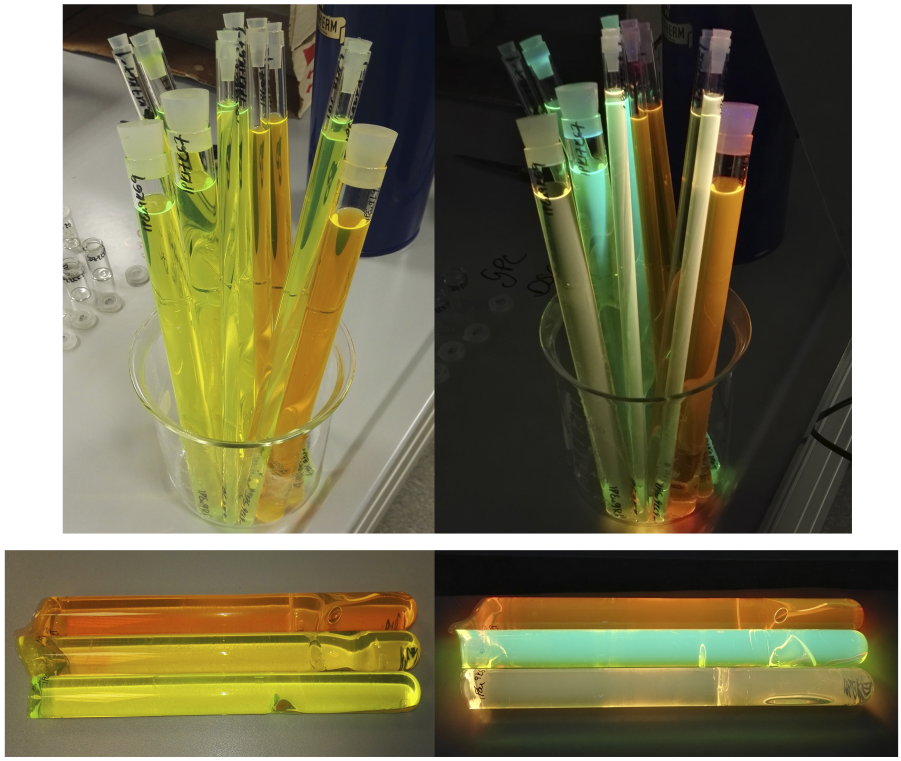

Figure 5.35: Photographs of the preforms before (top) and after (bottom) polymerization under environmental lighting (left) and UV (right) excitation.

5.8.2 Output power and FFSC efficiency

As first experiment, the output power of each of the samples was measured under AM 1.5G excitation (1000 W/m^2) employing an illuminated fiber length of 6 cm and a non-excited length of 3.3 cm. From these power values, two parameters were calculated, the η_{FFSC}, and the output irradiance. The η_{FFSC} was calculated as the ratio between the measured power and the lamp power (see equation (5.2)). It has to be noted that the value of P_{lamp} varies for each of the analyzed fiber di-

ameters since it is calculated taking into account the illuminated fiber surface as $P_{lamp} = I_{lamp} z_e d$ ($I_{lamp} = 1000$ W/m^2, z_e is the illuminated fiber length and d is the fiber diameter).

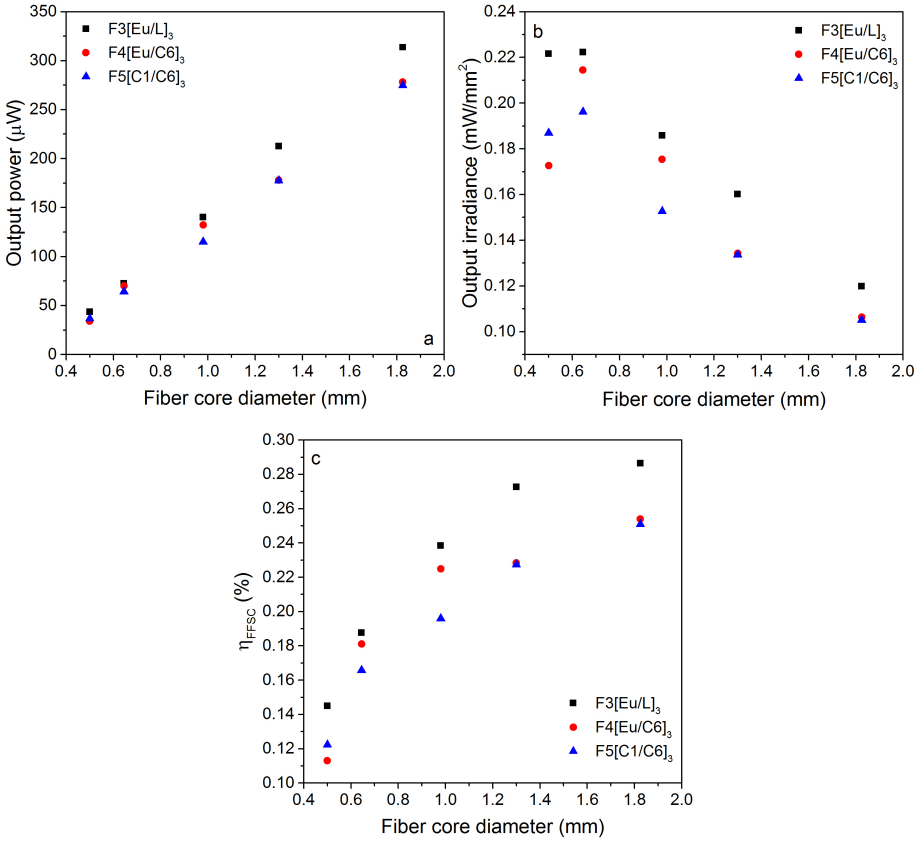

Figure 5.36: Output power (a), output concentrated irradiance (b) and η_{FFSC} (c) for the three double-doped samples as function of the fiber core diameter.

Figure 5.36 illustrates the experimentally measured output power (a), output irradiance (b), and η_{FFSC} (c) for the three double-doped samples. The data were plotted as functions of the fiber core diameters as it corresponds to the active volume of the fibers. Firstly, focusing on graph (a), it can be seen that the output power shows in all cases a linear dependence with the fiber core diameter. Therefore, the greatest

power values are obtained for the the case of the thickest fiber core diameter, namely 314, 278, and 275 μW for F3[Eu/L]$_3$, F3[Eu/C6]$_3$, and F3[C1/C6]$_3$ respectively. Secondly, graph (b) illustrates the irradiance at one of the fiber ends, showing greater concentration irradiances for lower core diameters. Finally, from graph (c) it can be seen that the η_{FFSC} increases with the fiber core diameter but it tends to saturate exponentially. The greatest value is obtained for the thickest sample of F3[Eu/L]$_3$, namely 0.29%.

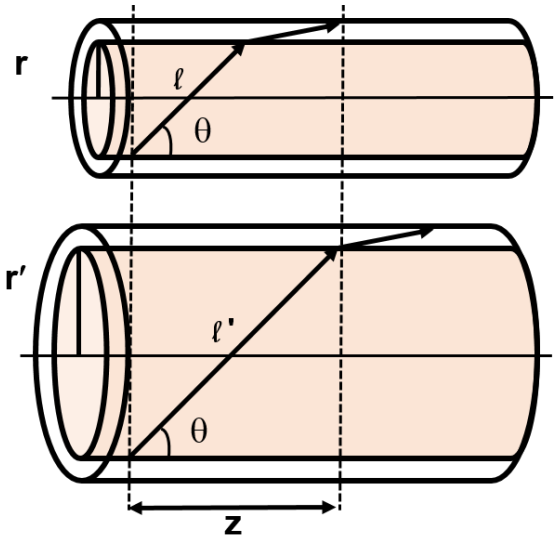

Figure 5.37: Representative model of the distance traveled by light in fibers with different radius ($r < r'$). For the same propagation distance z and for fibers with the same cladding, light travels longer distances ($l < l'$) through the doped core in the fiber with greater radius.

A simple theoretical model was developed capable of describing the behavior of the experimental measurements. Equations (3.6) and (5.3) were used in steady state to obtain an analytic expression for the output power. Working out these equations and for SI POFs ($\gamma = 1$), the

evolution of the power as function of the fiber radius is obtained:

$$P(r) = \left(\frac{C \frac{1}{\sqrt{1+\frac{r^2}{w^2}}} \sigma_{sp} \beta (1 - e^{-\sqrt{1+\frac{r^2}{w^2}} \alpha^* z_e})}{1 - \sigma_{sp} \beta (1 - e^{-\sqrt{1+\frac{r^2}{w^2}} \alpha^* z_e})} \right) I_p \pi r^2 = \kappa(r) I \pi r^2 \quad (5.4)$$

I is the excitation irradiance and r is the fiber core radius. $\kappa(r)$ encompasses the entire first term of equation (5.4), and it represents a factor associated with the propagation losses in the fiber. The dependence with r in this term was included by taking into account that in fibers with the same cladding and for the same propagation distance z, light travels more distance inside the doped core in fibers with larger diameters. A simple representation of this fact can be seen in Figure 5.37. To take this contribution into account, α^* from equation (5.3) was replaced by a radius dependent absorption coefficient: $\alpha(r) = \alpha^*(\sqrt{1 + r^2/w^2})$. C is a dimensionless constant given by the ratio between the excitation and emission absorption coefficients and the ratio between the excitation and emission wavelengths, w represents the half of the propagation distance traveled by light in each reflection, σ_{sp} is the probability of spontaneous emission, and β is the fraction of spontaneous emission contributing to the amplification process along the fiber.

As can be seen, the quadratic dependence of the output power with the fiber radius is compensated by the losses in the material, and therefore, its dependence with the radius is linear. In this way, the radius dependent irradiance and η_{FFSC} are given by the following two equations:

$$I(r) = \frac{P(r)}{\pi r^2} = \kappa(r) I \tag{5.5}$$

$$\eta_{FFSC}(r) = \frac{P(r)}{I z_e 2r} = \kappa(r) \frac{\pi r}{2 z_e} \tag{5.6}$$

From these two equations it can be deducted that the output irradiance decreases with the radius due to propagation losses in the doped core, and η_{FFSC} increases with the core radius, but it is also affected by the contribution of the propagation losses, so it ends up following a tendency to saturation.

To show that the theoretical model agrees with the measurements, Figure 5.38 shows the fittings of the theoretical curves to the experimental points obtained for the F3[Eu/L]$_3$ fiber. The fitting was carried out for $I = 1$ mw/mm^2 and $z_e = 60$ mm, and the resulting parameters are the following: $C = 1.20 \pm 0.02$, $w = 0.48 \pm 0.06$ mm, $\sigma_{sp}\beta = 0.18 \pm 0.01$, and $\alpha^* = 0.11 \pm 0.06$ mm^{-1}. The values of $\sigma_{sp}\beta$ and α^* agree with experimental values employed in similar fibers.

As it is observed, the theoretical model describes well the experimental behavior. The small mismatches between the experimental points and the theoretical curves may be due to other effects that are not taken into account in the simplified model. In such small diameters it could be that the contribution of the losses by reflections is relevant enough to influence in the evolution of the intensity. It could also be due to fabrication defects that worsen in smaller fiber diameters.

The values of the experimental data of Figure 5.36 are gathered in Table 5.15. This table also collects the experimental values obtained when using a reflective layer at a distance from the fiber of 4.5 cm. For this later, a remarkable result is obtained for the F3[Eu/L]$_3$ 2 mm fiber,

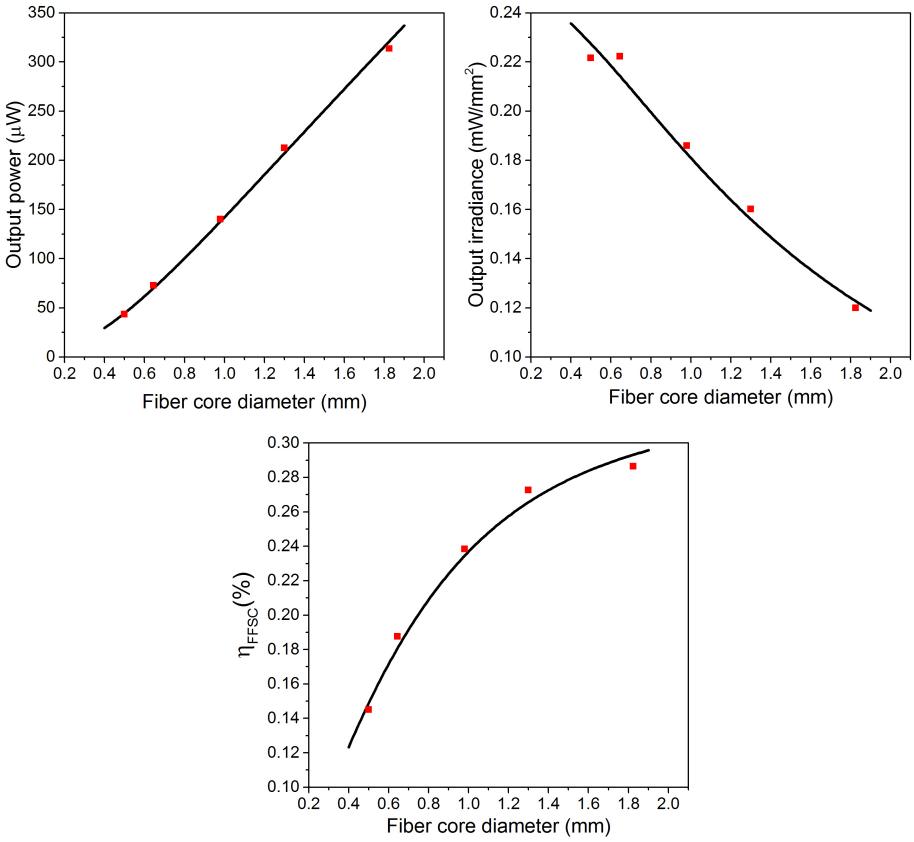

Figure 5.38: Output power, output irradiance and η_{FFSC} of F3[Eu/L]$_3$ fiber as function of the fiber core diameter. Symbols: experimental data; solid lines: fittings.

with an output power value of 540 μW and a conversion efficiency of 0.5% for just one piece of fiber of 6 cm long.

5.8.3 Performance under simulated weather scenarios

The aim of this section was to test the performance of the different diameter fibers under several weather scenarios. To simulate these conditions OD filters were employed to attenuate the power of the incident

Table 5.15: Output power, η_{FFSC} and output irradiance values for the three samples and different fiber diameters without and with a reflective layer at 4.5 cm from the fiber.

	F3[Eu/L]$_3$			**F5[Eu/C6]$_3$**			**F5[C1/C6]$_3$**		
⌀ **(mm)**	**P** (μ**W**)	$\eta_{\mathbf{FFSC}}$ (%)	**I** (**mW/mm^2**)	**P** (μ**W**)	$\eta_{\mathbf{FFSC}}$ (%)	**I** (**mW/mm^2**)	**P** (μ**W**)	$\eta_{\mathbf{FFSC}}$ (%)	**I** (**mW/mm^2**)
0.6	44	0.15	0.22	34	0.11	0.17	37	0.12	0.19
0.75	73	0.19	0.22	70	0.18	0.21	64	0.17	0.20
1	140	0.24	0.19	132	0.22	0.18	115	0.2	0.15
1.5	213	0.27	0.16	178	0.23	0.13	177	0.23	0.13
2	314	0.29	0.12	278	0.25	0.11	275	0.25	0.11
Reflective layer at 4.5 cm:									
0.6	87	0.29	0.44	66	0.22	0.34	72	0.24	0.37
0.75	136	0.35	0.42	133	0.34	0.41	124	0.32	0.38
1	265	0.46	0.36	238	0.40	0.32	217	0.37	0.29
1.5	374	0.48	0.28	320	0.41	0.24	308	0.4	0.24
2	540	0.5	0.21	462	0.42	0.18	465	0.43	0.18

radiation, as explained in Section 5.7.5. All the simulated weather conditions have been tested for five different fiber diameters of each three dopant combinations.

Figure 5.39 shows the calculated η_{FFSC} values as function of the fiber core diameter for the four simulated weather scenarios. From these graphs, it can be seen that the efficiency pattern remains invariable for all simulated weather conditions, i.e., the efficiency increases with the fiber diameter but it tends to saturate exponentially following the same trend for all excitation irradiances. Besides, slightly higher efficiency values are obtained as the pump irradiance is decreased for all the fiber diameters, as photodegradation of the dopant molecules increases with greater pump irradiances. This is the same trend as the one observed for the standard 1 mm fibers tested in Section 5.7.5. It has to be noted that all fiber diameters undergo similar efficiency improvements of around 10%, 7%, and 1% for the cases of cloudy winter day (OD 1), cloudy summer day (OD 0.5), and scattered clouds (OD 0.2) respectively. This values are valid for the three dopant combinations.

Figure 5.40 illustrates the before presented data in a 3D graph, with the aim of giving a gobal point of view of the evolution of the η_{FFSC} with two grades of dependency: excitation irradiance and fiber core diameter. This graph corresponds to the data of sample F4[Eu/C6]$_3$.

As a conclusion of the study presented in this section, it was successfully demonstrated that all the samples presented invariable performance under different weather scenarios, even showing small η_{FFSC} improvements for cloudy-day conditions. This quality reinforces the potential of these samples as FFSC.

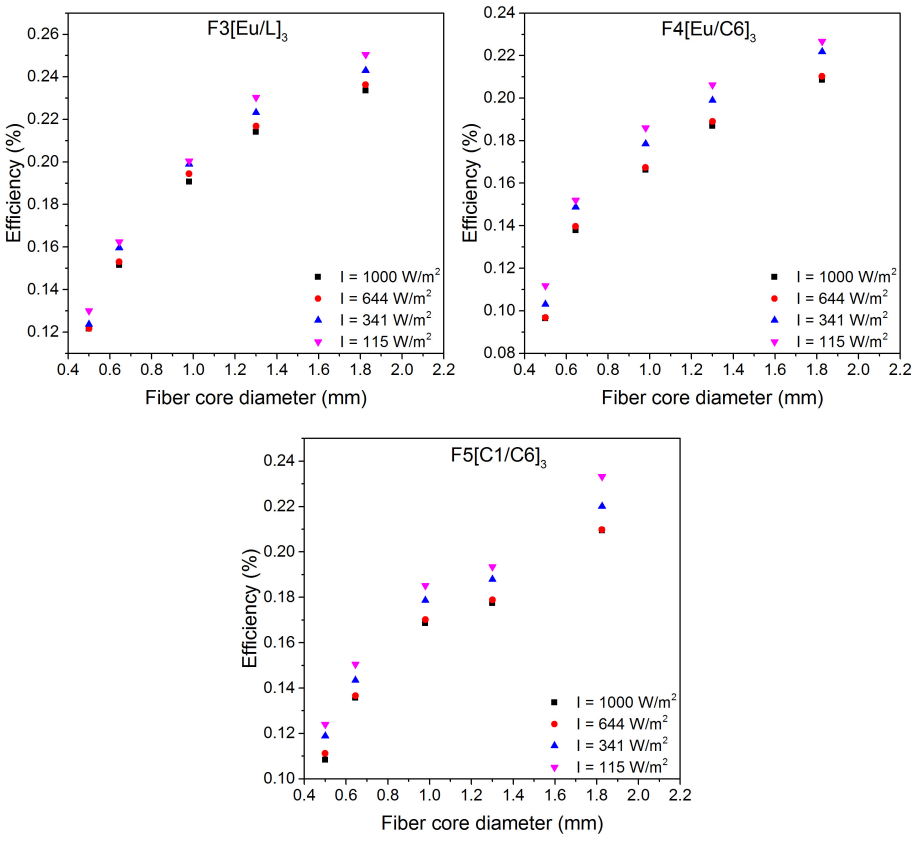

Figure 5.39: Evolution of the η_{FFSC} of the three double-doped combinations for different weather scenarios as function of the fiber core diameter. The illuminated fiber length is 4.5 cm in all cases.

5.8.4 Power-saturation fiber length

In this section, the evolution of the output power as a function of the illuminated fiber length is studied, for a pump irradiance of 1000 W/m^2. As seen in Section 5.7.6, the fiber was rolled step by step into loops and the output power at the fiber end closer to the detector was measured stepwise. The experimental data and the fittings to equation (5.2) are illustrated in Figure 5.41 for three different fiber diameters, 0.6, 0.75 and

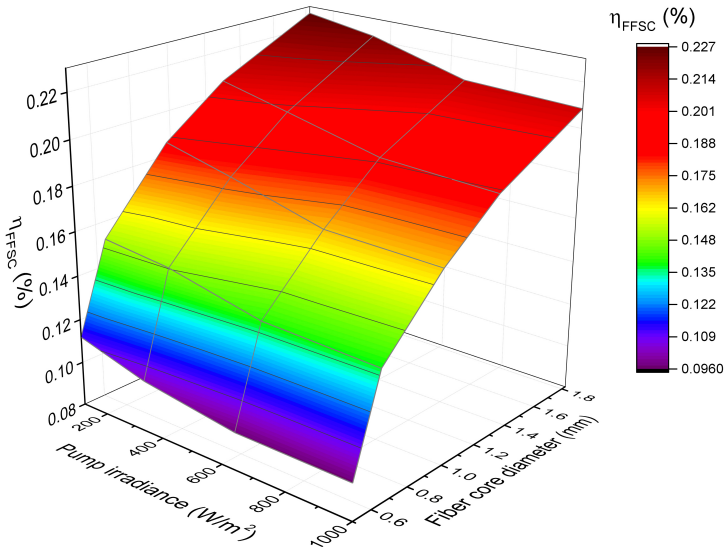

Figure 5.40: 3D plot of the variation of the η_{FFSC} with two variables: excitation irradiance and fiber core diameter for the F4[Eu/C6]$_3$ sample.

1 mm. The saturation fiber length L_{sat} was calculated as done in Section 5.7.6. The values of L_{sat} and P_{sat}, and I_{sat} are gathered in Table 5.16.

Table 5.16: Saturation fiber length L_{sat} (cm), saturation output power P_{sat} (μW), and saturation irradiance (mW/mm^2) for five different fiber diameters. The relative error in L_{sat} is less than 20% in all cases.

	F3[Eu/L]$_3$			**F5[Eu/C6]$_3$**			**F5[C1/C6]$_3$**		
⌀ (mm)	**L$_{sat}$**	**P$_{sat}$**	**I$_{sat}$**	**L$_{sat}$**	**P$_{sat}$**	**I$_{sat}$**	**L$_{sat}$**	**P$_{sat}$**	**I$_{sat}$**
0.6	138	140	0.71	288	158	0.8	235	203	1.04
0.75	203	256	0.78	458	380	1.16	496	430	1.32
1	240	563	0.75	647	1005	1.33	624	890	1.18
1.5	173	615	0.66	308	876	0.66	203	895	0.67
2	301	1041	0.40	280	935	0.36	213	1022	0.39

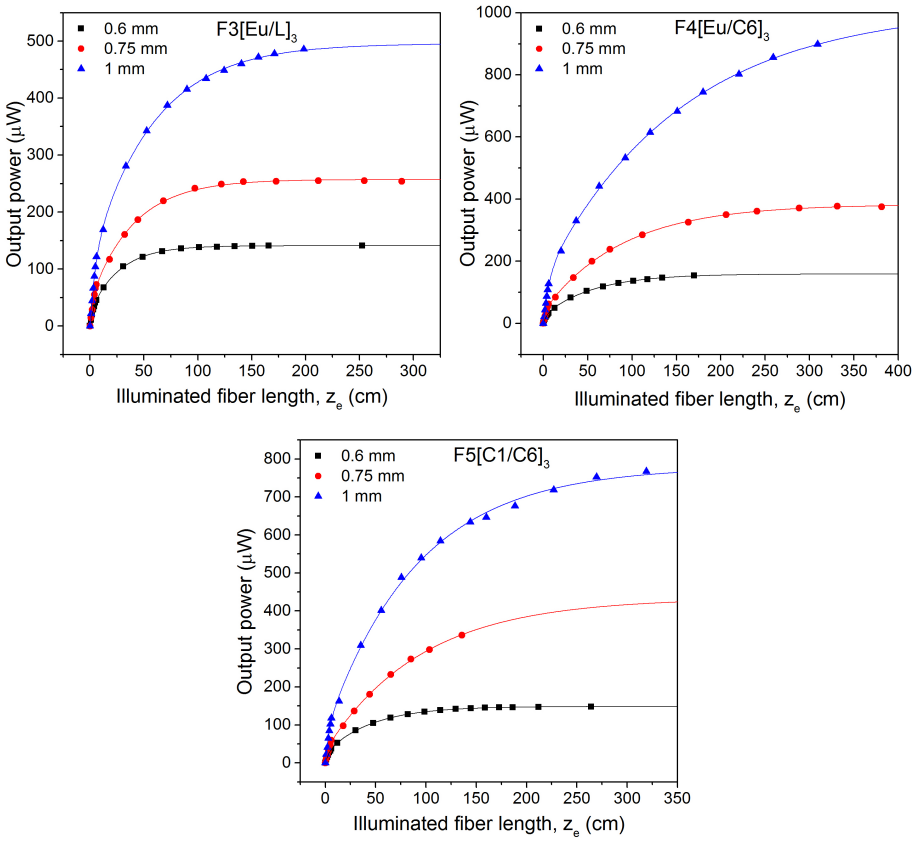

Figure 5.41: Evolution of the output power in one of the fiber ends as a function of the illuminated fiber length for three fiber diameters. Symbols: experimental points; lines: fitted curves to equation (5.2).

On the basis of the assumptions made in Section 5.8.2, fibers with thicker diameters undergo greater absorption in the doped core area, as light travels a larger distance through it than in fibers with smaller diameters (see Figure 5.37). It can be seen that this statement is satisfied for the three thickest fiber diameters (with the only exception of F3[Eu/L]$_3$ 2 mm sample, possibly due to experimental errors). However, the two smallest fiber diameters undergo greater losses. As mentioned before, this may be related to other source of losses that are not taken into account in the simplified model, such as reflection losses or fabrication de-

fects. From the experimental results, it can be seen that that F4[Eu/C6]$_3$ and F5[C1/C6]$_3$ combinations show best performance with distance than F3[Eu/L]$_3$. An interesting result to be noted, is that with the combination of Coumarine-1 and Coumarine-6, the irradiances obtained for the three smallest diameters are greater than the intensity of the sun-light in the earth surface, which is estimated to be around 1 mW/mm^2. These means, that a single 2.35 m length fiber, with a core diameter of 0.5 cm, is able to concentrate a sun-light equivalent irradiance. These results may be of great interest in the design and implementation of FFSCs.

5.8.5 Conclusions

In this work, an analysis of the diameter dependence of the FFSC performance of three different double-doped POFs was presented. The evolution of the output power, of the output irradiance and of the η_{FFSC} with the fiber core diameter were experimentally and theoretically analyzed. It was seen that the output power increases linearly with the fiber core diameter. On the other hand, the output irradiance decreases with the diameter, mainly due to propagation losses in the doped core area. For the same reason, the increase of the η_{FFSC} tends to saturate with the fiber diameter. Moreover, it was demonstrated that all fiber diameters show invariable performance under different lighting conditions, even observing some slight improvements for lower excitation irradinces. These improvements were calculated to be of around 10%, 7%, and 1% for the cases of cloudy winter day, cloudy summer day, and scattered clouds respectively, for all fiber diameters. Finally, the saturation fiber length was studied, yielding highly promising results for FFCS systems. As an example, with F5[C1/C6]$_3$ sample, irradiances comparable to those that would impinge directly from the sun are obtained for the three smallest diameters. As an overall conclusion from this work, when trying to

find the optimum fiber diameter for a specific application, the desired characteristics of the device should be taken into account, and a compromise between the output power and the output irradiance should be taken. For applications were the power represents the key parameter, greater fiber core diameters should be used, whereas if the irradiance is the desired parameter, smaller diameters would be more effective.

Chapter 6

Conclusions and open lines

6.1 Conclusions

Along this thesis work, several studies on the emission properties of numerous doped polymer optical fibers have been reported with the aim of covering two topics in rise in today's society. The whole study was based on the side-illumination technique, where the samples are transversally excited.

To begin, a general overview of POFs is presented in Chapter 2, covering their historical background and basic concepts. This chapter is followed by a description of the fundamental optical processes that occur in dye-doped POFs. The main absorption and emission mechanisms are described by means of a band-like energy level model. Besides, a theoretical model for describing light generation and amplification by the so-called rate equations is presented, and three analytic expressions that will be used all along the results are given. Lastly, a brief description

of the photodegradation phenomenon is presented.

The results of this thesis are divided into two main chapters. Charter 4: Amplified spontaneous emission and gain in dye-doped POFs, and Chapter 5: Solar energy concentration using doped POFs. The main conclusions for each results are presented bellow:

Amplified spontaneous emission and gain in dye-doped POFs:

- By a theoretical study of the local gain it was shown that the gain in a doped POF can be considered rather constant in z_e when large enough excitation lengths are used, as long as the smallest and the largest values of z_e are omitted, which correspond to the transitory growth of the ASE and to the gain saturation region, respectively.

- It was demonstrated that the dopant concentration plays an important role in the ASE and gain performance. By analyzing two R6G doped PMMA GI POFs with different concentrations (12 and 16 ppm) it was seen that the fiber with lower concentration showed a higher ASE threshold, and the pump irradiance had to be much higher for the output spectral width to be similar to the values obtained for the fiber with greater concentration. It was also demonstrated that for an specific excited length, around 20 times less pump irradiance was needed for the higher doping fiber than for lower doping fiber to get the same optical gain of around 13 cm^{-1}.

- It was proven that doped GI fibers are more optimal for amplification, as the interaction between light and dopant is more efficient

than in doped SI ones. In spite of the greater dopant concentration and the higher pump irradiance employed with a SI sample, the optical gains were still slightly higher for a GI sample. The possible influence of the host matrix was not detected in the analyzed properties.

- It was demonstrated that the presence of a cladding is essential to get a more effective ASE performance and greater gains, as it protects the core from external factors such as scratches, fingerprints and environmental conditions that can cause the light to leak out from the fiber. Approximately 30% less energy is needed in the cladded sample for ASE to occur, and greater optical gains were achieved for the cladded fiber under the same measuring conditions.

- It was seen that the ASE properties, such as the threshold-like energy, efficiency and gain, are strongly dependent on the pump polarization. Particularly, for a R6G doped GI POF with an average concentration of 12 ppm, it was demonstrated that the threshold energy is lower (around a half) and that the gain is higher (around 1.23 times) when the pump polarization is perpendicular to the fiber symmetry axis. Therefore, the pump polarization must be carefully controlled in order to optimize the emission performance of dye doped POFs when they are transversely pumped.

- Two-photon fluorescence was measured for two R6G doped thermoset SI POFs. The TPA curves were observed clearly red-shifted by approximately 11 nm from the OPA curves for both samples, although both fibers undergo similar variations of the λ_{avg}. The shifts of the λ_{avg} with the propagation distance could be useful for

the design of displacement sensors based on doped POFs.

In summary, the great potential of the R6G doped POFs as ASE light sources and inline optical amplifiers was demonstrated. It can be concluded that the best scenario for obtaining ASE and gain would be obtained for a GI POF of high dopant concentration (without reaching concentration saturation), with a thin cladding, and a excitation polarization perpendicular to the fiber axis.

Solar energy concentration using doped POFs:

- POFs doped with lumogen red in different concentrations and with conjugated polymers (F8BT F8T2 and PF3T) were analyzed as possible FFSCs. Calculations of the η_{SIC} and the η_{FFSC} were carried out. From the results obtained it was concluded that lumogen red doped fibers with high dopant concentration and thin cladding seem to be good candidates for possible applications in the field of fluorescent solar concentrators, whereas the conjugated polymers studied did not show the best performance for this application.

- Four lumogen (violet, yellow, orange and red) doped POFs were designed and fabricated by a APG/CSIC collaboration. All samples showed good values of η_{SIC}, and no photodegradation of the samples was observed after 10 h of continuous light exposure. Lumogen red sample achieved the longest active length before reaching power saturation. From all the measurements, it can be concluded that lumogen dyes are good candidates for FFSC applications, though improvements of the fabrication parameters must be done to re-

duce transmission losses and improve the overall performance.

- The design, fabrication and characterization under AM 1.5G solar simulator of novel double-doped POFs was carried out. The η_{SIC} and the η_{FFSC} were measured for all fabricated samples, and their applicability in any kind of weather scenarios was demonstrated. Active fiber lengths of around 6 m were reported for some of the studied samples, with output intensities of around 1.3 mW/mm^2, 1.3 times higher than the intensity that would impinge onto the PV cell with direct sun-light. Finally, the photostability measurements showed very interesting results for the search of a long-lasting and competent material for FFSCs. From this study, it was demonstrated that the designed fibers appear to be have great potential as cost-effective solutions to the expensive solar energy production.

- The diameter dependence of the best three double-doped fibers was experimentally and theoretically studied. It was seen that the output power increases linearly with the fiber core diameter, though the output irradiance decreases, mainly due to propagation losses in the doped core area. For the same reason, the increase of the η_{FFSC} tends to saturate with the fiber diameter. It was demonstrated that all fiber diameters show invariable performance under different lighting conditions, and estimations of the power-saturation fiber lengths were carried out, achieving irradiances comparable to those that would impinge directly from the sun for the three smallest diameters of F5[C1/C6]$_3$ sample. From this work, it can be concluded that a compromise must be taken into account between the output power and output intensity when trying to find the optimum fiber diameter for a concrete application. If the output power is the important feature, greater fiber

core diameters should be employed, whereas smaller diameters are preferable if the output intensity is the desired parameter. This results offer a general perceptive to the user to facilitate the optimal design of the FFSC system for a specific target application.

As a global conclusion from all the analysis carried out in Chapter 5, it can be said that there is a promising future regarding doped POFs as solar energy collectors. Mixtures of dopants with high quantum efficiencies and high photostability, that efficiently cover as much as solar spectrum as possible, appears to be a great cost-effective solution to the traditional solar energy harvesting systems.

6.2 Open lines

Although the goal of this thesis has been accomplished by demonstrating the potential of different doped POFs in two fields of full development nowadays, there are many opportunities to expand and strengthen their applications.

Regarding the applicability of doped POFs as light sources and amplifying media, there are several lines of research arising from the multiple new fiber configurations available, such as hollow-core doped POFs, microstructured doped POFs or doped nanofibers [94, 98, 177]. It could also be of great interest to study random lasing in doped POFs by inserting particles with a refractive index other than the host [101]. Besides, the scope of this work could be expanded to the field of sensors. As an example, the variation of the fluorescence spectrum as function of the temperature could be used for sensing temperature in different environ-

ments [177], and its variation as function of the distance traveled by light could serve as displacement sensors. The availability of a fiber drawing tower in the research group, and collaborations with different institutions for the manufacture of the preforms, provides endless possibilities to fabricate different and new fiber structures.

Concerning the field of FFSCs, there are some natural extensions of this work that could contribute with interesting results to those already presented:

- Going beyond the use of a solar simulator, carrying out measurements under real sun excitation conditions would provide information of the performance of the doped POFs in outdoor conditions (changes in environmental factors, variation of the excitation intensity, day/night sun cycle, etc.).
- Fabricating fiber arrays that could cover a bigger area of solar cells is an open line that is already under the first steps of development. Different fiber mounts can be used to help to further increase the performance of the system, such as semicircular rails fabricated in a reflective material (see Figure 6.1). Another possibility to increase the output could be by using both sides of the fiber arrays, or by employing a back-scattering mirror in one of the sides.
- Tests with FFSC arrays attached to silicon solar cells would provide a definite analysis of the performance of the solar energy-to-electricity converter system. This study would offer essential results for the possible implementation and future commercialization of these FFSC devices.

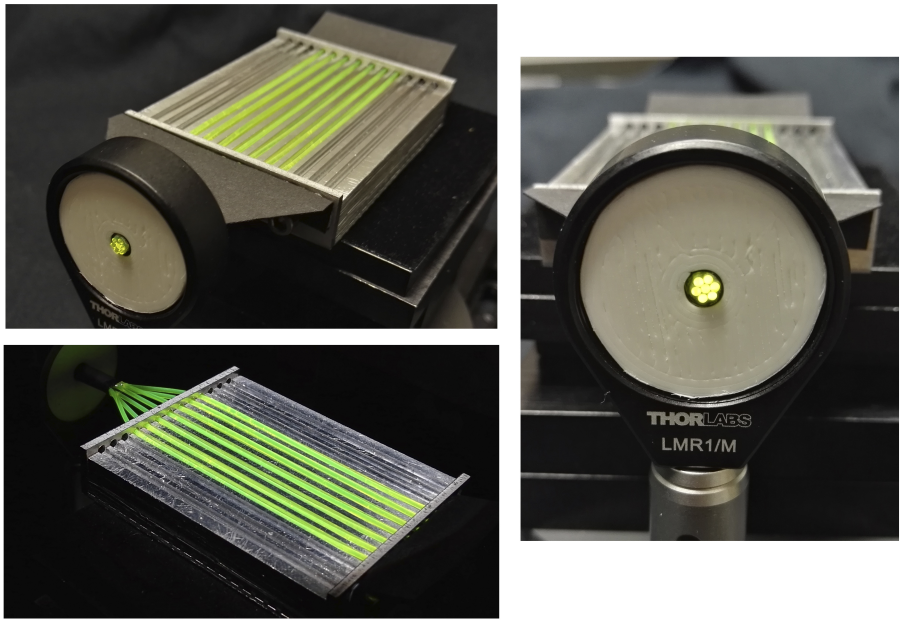

Figure 6.1: Photographs of 7 fiber arrays mounted on semicircular reflective rails.

Bibliography

[1] J. Zubia and J. Arrue. Plastic Optical Fibers: An Introduction to Their Technological Processes and Applications. *Optical Fiber Technology*, 7:101–140, 2001.

[2] T. Kaino, K. Jinguji, and S. Nara. Low loss poly(methylmethacrylate-d8) core optical fibers. *Applied Physics Letters*, 42:567–569, 1983.

[3] Y. Koike. *Fundamentals of Plastic Optical Fibers*. Wiley-VCH Verlag GmbH & Co. KGaA, 2014.

[4] Y. Koike and M. Asai. The future of plastic optical fiber. *NPG Asia Materials*, 1(1):22–28, 2009.

[5] H. Yang, S. C. J. Lee, E. Tangdiongga, C. Okonkwo, H. P. A . van den Boom, F. Breyer, S. Randel, and A. M. J. Koonen. 47.4 Gb/s Transmission Over 100 m Graded-Index Plastic Optical Fiber Based on Rate-Adaptive Discrete Multitone Modulation. *Journal of Lightwave Technology*, 28(4):352–359, 2010.

[6] J. Arrue, M. A. Illarramendi, I. Ayesta, F. Jiménez, J. Zubia, A. Tagaya, and Y. Koike. Laser-Like Performance of Side-Pumped Dye-Doped Polymer Optical Fibers. *IEEE Photonics Journal*, 7(2):1–10, 2015.

[7] L. Jaramillo-Ochoa, R. Narro-García, M. A. Ocampo, and R. Quintero-Torres. High stability of polymer optical fiber with dye doped cladding for illumination systems. *Journal of Luminescence*, 184:205–210, 2017.

[8] R. Narro-García, R. Quintero-Torres, J. L. Domínguez-Juárez, and M. A. Ocampo. Polymer optical fiber with Rhodamine doped cladding for fiber light systems. *Journal of Luminescence*, 169:295–300, 2016.

[9] S. Kamimura and R. Furukawa. Strain sensing based on radiative emission-absorption mechanism using dye-doped polymer optical fiber. *Applied Physics Letters*, 111(063301):1–4, 2017.

[10] C.-F. J. Pun, Z. Liu, M. L. V. Tse, X. Cheng, X. M. Tao, and H. Y. Tam. Side-illumination fluorescence dye-doped-clad PMMA-core polymer optical fiber: Potential intrinsic light source for biosensing. *IEEE Photonics Technology Letters*, 24(11):960–962, 2012.

[11] I. Parola, D. Zaremba, R. Evert, J. Kielhorn, F. Jakobs, M. A. Illarramendi, J. Zubia, W. Kowalsky, and H.-H. Johannes. High performance fluorescent fiber solar concentrators employing doubledoped polymer optical fibers. *Solar Energy Materials and Solar Cells*, 178:20–28, 2018.

[12] J. Zubia, G. Aldabaldetreku, G. Durana, J. Arrue, C. A. Bunge, and H. Poisel. Geometric Optics Analysis of Multi-Step Index Optical Fibers. *Fiber and Integrated Optics*, 23:121–156, 2004.

[13] S. Randel, T. Koonen, J. Lee, F. Breyer, M. Garcia Larrode, A. Ng'oma, G.-J. Rijckenberg, and H. van den Boom. Advanced Modulation Techniques for Polymer Optical Fiber Transmission. In *33rd European Conference and Exhibition on Optical Communication - ECOC 2007*, pages 1–4, 2007.

[14] S. Loquai, R. Kruglov, C. A. Bunge, O. Ziemann, B. Schmauss, and J. Vinogradov. 10.7-Gb/s Discrete Multitone Transmission Over 25-m Bend-Insensitive Multicore Polymer Optical Fiber. *IEEE Photonics Technology Letters*, 22(21):1604–1606, 2010.

[15] A. Berganza, G. Aldabaldetreku, J. Zubia, G. Durana, and J. Arrue. Misalignment losses in step-index multicore plastic optical fibers. *Journal of Lightwave Technology*, 31(13):2177–2183, 2013.

[16] M. van Eijkelenborg, M. Large, A. Argyros, J. Zagari, S. Manos, N. Issa, I. Bassett, S. Fleming, R. McPhedran, C. M. de Sterke, and N. A. Nicorovici. Microstructured polymer optical fibre. *Optics Express*, 9(7):319–327, 2001.

[17] C.-A. Bunge, K. Bremer, B. Lustermann, and G. Woyessa. Special fibres and components. In *Polymer Optical Fibres*, pages 119–151. Elsevier, 2017.

[18] M. C. J. Large, D. Blacket, and C. A. Bunge. Microstructured Polymer Optical Fibers Compared to Conventional POF: Novel Properties and Applications. *IEEE Sensors Journal*, 10(7):1213–1217, 2010.

[19] I.-L. Bundalo, K. Nielsen, C. Markos, and O. Bang. Bragg grating writing in PMMA microstructured polymer optical fibers in less than 7 minutes. *Optics Express*, 22(5):5270–5276, 2014.

[20] A. Stefani, M. Stecher, G. Town, and O. Bang. Direct Writing of Fiber Bragg Grating in Microstructured Polymer Optical Fiber. *IEEE Photonics Technology Letters*, 24(13):1148–1150, 2012.

[21] R. Oliveira, L. Bilro, and R. Nogueira. Bragg gratings in a few mode microstructured polymer optical fiber in less than 30 seconds. *Optics Express*, 23(8):10181–10187, 2015.

[22] A. W. Snyder and J. D. Love. *Optical waveguide theory*. Chapman and Hall, 1983.

[23] M. G. Kuzyk. *Polymer Fiber Optics Materials, Physics, and Applications*. Taylor & Francis Group, 2007.

[24] G. Woyessa, A. Fasano, A. Stefani, C. Markos, K. Nielsen, H. K. Rasmussen, and O. Bang. Single mode step-index polymer optical fiber for humidity insensitive high temperature fiber Bragg grating sensors. *Optics Express*, 24(2):1253–1260, 2016.

[25] O. Abdi, K. Peters, M. Kowalsky, and T. Hassan. Validation of a single-mode polymer optical fiber sensor and interrogator for large strain measurements. *Measurement Science and Technology*, 22(075207):1–10, 2011.

[26] K. Bhowmik, G. D. Peng, E. Ambikairajah, V. Lovric, W. R. Walsh, B. G. Prusty, and G. Rajan. Intrinsic High-Sensitivity Sensors Based on Etched Single-Mode Polymer Optical Fibers. *IEEE Photonics Technology Letters*, 27(6):604–607, 2015.

[27] G. Zhou, C.-F. J. Pun, H.-Y. Tam, A. C. L. Wong, C. Lu, and P. K. A. Wai. Single-Mode Perfluorinated Polymer Optical Fibers Applications. *IEEE Photonics Technology Letters*, 22(2):106–108, 2010.

[28] C. Koeppen, R. F. Shi, W. D. Chen, and A. F. Garito. Properties of plastic optical fibers. *Journal of the Optical Society of America B*, 15(2):727–739, 1998.

[29] G. Rajan, Y. M. Noor, B. Liu, E. Ambikairaja, D. J. Webb, and G. D. Peng. A fast response intrinsic humidity sensor based on an etched singlemode polymer fiber Bragg grating. *Sensors and Actuators A: Physical*, 203:107–111, 2013.

[30] W. Zhang and D. J. Webb. PMMA Based Optical Fiber Bragg Grating for Measuring Moisture in Transformer Oil. *IEEE Photonics Technology Letters*, 28(21):2427–2430, 2016.

[31] W. Yuan, A. Stefani, and O. Bang. Tunable Polymer Fiber Bragg Grating (FBG) Inscription: Fabrication of Dual-FBG Temperature Compensated Polymer Optical Fiber Strain sensors. *IEEE Photonics Technology Letters*, 24(5):401–403, 2012.

[32] S. Teshima, H. Munekuni, and S. Katsuta. Multicore plastic optical fiber for light signal transmission. Patent US08750333, 1998.

[33] S. Piperno, L. Lozzi, R. Rastelli, M. Passacantando, and S. Santucci. PMMA nanofibers production by electrospinning. *Applied Surface Science*, 252:5583–5586, 2006.

[34] Inc. Asahi Jacketed Multi-Core Fiber Cable - Asahi-Kasei offered by Industrial Fiber Optics. http://i-fiberoptics.com/multi-core-fiber-cable.php.

[35] T. Kaino. Preparation of plastic optical fibers for near-IR region transmission. *Journal of Polymer Science Part A: Polymer Chemistry*, 25:37–46, 1987.

[36] A. Kondo, T. Ishigure, and Y. Koike. Fabrication Process and Optical Properties of Perdeuterated Graded-Index Polymer Optical Fiber. *Journal Lightwave Technology*, 23(8):2443–2448, 2005.

[37] Y. Koike and M. Naritomi. Graded-refractive-index optical plastic material of a fluoropolymer containing a material in a concentration gradient therein. Patent US 6,271,312 B1, 2001.

[38] B. S. Rao, J. B. Puschett, and K. Matyjaszewski. Preparation of pH Sensors by Covalent Linkage of Dye Molecules to the Surface of

Polystyrene Optical Fibers. *Journal of Applied Polymer Science*, 43:925–928, 1991.

[39] A. Harlin, M. Mäkinen, and A. Vuorivirta. Development of polymeric optical fibre fabrics as illumination elements and textile displays. *Autex Research Journal*, 3(1):1–8, 2003.

[40] M. A. Van Eijkelenborg, A. Argyros, and S. G. Leon-saval. Polycarbonate hollow-core microstructured optical fiber. *Optics Letters*, 33(21):2446–2448, 2008.

[41] TOPAS Advanced Polymers. https://topas.com/.

[42] ZEONEX - Zeon Specialty Materials Inc. https://www.zeonex.com/.

[43] G. Woyessa, A. Fasano, C. Markos, A. Stefani, H. K. Rasmussen, and O. Bang. Zeonex microstructured polymer optical fiber: fabrication friendly fibers for high temperature and humidity insensitive Bragg grating sensing. *Optical Materials Express*, 7(1):286–295, 2017.

[44] A. Leal-Junior, A. Frizera, M. J. Pontes, A. Fasano, G. Woyessa, O. Bang, and C. A. F. Marques. Dynamic mechanical characterization with respect to temperature, humidity, frequency and strain in mPOFs made of different materials. *Optical Materials Express*, 8(4):804–815, 2018.

[45] I. P. Johnson, W. Yuan, A. Stefani, K. Nielsen, H. K. Rasmussen, L. Khan, D. J. Webb, K. Kalli, and O. Bang. Optical fibre Bragg grating recorded in TOPAS cyclic olefin copolymer. *Electronics Letters*, 47(4):1–2, 2011.

[46] K. Nielsen, H. K. Rasmussen, A. J. Adam, P. C. Planken, O. Bang,

and P. U. Jepsen. Bendable, low-loss Topas fibers for the terahertz frequency range. *Optics Express*, 17(10):8592–8601, 2009.

[47] J. Anthony, R. Leonhardt, A. Argyros, and M. C. J. Large. Characterization of a microstructured Zeonex terahertz fiber. *Journal of the Optical Society of America B*, 28(5):1013–1018, 2011.

[48] J. M. G. Cowie and V. Arrighi. *Polymers: Chemistry and Physics of Modern Materials*. Taylor & Francis Group, 2007.

[49] Thermoplastic vs. Thermoset - Star Thermoplastics ALloys and Rubbers Inc. https://www.starthermoplastics.com/our-chemistry/thermoplastic_vs_thermoset/.

[50] B. Valeur. *Molecular Fluorescence: Principles and Applications*. Wiley-VCH Verlag GmbH, 2001.

[51] W. Denk, J. H. Strickler, and W. W. Webb. Two-Photon Laser Scanning Fluorescence Microscopy. *Science*, 248:73–76, 1990.

[52] J. Liu. Two-photon microscopy in pre-clinical and clinical cancer research. *Frontiers of Optoelectronics*, 8(2):141–151, 2014.

[53] J. Arrue, F. Jiménez, I. Ayesta, M. A. Illarramendi, and J. Zubia. Polymer-Optical-Fiber Lasers and Amplifiers Doped with Organic Dyes. *Polymers*, 3(4):1162–1180, jul 2011.

[54] R. Xia, G. Heliotis, Y. Hou, and D. D. C. Bradley. Fluorene-based conjugated polymer optical gain media. *Organic Electronics*, 4:165–177, 2003.

[55] E. M. Calzado, P. G. Boj, and M. A. Díaz-García. Amplified spontaneous emission properties of semiconducting organic materials. *International Journal of Molecular Sciences*, 11:2546–2565, 2010.

[56] I. Parola, M. A. Illarramendi, J. Arrue, I. Ayesta, F. Jiménez, J. Zubia, A. Tagaya, and Y. Koike. Characterization of the optical gain in doped polymer optical fibres. *Journal of Luminescence*, 177:1–8, 2016.

[57] G. D. Peng, Z. Xiong, and P. L. Chu. Fluorescence Decay and Recovery in Organic Dye-Doped Polymer Optical Fibers. *Journal of Lightwave Technology*, 16(12):2365–2372, 1998.

[58] T. Bernas, M. Zarbski, R. R. Cook, and J. W. Dobrucki. Minimizing photobleaching during confocal microscopy of fluorescent probes bound to chromatin: Role of anoxia and photon flux. *Journal of Microscopy*, 215:281–296, 2004.

[59] A. Diaspro, G. Chirico, C. Usai, P. Ramoino, and J. Dobrucki. Photobleaching. In *Handbook of Biological Confocal Microscopy*, pages 690–702. Springer Science+Business Media, 2006.

[60] I. Ayesta, M. A. Illarramendi, J. Arrue, F. Jiménez, and J. Zubia. Two-Photon-Excited Emission in Polymer Optical Fibers Doped With a Conjugated Polymer. *IEEE Photonics Journal*, 6(4):1–10, 2014.

[61] S. K. Ramini and M. G. Kuzyk. A Self Healing Model Based on Polymer-Mediated Chromophore Correlations. *The Journal of Chemical Physics*, 137(5):1–11, 2012.

[62] B. Anderson, S.-T. Hung, and M. G. Kuzyk. Influence of an electric field on photodegradation and self-healing in disperse orange 11 dye-doped PMMA thin films. *Journal of the Optical Society of America B*, 30(12):3193–3201, 2013.

[63] K. Kuriki, T. Kobayashi, N. Imai, T. Tamura, S. Nishihara, Y. Nishizawa, A. Tagaya, and Y. Koike. High-efficiency organic

dye-doped polymer optical fiber lasers. *Applied Physics Letters*, 77:331–333, 2000.

[64] A. Tagaya, S. Teramoto, E. Nihei, K. Sasaki, and Y. Koike. High-power and high-gain organic dye-doped polymer optical fiber amplifiers: novel techniques for preparation and spectral investigation. *Applied optics*, 36(3):572–578, 1997.

[65] I. Ayesta, M. A. Illarramendi, J. Arrue, F. Jimenez, J. Zubia, I. Bikandi, J. M. Ugartemendia, and J.-R. Sarasua. Luminescence Study of Polymer Optical Fibers Doped With Conjugated Polymers. *Journal of Lightwave Technology*, 30(21):3367–3375, 2012.

[66] M. A. Illarramendi, J. Zubia, L. Bazzana, G. Durana, G. Aldabaldetreku, and J. R. Sarasua. Spectroscopic Characterization of Plastic Optical Fibers Doped with Fluorene Oligomers. *Journal of Lightwave Technology*, 27(15):3220–3226, 2009.

[67] H. Liang, Q. Zhang, Z. Zheng, H. Ming, Z. Li, J. Xu, B. Chen, and H. Zhao. Optical amplification of $Eu(DBM)_3Phen$-doped polymer optical fiber. *Optics Letters*, 29(5):477–479, 2004.

[68] H. Liang, Z. Zheng, Z. Li, J. Xu, B. Chen, H. Zhao, Q. Zhang, and H. Ming. Fabrication and amplified spontaneous emission of $Eu(DBM)_3Phen$ doped step-index polymer optical fiber. *Optical and Quantum Electronics*, 36:1313–1322, 2004.

[69] X. Peng, P. Wu, Y. Han, and G. Hu. Computational analysis of the amplified spontaneous emission in quantum dot doped plastic optical fibers. *Laser Physics*, 24:115104, 2014.

[70] H. C. Y. Yu, A. Argyros, G. Barton, M. A. van Eijkelenborg, C. Barbe, K. Finnie, L. Kong, F. Ladouceur, and S. McNiven. Quantum dot and silica nanoparticle doped polymer optical fibers. *Optics Express*, 15(16):9989–9994, 2007.

[71] Z. Hu, Y. Liang, P. Gao, H. Jiang, J. Chen, S. Jiang, and K. Xie. Random lasing from dye doped polymer optical fiber containing gold nanoparticles. *Journal of Optics*, 17(125403):1–6, 2015.

[72] S. Sebastian, C. L. Linslal, C. P. G. Vallabhan, V. P. N. Nampoori, P. Radhakrishnan, and M. Kailasnath. Random lasing with enhanced photostability of a silver nanoparticle doped polymer optical fiber laser. *Laser Physics Letters*, 11(55108):1–5, 2014.

[73] J. Clark and G. Lanzani. Organic photonics for communications. *Nature Photonics*, 4:438–446, 2010.

[74] A. Tagaya, Y. Koike, E. Nihei, S. Teramoto, K. Fujii, T. Yamamoto, and K. Sasaki. Basic performance of an organic dye-doped polymer optical fiber amplifier. *Applied optics*, 34(6):988–92, 1995.

[75] I. D. W. Samuel and G. A. Turnbull. Organic Semiconductor Lasers. *Chemical Reviews*, 107(4):1272–1295, apr 2007.

[76] P. W. France. *Optical Fibre Lasers and Amplifiers*. Springer Netherlands, 1991.

[77] A. Bjarklev. *Optical Fiber Amplifiers: Design and System Applications*. Artech House, 1993.

[78] K. Kuriki, T. Kobayashi, N. Imai, T. Tamura, Y. Koike, and Y. Okamoto. Organic Dye-doped Polymer Optical Fiber Lasers. *Polymers for advanced technologies*, 11:612–616, 2000.

[79] M. Sheeba, K. J. Thomas, M. Rajesh, V. P. N. Nampoori, C. P. G. Vallabhan, and P. Radhakrishnan. Multimode laser emission from dye doped polymer optical fiber. *Applied optics*, 46(33):8089–8094, 2007.

[80] R. F. Kubin and A. N. Fletcher. Fluorescence quantum yields of some rhodamine dyes. *Journal of Luminescence*, 27:455–462, 1982.

[81] S. Muto, A. Ando, O. Yoda, T. Hanawa, and H. Ito. Tunable Laser Using Sheet of Dye-Doped Plastic Fibers. *Electronics and Communications in Japan*, 71(10):1479–1484, 1988.

[82] Z.-C. Li, H. Liang, Z.-Qi. Zheng, Q.-J. Zhang, and H. Ming. Amplified Spontaneous Emission of Rhodamine B-Doped Step-Index Polymer Optical Fibre. *Chinese Physics Letters*, 22(3):618–620, 2005.

[83] H. Liang, B. Chen, Q. Zhang, Z. Zheng, H. Ming, and F. Guo. Amplified Spontaneous Emission of $Eu(DBM)_3Phen$ Doped Step-Index Polymer Optical Fiber by End-Pumping with a YAG. *Journal of Applied Polymer Science*, 98:912–916, 2005.

[84] G. V. Maier, T. N. Kopylova, V. A. Svetlichnyi, V. M. Podgaetskii, S. M. Dolotov, O. V. Ponomareva, A. E. Monich, and E. A. Monich. Active polymer fibres doped with organic dyes: Generation and amplification of coherent radiation. *Quantum Electronics*, 37(1):53–59, 2007.

[85] M. A. Illarramendi, J. Arrue, I. Ayesta, F. Jiménez, J. Zubia, I. Bikandi, A. Tagaya, and Y. Koike. Amplified spontaneous emission in graded-index polymer optical fibers: theory and experiment. *Optics express*, 21(20):24254–24266, 2013.

[86] J. Bonefacino, X. Cheng, M.-L. V. Tse, and H.-Y. Tam. Recent Progress in Polymer Optical Fiber Light Sources and Fiber Bragg Gratings. *IEEE Journal of Selected Topics in Quantum Electronics*, 23(2):1–11, 2017.

[87] B. Redding, P. Ahmadi, V. Mokan, M. Seifert, M. A. Choma, and H. Cao. Low-spatial-coherence high-radiance broadband fiber source for speckle free imaging. *Optics Letters*, 40(20):4607–4610, 2015.

[88] M. J. F. Digonnet. *Rare-Earth-Doped Fiber Lasers and Amplifiers, 2nd Edition, Revised and Expanded.* Marcel Dekker, Inc, 2001.

[89] M. C. J. Large, L. Poladian, G. W. Barton, and M. A. van Eijkelenborg. *Microstructured Polymer Optical Fibres.* Springer, 2008.

[90] G. Morello, A. Camposeo, M. Moffa, and D. Pisignano. Electrospun Amplified Fiber Optics. *ACS Applied Materials and Interfaces*, 7:5213–5218, 2015.

[91] G. Morello, M. Moffa, S. Girardo, A. Camposeo, and D. Pisignano. Optical Gain in the Near Infrared by Light-Emitting Electrospun Fibers. *Advanced Functional Materials*, 24:5225–5231, 2014.

[92] L. Persano, A. Camposeo, P. Del Carro, V. Fasano, M. Moffa, R. Manco, Stefania D'Agostino, and Dario Pisignano. Distributed Feedback Imprinted Electrospun Fiber Lasers. *Advanced materials*, 26(38):6542–6547, 2014.

[93] J. Peter, C. P. G. Vallabhan, P. Radhakrishnan, V. P. N. Nampoori, and M. Kailasnath. ASE and photostability measurements in dye doped step index, graded index and hollow polymer optical fiber. *Optics and Laser Technology*, 63:34–38, 2014.

[94] J. Peter, R. Saleem, A. Sebastian, P. Radhakkrishnan, V. P. N. Nampoori, C. P. Girijavallabhan, and M. Kailasnath. Pumping scheme dependent multimode laser emission from free-standing cylindrical microcavity. *Optics Communications*, 320:125–128, 2014.

[95] H. Liu, J. B. Edel, L. M. Bellan, and H. G. Craighead. Electrospun Polymer Nanofibers as Subwavelength Optical Waveguides Incorporating Quantum Dots. *Small*, 2(4):495–499, 2006.

[96] X. Sun, B. Li, L. Song, J. Gong, and L. Zhang. Electrospinning preparation and photophysical properties of one-dimensional (1D) composite nanofibers doped with erbium(III) complexes. *Journal of Luminescence*, 130(8):1343–1348, 2010.

[97] V. Fasano, A. Polini, G. Morello, M. Moffa, A. Camposeo, and D. Pisignano. Bright Light Emission and Waveguiding in Conjugated Polymer Nanofibers Electrospun from Organic Salt Added Solutions. *Macromolecules*, 46:5935–5942, 2013.

[98] P. Wang, Y. Wang, and L. Tong. Functionalized polymer nanofibers: a versatile platform for manipulating light at the nanoscale. *Light: Science & Applications*, 2(e102):1–10, 2013.

[99] G. S. He, J. D. Bhawalkar, C. F. Zhao, C. K. Park, and P. N. Prasad. Upconversion dye-doped polymer fiber laser. *Applied Physics Letters*, 68:3549–3551, 1996.

[100] Y. Zhu, J. Zhou, and M. G. Kuzyk. Two-photon fluorescence measurements of reversible photodegradation in a dye-doped polymer. *Optics Letters*, 32(8):958–960, 2007.

[101] Z. Hu, B. Miao, T. Wang, Q. Fu, D. Zhang, H. Ming, and Q. Zhang. Disordered microstructure polymer optical fiber for stabilized coherent random fiber laser. *Optics Letters*, 38(22):4644–4647, 2013.

[102] A. Tagaya, Y. Koike, T. Kinoshita, E. Nihei, T. Yamamoto, and K. Sasaki. Polymer optical fiber amplifier. *Applied Physics Letters*, 63(7):883–884, 1993.

[103] G. D. Peng, P. L. Chu, Z. Xiong, T. W. Whitbread, and R. P. Chaplin. Dye-Doped Step-Index Polymer Optical Fiber for Broadband Optical Amplification. *Journal of Lightwave Technology*, 14(10):2215–2223, 1996.

[104] M. Rajesh, M. Sheeba, K. Geetha, C. P. G. Vallaban, P. Radhakrishnan, and V. P. N. Nampoori. Fabrication and characterization of dye-doped polymer optical fiber as a light amplifier. *Applied optics*, 46(1):106–112, 2007.

[105] J. Clark, L. Bazzana, D. D. C. Bradley, J. Cabanillas-Gonzalez, G. Lanzani, D. G. Lidzey, J. Morgado, A. Nocivelli, W. C. Tsoi, T. Virgili, and R. Xia. Blue polymer optical fiber amplifiers based on conjugated fluorene oligomers. *Journal of Nanophotonics*, 2(023504):1–17, 2008.

[106] K. L. Shaklee and R. F. Leheny. Direct Determination of Optical Gain in Semiconductor Crystals. *Applied Physics Letters*, 18:475–477, 1971.

[107] L. Dal Negro, P. Bettotti, M. Cazzanelli, D. Pacifici, and L. Pavesi. Applicability conditions and experimental analysis of the variable stripe length method for gain measurements. *Optics Communications*, 229:337–348, 2004.

[108] T. Ishigure, E. Nihei, and Y. Koike. Graded-index polymer optical fiber for high-speed data communication. *Applied Optics*, 33(19):4261–4266, 1994.

[109] G. Somasundaram and A. Ramalingam. Gain studies of Rhodamine 6G dye doped polymer laser. *Journal of Photochemistry and Photobiology A: Chemistry*, 125:93–98, 1999.

[110] M. A. Illarramendi, J. Zubia, I. Bikandi, I. Ayesta, I. Parola, I. Aramburu, J. Arrue, and A. Tagaya. Pump-polarization effects in dye-doped polymer optical fibers. *(Manuscript Submitted for Publication)*, 2018.

[111] O. Palchik and V. Palchik. Thermoset and thermoplastic fibers

and preparation thereof by uv curing. Patent WO 2012156896A1, 2014.

[112] O. Palchik, N. Jaber, I. Amram, A. Roitfeld, and L. Vaistikh. UV curing process applied for POFs and their doping using fluorescent materials. In *The 24th Intenational Conference on Plastic Optical Fibers*, pages 26–29, 2015.

[113] I. Bikandi, M. A. Illarramendi, J. Zubia, G. Aldabaldetreku, and L. Bazzana. Effects of cladding on the emission of doped plastic optical fibres. *Physica Status Solidi C*, 8(9):2931–2934, 2011.

[114] I. Ayesta, M. A. Illarramendi, J. Arrue, I. Parola, F. Jiménez, J. Zubia, A. Tagaya, and Y. Koike. Optical Characterization of Doped Thermoplastic and Thermosetting Polymer-Optical-Fibers. *Polymers*, 9(90):1–13, 2017.

[115] E . De la Rosa-cruz, C. W. Dirk, O Rodríguez, and V. M. Castaño. Characterization of Fluorescence Induced by Side Illumination of Rhodamine B Doped Plastic Optical Fibers. *Fiber and Integrated Optics*, 20(5):457–464, 2001.

[116] A. Penzkofer and W. Leupacher. Fluorescence behavior of highly concentrated rhodamine 6G solutions. *Journal of Luminescence*, 37:61–72, 1987.

[117] S. Bloński. Aggregation of rhodamine 6G in porous silica gels. *Chemical Physics Letters*, 184(1-3):229–234, 1991.

[118] Statistical Review of World Energy 2017 - BP. https://www.bp.com/content/dam/bp/en/corporate/pdf/energy-economics/statistical-review-2017/bp-statistical-review-of-world-energy-2017-full-report.pdf.

[119] J. Houghton. Global warming. *Reports on Progress in Physics*, 68:1343–1403, 2005.

[120] M. A. Green. The Path to 25% Silicon Solar Cell Efficiency: History of Silicon Cell Evolution. *Progress in Photovoltaics: Research and Applications*, 17:183–189, 2009.

[121] D. Chemisana. Building integrated concentrating photovoltaics: A review. *Renewable and Sustainable Energy Reviews*, 15:603–611, 2011.

[122] C.-F. Chen, C.-H. Lin, H.-T. Jan, and Y.-L. Yang. Design of a solar concentrator combining paraboloidal and hyperbolic mirrors using ray tracing method. *Optics Communications*, 282:360–366, 2009.

[123] V. C. Coffey. Solar Concentrators: Using Optics to Boost Photovoltaics. *Optics and Photonics News*, 22(1):22–27, 2011.

[124] T. Tao, Z. Hongfei, H. Kaiyan, and A. Mayere. A new trough solar concentrator and its performance analysis. *Solar Energy*, 85:198–207, 2011.

[125] W. H. Weber and J. Lambe. Luminescent greenhouse collector for solar radiation. *Applied Optics*, 15(10):2299–2300, oct 1976.

[126] J. S. Batchelder, A. H. Zewai, and T. Cole. Luminescent solar concentrators 1: Theory of operation and techniques for performance evaluation. *Applied Optics*, 18(18):3090–3110, 1979.

[127] J. S. Batchelder, A. H. Zewail, and T. Cole. Luminescent solar concentrators. 2: Experimental and theoretical analysis of their possible efficiencies. *Applied Optics*, 20(21):3733–3754, 1981.

[128] Lumogen F Colorants and Graphic Systems - BASF. http://www2.basf.us/additives/pdfs/p3201e.pdf.

[129] M. J. Currie, J. K. Mapel, T. D. Heidel, S. Goffri, and M. A. Baldo. High-Efficiency Organic Solar Concentrators for Photovoltaics. *Science*, 321:226–228, 2008.

[130] G. Maggioni, A. Campagnaro, S. Carturan, and A. Quaranta. Dye-doped parylene-based thin film materials: Application to luminescent solar concentrators. *Solar Energy Materials and Solar Cells*, 108:27–37, 2013.

[131] B. C. Rowan, L. R. Wilson, and B. S. Richards. Advanced Material Concepts for Luminescent Solar Concentrators. *IEEE Journal on Selected Topics in Quantum Electronics*, 14(5):1312–1322, 2008.

[132] M. D. R. Kaysir, S. Fleming, R. W. MacQueen, T. W. Schmidt, and A. Argyros. Luminescent solar concentrators utilizing stimulated emission. *Optics Express*, 24(6):A497–A505, 2016.

[133] D. L. Waldron, A. Preske, J. M. Zawodny, T. D. Krauss, and M. C. Gupta. PbSe quantum dot based luminescent solar concentrators. *Nanotechnology*, 28(095205):1–6, 2017.

[134] Michael G. Debije and Paul P. C. Verbunt. Thirty Years of Luminescent Solar Concentrator Research: Solar Energy for the Built Environment. *Advanced Energy Materials*, 2:12–35, 2012.

[135] F. Meinardi, S. Ehrenberg, L. Dhamo, F. Carulli, M. Mauri, F. Bruni, R. Simonutti, U. Kortshagen, and S. Brovelli. Highly efficient luminescent solar concentrators based on earth-Abundant indirect-bandgap silicon quantum dots. *Nature Photonics*, 11:177–185, 2017.

[136] P. P.C. Verbunt and M. G. Debije. Progress in Luminescent Solar Concentrator Research: Solar Energy for the Built Environment. In *World Renewable Energy Congress*, pages 2751–2758, 2011.

[137] Nearly zero-energy buildings - European Commission. https://ec.europa.eu/energy/en/topics/energy-efficiency/buildings/nearly-zero-energy-buildings.

[138] A. A. Earp, G. B. Smith, J. Franklin, and P. Swift. Optimisation of a three-colour luminescent solar concentrator daylighting system. *Solar Energy Materials and Solar Cells*, 84:411–426, 2004.

[139] C. Wang, H. Abdul-Rahman, and S. P. Rao. Daylighting can be fluorescent: Development of a fiber solar concentrator and test for its indoor illumination. *Energy and Buildings*, 42:717–727, 2010.

[140] C. Wang, H. Abdul-Rahman, and S. P. Rao. A new design of luminescent solar concentrator and its trial run. *International journal of energy research*, 34:1372–1385, 2010.

[141] A. Goetzberger. Fluorescent Solar Energy Collectors: Operating Conditions with Diffuse Light. *Applied Physics*, 16:399–404, 1978.

[142] M. Xiao and P. R. Selvin. Quantum Yields of Luminescent Lanthanide Chelates and Far-Red Dyes Measured by Resonance Energy Transfer. *Journal of the American Chemical Society*, 123:7067–7073, 2001.

[143] S. McDowall, T. Butler, E. Bain, K. Scharnhorst, and D. Patrick. Comprehensive analysis of escape-cone losses from luminescent waveguides. *Applied optics*, 52(6):1230–1239, 2013.

[144] S. McDowall, B. L. Johnson, and D. L. Patrick. Simulations of luminescent solar concentrators: Effects of polarization and fluorophore alignment. *Journal of Applied Physics*, 108(053508):1–8, 2010.

[145] C. L. Mulder, P. D. Reusswig, A. P. Beyler, H. Kim, C. Rotschild, and M. A. Baldo. Dye alignment in luminescent solar concen-

trators: II. Horizontal alignment for energy harvesting in linear polarizers. *Optics Express*, 18(S1):A91–A99, 2010.

[146] R. W. MacQueen, Y. Y. Cheng, R. G. C. R. Clady, and T. W. Schmidt. Towards an aligned luminophore solar concentrator. *Optics Express*, 18(S2):A161–A166, 2010.

[147] A. M. Taleb. Self absorption treatment for the luminescent solar concentrators. *Renewable Energy*, 26:137–142, 2002.

[148] T. Wang, B. Yu, B. Chen, Z. Hu, Y. Luo, G. Zou, and Q. Zhang. A theoretical model of a cylindrical luminescent solar concentrator with a dye-doping coating. *Journal of Optics*, 15(055709):1–8, 2013.

[149] M. J. Kastelijn, C. W. M. Bastiaansen, and M. G. Debije. Influence of waveguide material on light emission in luminescent solar concentrators. *Optical Materials*, 31:1720–1722, 2009.

[150] M. Zettl, O. Mayer, E. Klampaftis, and B. S. Richards. Investigation of Host Polymers for Luminescent Solar Concentrators. *Energy Technology*, 5:1037–1044, 2017.

[151] F. V. Tooley. *The Handbook of Glass Manufacture*. Ashlee Publishing Company Inc., 1985.

[152] A. F. Mansour. Optical Efficiency and Optical Properties of Luminescent Solar Concentrators. *Polymer Testing*, 17:333–343, 1998.

[153] L. H. Slooff, N. J. Bakker, P. M. Sommeling, A. Büchtemann, A. Wedel, and W. G. J. H. M. Van Sark. Long-term optical stability of fluorescent solar concentrator plates. *Physica Status Solidi (A) Applications and Materials Science*, 211(5):1150–1154, 2014.

[154] M. G. Debije, P. P. C. Verbunt, B. C. Rowan, B. S. Richards, and T. L. Hoeks. Measured surface loss from luminescent solar concentrator waveguides. *Applied Optics*, 47(36):6763–6768, 2008.

[155] P. D. Swift and G. B. Smith. Color considerations in fluorescent solar concentrator stacks. *Applied Optics*, 42(25):5112–5117, 2003.

[156] S. T. Bailey, G. E. Lokey, M. S. Hanes, J. D.M. Shearer, J. B. McLafferty, G. T. Beaumont, T. T. Baseler, J. M. Layhue, D. R. Broussard, Y.-Z. Zhang, and B. P. Wittmershaus. Optimized excitation energy transfer in a three-dye luminescent solar concentrator. *Solar Energy Materials and Solar Cells*, 91:67–75, 2007.

[157] A. Rosencwaig and E. A. Hildum. Nd^{3+} fluorescence quantum-efficiency measurements with photoacoustics. *Physical Review B*, 23(7):3301–3307, 1981.

[158] K. R. McIntosh, N. Yamada, and B. S. Richards. Theoretical comparison of cylindrical and square-planar luminescent solar concentrators. *Applied Physics B*, 88:285–290, jul 2007.

[159] G. Colantuono, A. Buckley, and R. Erdelyi. Ray-Optics Modelling of Rectangular and Cylindrical 2-Layer Solar Concentrators. *Journal of Lightwave Technology*, 31(7):1033–1044, apr 2013.

[160] J. J. H. Videira, E. Bilotti, and A. J. Chatten. Cylindrical and square fibre luminescent solar concentrators: Experimental and simulation comparisons. In *2014 IEEE 40th Photovoltaic Specialist Conference (PVSC)*, pages 2280–2285. IEEE, jun 2014.

[161] S. F. H. Correia, P. P. Lima, P. S. André, M. R. S. Ferreira, and L. A. D. Carlos. High-efficiency luminescent solar concentrators for flexible waveguiding photovoltaics. *Solar Energy Materials and Solar Cells*, 138:51–57, 2015.

[162] E.-H. Banaei and A. F. Abouraddy. Design of a polymer optical fiber luminescent solar concentrator. *Progress in Photovoltaics: Research and Applications*, 23:403–416, apr 2015.

[163] Technische Universität Braunschweig. www.tu-braunschweig.de.

[164] L. Bazzana, G. Lanzani, R. Xia, J. Morgado, S. S., and G L. D. Plastic optical fibers with embedded organic semiconductors for signal amplification. In *16th International Plastic Optical Fibers Conference*, Torino, 2001.

[165] F. López Arbeloa, P. Ruiz Ojeda, and I. López Arbeloa. The fluorescence quenching mechanisms of Rhodamine 6G in concentrated ethanolic solution. *Journal of Photochemistry and Photobiology, A: Chemistry*, 45:313–323, 1988.

[166] Consejo Superior de Investigaciones Científicas - CSIC. www.csic.es.

[167] J. J. H. Videira, E. Bilotti, and A. J. Chatten. Cylindrical array luminescent solar concentrators: performance boosts by geometric effects. *Optics Express*, 24(14):A1188–A1200, 2016.

[168] L. Cerdán, A. Costela, G. Durán-Sampedro, I. García-Moreno, M. Calle, M. Juan-y Seva, J. de Abajo, and G. A. Turnbull. New perylene-doped polymeric thin films for efficient and long-lasting lasers. *Journal of Materials Chemistry*, 22:8938–8947, 2012.

[169] G. R. J. Müller, C. Meiners, V. Enkelmann, Y. Geerts, and K. Müllen. Liquid crystalline perylene-3,4-dicarboximide derivatives with high thermal and photochemical stability. *Journal of Materials Chemistry*, 8(1):61–64, 1998.

[170] A. F. Mansour, M. G. El-Shaarawy, S. M. El-Bashir, M. K. El-Mansy, and M Hammam. Optical study of perylene dye doped

poly(methyl methacrylate) as fluorescent solar collector. *Polymer International*, 51:393–397, apr 2002.

[171] L. R. Melby, N. J. Rose, E. Abramson, and J. C. Caris. Synthesis and Fluorescence of Some Trivalent Lanthanide Complexes. *Journal of the American Chemical Society*, 86(23):5117–5125, 1964.

[172] W. G. J. H. M. van Sark, K. W. J. Barnham, L. H. Slooff, A. J. Chatten, A. Buechtemann, A. Meyer, S. J. McCormack, R. Koole, D. J. Farrell, R. Bose, E. E. Bende, A. R. Burgers, T. Budel, J. Quilitz, M. Kennedy, T. Meyer, C. De Mello Donega, A. Meijerink, and D. Vanmaekelbergh. Luminescent Solar Concentrators - A review of recent results. *Optics Express*, 16(26):21773–21792, 2008.

[173] STM G173 03(2012) Standard Tables for Reference Solar Spectral Irradiances: Direct Normal ASTM and Hemispherical on 37 Tilted Surface International. https://www.astm.org/Standards/G173.htm.

[174] Z. Krumer, W. G. J. H. M. van Sark, R. E. I. Schropp, and C. de Mello Donegá. Compensation of self-absorption losses in luminescent solar concentrators by increasing luminophore concentration. *Solar Energy Materials and Solar Cells*, 167:133–139, 2017.

[175] J. R. Lakowicz. *Principles of fluorescence spectroscopy*. Springer, 2006.

[176] D. Zaremba, R. Evert, J. Kielhorn, F. Jakobs, R. Caspary, W. Kowalsky, and H.-H. Johannes. Molecular Weight Variations in Perylene-doped PMMA for Luminescent Solar Concentrators (LSCs). *Polymer International*, pages 1–21, 2018.

[177] V. R. Anand, S. Mathew, C. L. Linslal, J. Peter, P. Radhakrishnan, and M. Kailasnath. Tunable amplified spontaneous emission from

dye doped hollow polymer optical fiber. *Journal of Luminescence*, 201:1–4, 2018.

Thesis outreach

Scientific publications

- I. Parola, D. Zaremba, R. Evert, J. Kielhorn, F. Jakobs, M. A. Illarramendi, J. Zubia, W. Kowalsky, and H.-H. Johannes. Diameter dependence on double-doped polymer optical fibers for fluorescent solar concentrators. (*Manuscript in preparation*).

- M. A. Illarramendi, J. Zubia, I. Bikandi, I. Ayesta, I. Parola, I. Aramburu, J. Arrue, and A. Tagaya. Pump-polarization effects in dye-doped polymer optical fibers. (*Manuscript Submitted for Publication at Journal of Lightwave Technology*), 2018.

- I. Parola, D. Zaremba, R. Evert, J. Kielhorn, F. Jakobs, M. A. Illarramendi, J. Zubia, W. Kowalsky, and H.-H. Johannes. High performance fluorescent fiber solar concentrators employing double-doped polymer optical fibers. *Solar Energy Materials and Solar Cells*, 178:20-28, 2018.

- I. Parola , E. Arrospide, F. Recart, M. A. Illarramendi, G. Durana, N. Guarrotxena, O. Garca, and J. Zubia. Fabrication and Characterization of Polymer Optical Fibers Doped

with Perylene Derivatives for Fluorescent Lighting Applications. *Fibers*, 5(28):1-11, 2017.

- I. Ayesta, M. A. Illarramendi, J. Arrue, I. Parola, F. Jimnez, J. Zubia, A. Tagaya, and Y.Koike. Optical Characterization of Doped Thermoplastic and Thermosetting Polymer-Optical-Fibers. *Polymers*, 9(90)1-13, 2017.

- I. Parola, M. A. Illarramendi, J. Zubia, E. Arrospide, G. Durana, N. Guarrotxena, O. Garca, R. Evert, D. Zaremba, H.-H. Johannes, and F. Recart. Polymer optical fibers doped with organic materials as luminescent solar concentrator. *Proceedings of the SPIE–Organic Photonics Materials and Devices XIX*, 10101(10101Z):1-8, 2017.

- I. Parola, M. A. Illarramendi1, I. Ayesta, J. Arrue, F. Jimnez, J. Zubia, S. Diamant, and O. Palchik. Analysis of cladded and uncladded dye-doped step-index polymer optical fibers. *Proceedings of the SPIE–Organic Photonics VII*, 9895(989504):1-10, 2016.

- I. Parola, M. A. Illarramendi, J. Arrue, I. Ayesta, F. Jimnez, J. Zubia, A. Tagaya, and Y. Koike. Characterization of the optical gain in doped polymer optical fibers. *Journal of Luminescence*, 117:1-8, 2016

Conferences

- M. A. Illarramendi, J. Zubia, I. Parola, E. Arrospide, I. Ayesta, J. Arrue, I. Bikandi, N. Guarrotxena, and O. Garca. Progress in Doped Polymer Optical Fibers for Photonic Applications.

Oral talk at *Polymers 2018: Design, Function and Application*, Barcelona, 2018.

- I. Parola, D. Zaremba, R. Evert, J. Kielhorn, F. Jakobs, M. A. Illarramendi, J. Zubia, W. Kowalsky, and H.-H. Johannes. Double-Doped Polymer Optical Fibers for High Performance Fluorescent Fiber Applications. Oral talk at *26th International Conference on Plastic Optical Fibres*, Aveiro, 2017.

- I. Parola, D. Zaremba, R. Evert, M. A. Illarramendi, J. Zubia, W. Kowalsky, and H.-H. Johannes. Double-Doped Polymer Optical Fibers for Fluorescent Fiber Applications. Poster at *The Fiber Society 2017–Spring Conference*, Aachen, 2017.

  ◇ The Fiber Society 2017 Spring Conference Poster Competition Award 3rd place

- I. Parola, M. A. Illarramendi, J. Zubia, E. Arrospide, G. Durana, N. Guarrotxena, O. Garca, R. Evert, D. Zaremba, H.-H. Johannes, and F. Recart. Polymer optical fibers doped with organic materials as luminescent solar concentrator. Oral talk at *SPIE Photonics West 2017*, San Francisco, 2017.

- I. Parola, E. Arrospide, M. A Illarramendi, I. Ayesta J. Zubia, N. Guarrotxena, O. Garca, and C. Vazquez. Fabrication and characterization of a lumogen-orange-doped polymer optical fiber. Invited talk at *The 25th International Conference on Plastic Optical Fibers*, Birmingham, 2016.

- J. Arrue, M. A. Illarramendi, B. Garcia-Ramiro, I. Parola, F. Jimnez, J. Zubia, R. Evert, D. Zaremba, and H.-H. Johannes. Analysis of Light Emission in Polymer Optical Fibers Doped

with Europium Complex. Oral talk at *The 25th International Conference on Plastic Optical Fibers*, Birmingham, 2016.

- I. Parola, M. A. Illarramendi1, I. Ayesta, J. Arrue, F. Jimnez, J. Zubia, S. Diamant, and O. Palchik. Analysis of cladded and uncladded dye-doped step-index polymer optical fibers. Oral talk at *SPIE Photonics Europe 2016*, Brussels, 2016.

- M. A. Illarramendi, J. Zubia, I. Parola, J. Arrue, I. Ayesta, F. Jimnez, A. Tagaya, Y. Koike, S. Diamant, and O. Palchik. Gain phenomena in doped thermoset and thermoplastic polymer optical fibers. Invited talk at *Smart Materials 2016*, Singapore, 2016.

- J. Arrue, I. Parola, I. Ayesta, F. Jimnez, M. A. Illarramendi, J. Zubia, A. Tagaya, and Y. Koike. Theoretical and experimental analysis of polymer optical fibers working as broadband lasers. Oral talk at *The 24th International Conference on Plastic Optical Fibers*, Nuremberg, 2015.

- I. Parola, I. Ayesta, M. A. Illarramendi, and J. Zubia. Amplificación de luz en fibras de plástico dopadas: cálculo de ganancias ópticas. Poster at *IX Reunión Española de Optoelectrónica*, Salamanca, 2015.

Press Release

Press release of the article *High performance fluorescent fiber solar concentrators employing doubledoped polymer optical fibers* (*Solar Energy Materials and Solar Cells*). Sources:

- New high-performance polymer optical fibre designed to obtain solar energy. https://www.ehu.eus/en/-/eguzki-energia-eskuratzeko-errendimendu-handiko-polimerozko-zuntz-optiko-berria
- Nueva fibra óptica de plástico que capta energía solar con alto rendimiento. http://noticiasdelaciencia.com/not/28003/nueva-fibra-optica-de-plastico-que-capta-energia-solar-con-alto-rendimiento/
- New high-performance polymer optical fibre designed to obtain solar energy. https://www.pv-magazine.com/press-releases/new-high-performance-polymer-optical-fibre-designed-to-obtain-solar-energy/
- Captar energía solar con fibras ópticas de plástico. http://www.-spri.eus/es/tecnologia-comunicacion/captar-energia-solar-fibras-opticas-plastico/
- Nueva fibra óptica de plástico que capta energía solar con alto rendimiento. http://www.solarnews.es/2018/04/03/nueva- fibra-optica-de-plastico-que-capta-energia-solar-con-alto-rendimiento/
- Plastic fiber optic could be the new revolution. https://steemit.-com/english/@thegoldman9/plastic-fiber-optic-could-be-the-new-revolution